Karlsruhe Institute of Technology

Measurement of the Spectrum of Charged Hadrons in $\pi^- + C$ Interactions with the NA61 Experiment

Diplomarbeit
von

Martin Ruprecht

An der Fakultät für Physik
Institut für Experimentelle Kernphysik

Erstgutachter:	Prof. Dr. J. Blümer
Zweitgutachter:	Prof. Dr. M. Feindt
Betreuender Mitarbeiter:	Dr. M. Unger

31. Mai 2012

Zusammenfassung

Einleitung

Vor knapp 50 Jahren wurde von John Linsley zum ersten mal kosmische Strahlung mit einer Energie von mehr als 10^{20} eV nachgewiesen [1], die sogenannte ultrahochenergetische kosmischen Strahlung. Als kosmische Strahlung bezeichnet man vollständig ionisierte Atomkerne außerirdischen Ursprungs, die mit hoher kinetischer Energie (wenige GeV bis über 10^{20} eV) auf die Erdatmosphäre treffen. Ultrahochenergetische Primärteilchen erzeugen dabei einen ausgedehnten Luftschauer, dessen Sekundärteilchen sich am Boden über mehrere Kilometer erstrecken können. Viele Fragen bezüglich des Energiespektrums der kosmischen Strahlung, ihrer Massenzusammensetzung und ihres Ursprungs sind immer noch offen und werden von Wissenschaftlern ausgiebig untersucht.

Die Messung von ausgedehnten Luftschauern erfolgt entweder direkt mit in die Atmosphäre gerichteten Floureszenzteleskopen oder indirekt über Bodendetektoren, die über eine große Fläche verteilt sind.

Um von der Beobachtung von Luftschauern auf die Eigenschaften des Primärteilchens rückschließen zu können, ist ein genaues Verständnis der Schauerentwicklung notwendig. Die Teilchenkaskade wird von Teilchen ausgelöst, deren kinetische Energie häufig weit über derjenigen liegt, die von Teilchenbeschleunigern erreicht werden kann. Außerdem handelt es sich dabei vor allem um hadronische Wechselwirkungen mit geringem Impulsübertrag, die nicht mit quantenchromodynamischen Methoden berechnet werden können. Das hat zur Folge, dass die Schauer phänomenologisch modelliert werden müssen. Die Wechselwirkungsmodelle stützen sich dabei, wenn möglich, auf Messungen. Leider ist ein Mangel an Messungen nicht nur im hochenergetischen Bereich vorzufinden, sondern auch im relativ niederenergetischen Bereich anzutreffen, also den letzten Stufen der Kaskade.

Letztere sind besonders für die Zahl der Myonen auf der Erdoberfläche relevant. Diese Myonenzahl ist eine Messgröße von großem Interesse und wirft außerdem mehrere bisher ungelöste Fragen auf. Eine davon ist das Myonendefizit der Wechselwirkungsmodelle beim Pierre Auger-Observatorium. Eine weiter offene Frage betrifft die Massenzusammensetzung der kosmischen Strahlung auf Grundlage der Messdaten von KASCADE. Die Berechnung basiert auf der gemessen Zahl an Myonen und Elektronen am Boden und auf Schauersimulationen. Das Ergebnis dieser Berechnung hängt stark von den eingesetzten Schauermodellen ab und erlaubt derzeit keine eindeutige Aussage über die Massenzusammensetzung im Energiebereich von KASCADE.

Das Ziel dieser Diplomarbeit ist die Messung des differenziellen inklusiven Wirkungsquerschnitts negativ und positiv geladener Hadronen in $\pi^- + \mathrm{C}$ Kollisionen bei einem Strahlimpuls von 158 GeV/c und 350 GeV/c.

Die Wechselwirkung von Pionen mit Kohlenstoff ähnelt der in einem Luftschauer am häufigst vorkommenden Wechselwirkung, $\pi^\pm + \mathrm{Luft}$, da sich die Ordnungszahl von Stickstoff und Sauerstoff nur um eins bzw. zwei von Kohlenstoff unterscheidet. Kohlenstoff wird verwendet da es im Gegensatz zu den genannten Gasen bei Raumtemperatur fest ist und sich leichter handhaben lässt. Darüber hinaus liegen die untersuchten Kollisionen in einem Energiebereich der wichtig für die Zahl der Myonen an der Erdoberfläche ist.

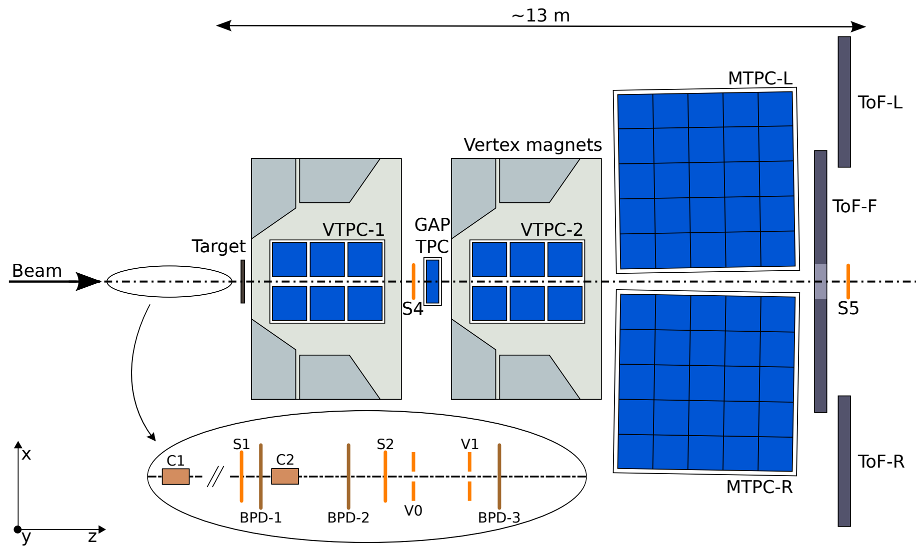

Abbildung 1.: Schematischer Aufbau des NA61-Detektors. Erklärungen zu den einzelnen Bestandteilen befinden sich in Kapitel 2.

Messungen von $\pi^- + \mathrm{C}$ Kollisionen bei einem Strahlimpuls von 158 GeV/c und 350 GeV/c werden dazu beitragen, die Wechselwirkungsmodelle zu verbessern und eventuell einen Beitrag dazu leisten, die oben genannten offenen Fragen zu beantworten.

Das Experiment NA61/SHINE, das sich am Super Proton Synchrotron am CERN befindet, hat neben anderen Messungen die für Luftschauermodelle relevant sind, die Messung von $\pi^- + \mathrm{C}$ Kollisionen bei einem Strahlimpuls von 158 GeV/c und 350 GeV/c durchgeführt. Der NA61-Detektor ist ein Spektrometer für Hadronen die bei Kollisionen mit einem ruhenden Target (englisch für "Ziel") erzeugt werden. Er bestehend aus einer Reihe von Strahldetektoren, Auslösedetekoren, Szintillatoren zur Messung der Flugzeit und vier, teils im Magnetfeld befindlichen Zeitprojektionskammern mit denen die Spuren der Teilchen rekonstruiert werden. In Abbildung 1 ist eine schematische Übersicht der Bestandteile dargestellt.

Analyse

Die Analyse stellt den Hauptteil dieser Arbeit dar. Darin wird beschrieben wie aus den kalibrierten und rekonstruierten Daten des NA61-Detektors die Spektren der geladenen Hadronen gewonnen werden. Der in dieser Arbeit verwendete Analysetyp ist die sogenannte geladene Hadronenanalyse. Dabei werden die positiv und negativ geladenen Hadronen nicht weiter in ihren Teilchentyp (wie Pion oder Kaon) aufgespalten. Leptonen, die auch einen Teil der detektierten Spuren ausmachen, werden jedoch auf der Grundlage von Monte Carlo Simulationen entfernt.

Zunächst werden eine Reihe von Schnitten bezüglich der Ereignisse und Spuren angewandt. Für die Definition der Akzeptanz wird eine geometrische Methode vorgestellt, die jeden Bereich im Phasenraum auf der Grundlage der durch Simulationen erhaltenen Rekonstruktionseffizienz untersucht. Das Resultat ist eine Akzeptanzkarte mit Gebieten mit nahezu 100 prozentiger Akzeptanz und Gebieten ohne Akzeptanz.

Anschließend wird eine Korrektur angewandt, die Spurbeiträge entfernt die nicht vom Kohlenstofftarget stammen. Dazu wurden Ereignisse aufgenommen ohne das Target in der Halterung einzusetzen. Nach Normierung bezüglich der Anzahl der Strahlteilchen kann dieser Beitrag von den Ereignissen mit eingesetztem Target abgezogen werden.

Zwei weitere wichtige Korrekturen in der Analyse sind die Monte Carlo Korrektur und die Korrektur der Verzerrung durch den Wechselwirkungsauslöser. Ersteres enthält folgende Beiträge:

- Akzeptanzkorrektur (rein geometrisch)
- Effizienz des Schnittes auf rekonstruierte Spuren
- Rekonstruktionseffizienz
- Zerfall geladener und neutraler Hadronen (Gewinn oder Verlust an Spuren, Knicke in Spuren)
- Sekundärwechselwirkungen im Target und im übrigen Detektormaterial
- $e^{\pm}$ Beimischung (vor allem aus der Konversion von γ im Target aus dem Zerfall von π^0)

Die zweite wichtige Korrektur ist diejenige der Verzerrung durch den S4-Auslöser. S4 ist ein kreisförmiger Szintillator, der sich im Abstand von etwa 3.7 m vom Target in der Stahlachse befindet und als Wechselwirkungsauslöser fungiert. Für die Datenaufnahme wird er als Veto verwendet, das heißt, Daten werden aufgenommen, wenn der Szintillator nicht getroffen wird. Letzteres ist vor allem dann der Fall, wenn eine inelastische Wechselwirkung stattgefunden hat, die neue Teilchen mit niedrigerem Impuls erzeugt. Da aber bei der höchsten Strahlenergie (350 GeV/c) in etwa 25% der Ereignisse S4 durch ein Sekundärteilchen getroffen wird, entsteht eine Verzerrung durch den Wegfall von Ereignissen mit bestimmter Ausprägung. In dieser Arbeit wird eine auf Daten beruhende Methode zur Behebung dieser Verzerrung vorgestellt. Dabei werden andere Auslöser, die eine kleinere oder keine Verzerrung aufweisen verwendet um Korrekturfaktoren für die verzerrten Daten zu gewinnen.

Ein weitere Teil der Analyse stellt die Untersuchung der statistischen und systematischen Unsicherheiten dar. In dieser Arbeit werden neben anderen systematischen Unsicherheiten insbesondere die einzelnen Beiträge der Monte Carlo Korrektur aufgeschlüsselt.

Abschließend wird die Normierung erklärt, die beschreibt wie aus Spurmultiplizitäten inklusive Wirkungsquerschnitte zu erhalten sind, und offene Fragen diskutiert.

Zwei der in dieser Arbeit entwickelten Methoden, die Vorgehensweise zur Definition der Akzeptanz und die Korrektur der Verzerrung durch den S4-Auslöser, sind inzwischen Standardmethoden in der NA61 Kollaboration.

Ergebnisse

Die Ergebnisse dieser Arbeit, der differenzielle inklusive Wirkungsquerschnitt negativ und positiv geladener Hadronen in $\pi^- + \mathrm{C}$ Kollisionen bei einem Strahlimpuls von 158 GeV/c und 350 GeV/c, sind in Abbildung 2 dargestellt. Dabei ist die Abschätzung der Gesamtunsicherheit als Fehlerbalken in den Datenpunken zu sehen. Sie beträgt im Mittel 3% mit einem Maximum von 47%. Eine Tabelle, die die Ergebnisse zusammen mit der genauen Größe der Bins und den statistischen und systematischen Unsicherheiten darstellt, befindet sich im Anhang H.

Eines der Hauptziele dieser Arbeit ist es Messungen zu präsentieren, die relevant sind für die Vorhersagen der Wechselwirkungsmodelle bezüglich der Zahl der Myonen an der Erdoberfläche bei Luftschauern. Wie in Abbildung 3 zu sehen ist, deckt die Akzeptanz dieser Studie bei der entsprechenden Energie in weiten Teilen die relevanten Bereiche für KASCADE und für das Pierre Auger-Observatorium ab.

Weiterhin werden in dieser Arbeit die Ergebnisse mit Wechselwirkungsmodellen verglichen, die auch für die Simulation von Luftschauern verwendet werden. Dabei stellte sich heraus, dass keines der aktuellen Modelle Vorhersagen liefert, die die Messungen dieser Arbeit über den ganzen Phasenraum exakt wiedergeben können. Die Gesamtunsicherheit der Messung dieser Arbeit ist in weiten Bereichen deutlich kleiner als die Abweichungen zu den Modellen, die bei einer Größenordnung von 30%, zum Teil aber auch deutlich darüber liegt. Dies legt nahe, dass die Modelle mit Hilfe der aufgezeichneten Daten der $\pi^- + \mathrm{C}$

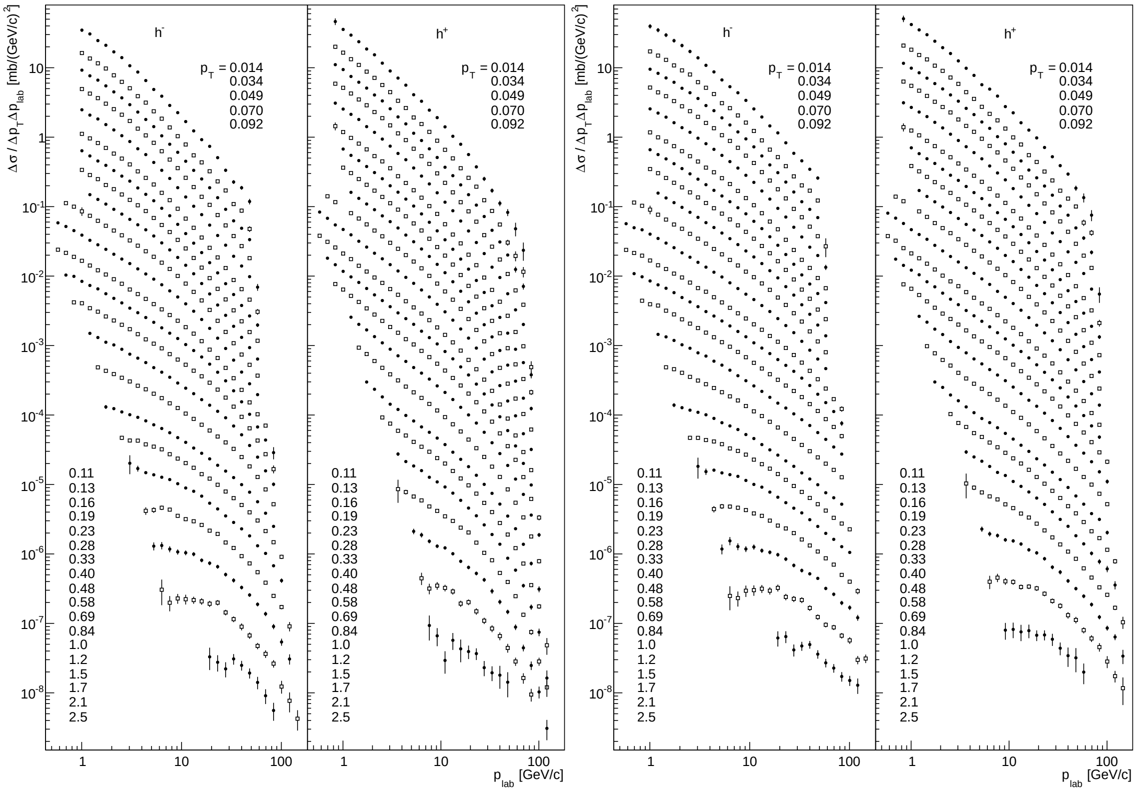

Abbildung 2.: Differenzieller inklusiver Wirkungsquerschnitt negativ und positiv geladener Hadronen in $\pi^- + \text{C}$ Kollisionen bei einem Strahlimpuls von 158 GeV/c (links) und 350 GeV/c (rechts). Die Fehlerbalken zeigen die gesamte Unsicherheit. Außer für $p_T = 0.014$ GeV/c wurden die Datenpunkte sukzessive durch Faktoren geteilt. Sie lauten 6 bis $p_T = 0.034$ GeV/c, 2.5 bis $p_T = 0.11$ GeV/c, 2 bis $p_T = 0.33$ GeV/c und 1.5 bis $p_T = 0.84$ GeV/c. Datenpunkte ab $p_T = 1$ GeV/c wurden nicht durch weitere Faktoren geteilt. p_T ist in Einheiten von GeV/c angegeben. Größere Abbildungen dieser Grafiken finden sich im Ergebnissteil, Kapitel 5.

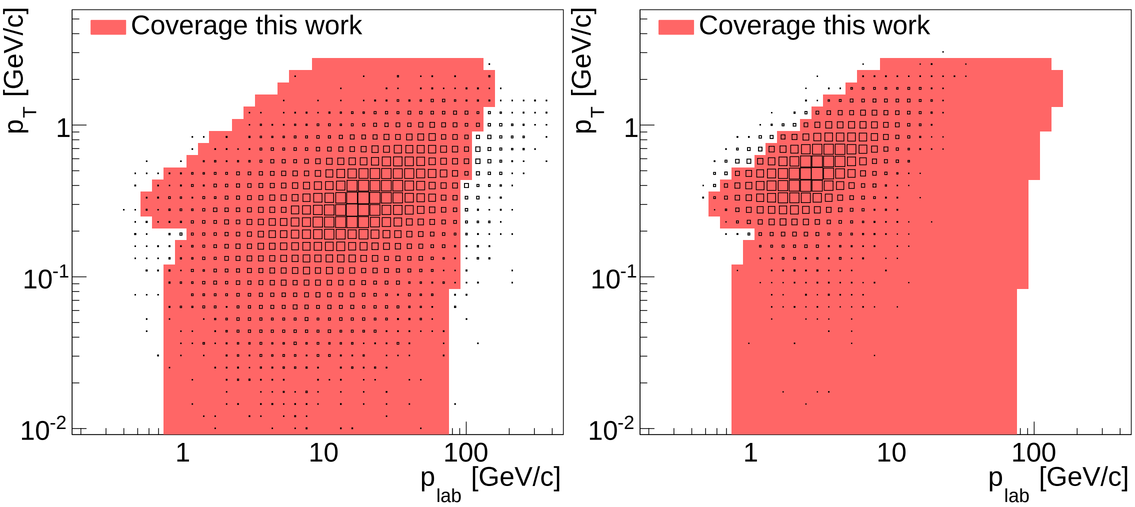

Abbildung 3.: Relevanz der Phasenraumbins (Boxen) für die Zahl der Myonen an der Erdoberfläche für die Experimente KASCADE (links) und dem Pierre Auger-Observatorium (rechts) bei einem Impuls des Projektils von etwa 350 GeV/c. In rot ist die Akzeptanz dieser Arbeit beim Strahlimpuls von 350 GeV/c überlagert. Die Schauersimulation wurde mit QGSJet-II and Fluka durchgeführt. Weitere Grafiken, Beschreibungen und Quellen befinden sich in Kapitel 5.

Reaktion bei einem Strahlimpuls von 158 GeV/c und 350 GeV/c verbessert werden können. Grafiken zum Vergleich der Messergebnisse dieser Arbeit mit den Modellvorhersagen finden sich in Kapitel 5.

Ausblick

Bei dem NA61 Kollaborationstreffen in Budapest, Ungarn (14. - 19. Mai 2012) wurde beschlossen, im Sommer 2012 Spektren geladener Hadronen als vorläufige Ergebnisse zu veröffentlichen. Die vorläufigen Spektren werden dabei maßgeblich auf den in dieser Arbeit vorgestellten Verfahren und Ergebnissen beruhen.

Die Analyse der aufgezeichneten $\pi^- + \mathrm{C}$ Reaktion aus dem Jahre 2009 ist damit allerdings noch nicht beendet. In zukünftigen Analysen wird eine Teilchenidentifikation auf Grundlage des Energieverlusts pro Weglänge der einzelnen Spuren durchgeführt werden. Diese Information ist in NA61 Daten enthalten, wird derzeit aber noch mit neuen Kalibrationskonstanten aufbereitet und konnte deshalb noch nicht in diese Analyse einfließen. Zum einen ließen sich damit die Elektronen auf eine modellunabhängige Weise entfernen, was in der hier vorgestellten Methode einen großen Beitrag zur systematischen Unsicherheit leistet. Zum anderen wird es mit dieser Information möglich sein, jeweils die Produktionsspektren der Teilchen $\pi^\pm$, $K^\pm$, p und $\bar{p}$ einzeln zu bestimmen. Damit erhält man unter anderem den Anteil der Baryonen an der Menge der erzeugten Teilchen, und kann damit die Frage beantworten ob ein erhöhter Baryonenanteil die Lösung des Myonendefizits bei hoch energetischen Luftschauern sein könnte, wie es in [2] vorgeschlagen wird.

Contents

Introduction

Almost 50 years ago, the first ultra-high-energy cosmic rays (UHECRs) were discovered by John Linsley [1]. UHECRs are cosmic rays with a kinetic energy of 10^{20} eV and higher. Cosmic rays are fully ionized nuclei with kinetic energies ranging from the GeV region up to the UHECR region. Many questions regarding their energy spectrum, mass composition and origin are still open and subject to intensive research.

To be able to interpret the measurements of extensive air showers at ground level, it is necessary that the development of the particle cascade is well understood. The collisions that take place in such a cascade are soft hadronic interactions which can currently not be calculated using perturbative quantum chromodynamics. Moreover, the energy of the primary particle is often well above the highest energies created at particle accelerators which leads to the requirement of phenomenological modeling of the cascade. The interaction models use, wherever possible, measurements to verify and adjust their predictions. Nevertheless, measurements are also lacking in the relatively low energy region at the last stages of the cascade.

This low energy region in air showers is of particular importance for the number of muons at ground level because the particles that are created at the last stages of the cascade decay into muons. The number of muons is an interesting observable with several open questions related to it. One of them is the muon deficit of the interaction models with respect to the Pierre Auger Observatory. Another open question is related to the mass composition of cosmic rays calculated from measurements of KASCADE. The calculation is based on the number of electrons and muons at ground level and shower simulations. The outcome of the calculation depends strongly on the simulation model which makes it currently impossible to provide an unambiguous determination of the mass composition at the energy range of KASCADE.

The goal of this work is the measurement of the differential inclusive cross section of negatively and positively charged hadrons in $\pi^- + \mathrm{C}$ collisions at beam energies of 158 GeV/c and 350 GeV/c. The interaction of pions with carbon is similar to the most common reaction in air showers, $\pi^\pm + \mathrm{air}$. Moreover, the energies chosen are relevant for the number of muons at ground level. The measurements of these particle spectra will provide valuable information to improve interaction models and to solve open questions such as those presented above. The interplay between cosmic rays and particle physics will be further discussed in Chapter 1.

The fixed target experiment NA61/SHINE, located at the CERN SPS, is capable of providing relevant measurements for the purpose of improving interaction models in the low energy region. The NA61 detector is a wide acceptance spectrometer with four large volume TPCs designed for the study of hadron production in soft hadronic collisions. In 2009, $\pi^- + \mathrm{C}$ collisions at beam energies of 158 GeV/c and 350 GeV/c were recorded. Chapter 2 explains the basic features of the NA61 detector including its beam line, tracking and timing detectors.

The main part of this work, to be found in Chapter 4, is devoted to the analysis of these data sets and describes how the hadroproduction spectra are obtained from the calibrated and reconstructed data. Selection criteria for events and tracks, target-out subtraction, Monte Carlo and trigger bias corrections, and all steps of the normalization of the production spectra will be described in detail. Emphasis is put on the introduction of a geometrical approach for the definition of the acceptance and on Monte Carlo corrections, for they are of fundamental importance for the type of analysis used in this work. To validate the Monte Carlo simulation, in particular its ability to reproduce the data well and to check the choice of binning, a summary of performance studies that were carried out prior to the analysis is described in Chapter 3. Moreover, the chapter on analysis contains a section on the trigger bias correction, where a data-driven method is introduced that has previously not been used in the NA61 collaboration. A study of statistical and systematic uncertainties concludes this chapter along with a brief discussion of open questions.

Finally, the results are presented in Chapter 5 together with a discussion on the findings and a comparison of the results to current interaction models. A summary of this work and an outlook on future studies can be found in Chapter 6.

1. Cosmic rays and particle physics

The first two sections of this chapter give an introduction to extensive air showers and their measurement. Moreover, open questions in cosmic ray research and the importance of interaction models are presented. In the third section, the origin of muons in extensive air showers is described in more detail. Finally, the importance of the measurements at NA61 for the interpretation of extensive air showers is explained in section Section 1.4.

1.1. Extensive air showers

Extensive air showers, as studied by the Pierre Auger Observatory [3], KASCADE [4], and KASCADE-Grande [5], are initiated by cosmic rays. The primary particle is a nuclei of very high kinetic energies (ranging from $E_0 = 10^{15}$ eV to $E_0 = 10^{20}$ eV or more) interacting with nuclei of the air. Such an interaction is a hadronic collision, resulting in the production of new hadrons which in turn collide again with nuclei of the air. The net effect is a cascade of particles, also known as extensive air shower.

A simple way to describe the hadronic component of such a cascade is the extended Heitler model, see Fig. 1.1. In this model, it is assumed that only pions are produced at each interaction. In addition, the energy fractions are assumed to be exactly 1:1:1 for π^-, π^+, and π^0. As a consequence of their very short life time, neutral pions mostly decay before they interact ($c\tau = 25.2$ nm [6]). Charged pions, on the other hand, have a much longer mean free path at the same energy ($c\tau = 7.8045$ m [6]) and are therefore more likely to interact again.

In the extended Heitler model, the hadronic cascade stops as soon as the energy of the individual particles has dropped below a threshold, the so called decay energy. It is defined as the energy at which the probability of decay and inelastic interaction are equal, thus it is labeled E_{dec}. Since the majority of the hadrons produced in such a shower are pions, E_{dec} can be estimated by comparing the decay length and interaction length of charged pions. In the extended Heitler model, neutral pions do not contribute to the hadronic cascade. The interaction length depends, amongst others, on the density of air. Consequently E_{dec} is dependent on the density profile and, in a more general case, on various model parameters, see [8] for details.

1.2. Observables and open questions

Important physical quantities of extensive air showers are their primary energy, their arrival directions and their mass composition. The knowledge of these parameters has implications

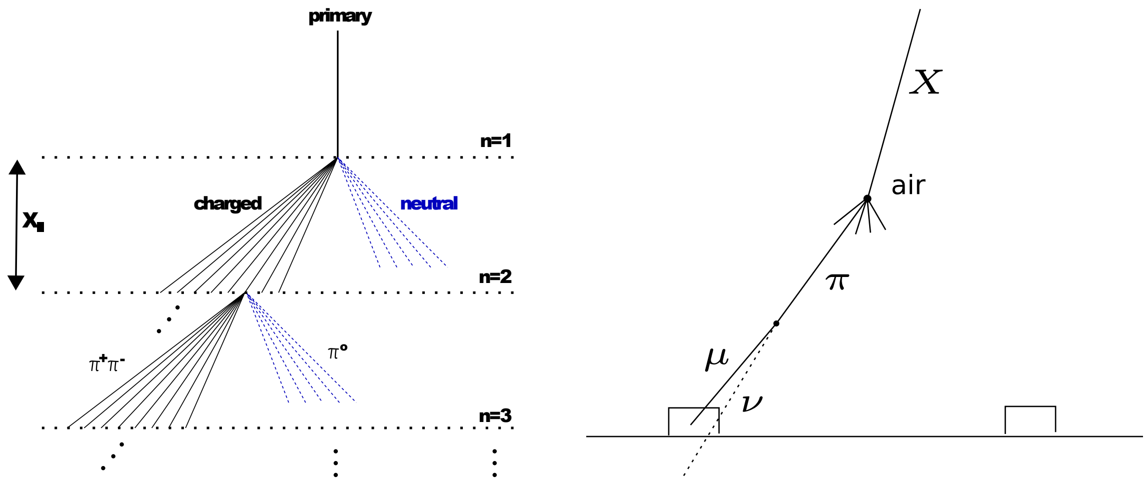

Figure 1.1.: Left panel: Extended Heitler model. Picture extracted from [7]. Right panel: Depiction of the definition of a grandmother particle X, which can be any hadron. The horizontal line symbolizes the ground; the rectangles are surface detectors.

on the astrophysical sources of cosmic rays and their propagation in the universe [9]. The extraction of these quantities turns out to be complicated because observables that are measured at ground level only allow indirect determination of the physical quantities. In this section, two examples of observables that are measured in KASCADE and the Pierre Auger Observatory are presented together with open questions associated to them.

1.2.1. Muon signal in the Pierre Auger Observatory

The surface detectors at the Pierre Auger Observatory measure the Cherenkov light of particles that traverse the water tanks. It is possible to extract a muon yield from this signal, thus measuring the number of muons produced in the extensive air shower. This measurement has led to a long standing open question, the so called "muon deficit of the hadronic interaction models" (short muon deficit). The deficit manifests itself in a discrepancy in the number of muons given the energy scale from the fluorescence telescopes and expectations based on model calculations and the measurements by the surface detectors. The deficit is currently not understood [10].

There are several hypotheses regarding the muon deficit. It might be solved if

1. the low energy interaction models predicted a significantly different particle spectrum,
2. baryons carried away a significant energy fraction to the hadronic component in each interaction or
3. new particle physics took place at the interactions at the highest energies [11].

Up to date, there is not enough evidence that would unambiguously support either of those hypotheses.

1.2.2. Muon and electron signal in KASCADE

The surface detectors of KASCADE measure the electronic and muonic component of an extensive air shower. It is possible to extract the energy dependent mass composition of cosmic rays from those measurements by unfolding the two-dimensional shower size of electron and muon numbers, which contains in every bin a superposition of contributions from different primary particles with varying energies [12]. The task of disentangling the information is challenging and requires intensive use of shower simulations. Hence, the exact mass composition in the energy range of KASCADE is still an open question, see [12] and [13].

As discussed in [12], the outcome of the analysis depends significantly on the high energy interaction model used for the simulation of extensive air showers. The dependence of the outcome on the low energy interaction model seems to be less significant if comparing FLUKA and GHEISA [13]. However, this does not exclude the possibility that the low energy models are important. Moreover, it is plausible that measurements that suggest a change in low energy models will also require changes in high energy models.

This work will provide measurements in the low energy region that can contribute to a better understanding and a clarification of the ambiguous results regarding the mass composition measured by KASCADE.

1.2.3. Interaction models in cosmic ray measurements

As already mentioned above, the interpretation of measurements of extensive air showers requires simulations of soft hadronic interactions. Since this type of reaction can presently not be calculated in QCD, simulations depend on phenomenological modeling. The modeling in turn requires measurements to be accurate and is necessarily based on extrapolations to phase space regions where no data is available. The fact that many interactions cannot, or have not been studied previously to this work, introduces large uncertainties to the models and eventually to the interpretation of extensive air showers.

In fact, the uncertainty in the soft hadronic interaction models is one of the most important limiting factors for interpretations, such as the mass composition or the energy scale [9]. At the Pierre Auger Observatory, the energy scale obtained from the measurements at the surface detectors by means of extensive air shower simulations seems to differ by 25% with respect to direct energy measurements via fluorescence detectors [9].

Current interaction models for soft hadronic interaction come along with rather large theoretical uncertainties. The theoretical uncertainties can be depicted by the fact that competing models predict quite different spectra of charged hadrons, as can be seen later in this work.

There are models, such as EPOS, that have been adjusted in a direction that would partially solve the muon deficit described above. EPOS assumes a baryon fraction higher than most models, see Fig. 1.2. If the ratio of baryons to pions is large, few π^0 are produced in a shower and consequently a large fraction of the total energy stays in the hadronic component. This leads to a production of more low energetic charged mesons and eventually to more muons on the surface.

1.3. Origin of muons in extensive air showers

For the understanding of surface detector measurements, it appears to be customary to call muons that stem from an extensive air shower and reach the detector *daughter particles*. Accordingly, the preceding particle, mostly mesons that decay into muons, are called *mother particles*. The particles that are serving as the projectiles of the last hadronic interaction in the cascade produce the mother particles. They are called *grandmother particles*. An illustration of the definitions can be seen in the left panel of Fig. 1.1.

The impact of grandmother particles on the measured muon yield has been studied in [15], where air showers are simulated for a detector configuration typical for the Pierre Auger Observatory and KASCADE respectively. The simulations with a primary energy of the shower of $E_0 = 10^{15}$ eV (left) and $E_0 = 10^{19}$ eV (right) are shown in Fig. 1.3. The minimum muon energy is 250 MeV (left) and 150 GeV (right). Furthermore, the muons must reach the ground in a lateral distance from the shower core between $r = 40$ m and $r = 200$ m (left) and between $r = 900$ m and $r = 1100$ m (right) to be accounted for. Thus, the left panels correspond to primary energies, lateral extend and detection threshold of KASCADE and the right panel are for parameters relevant for the surface detectors of the

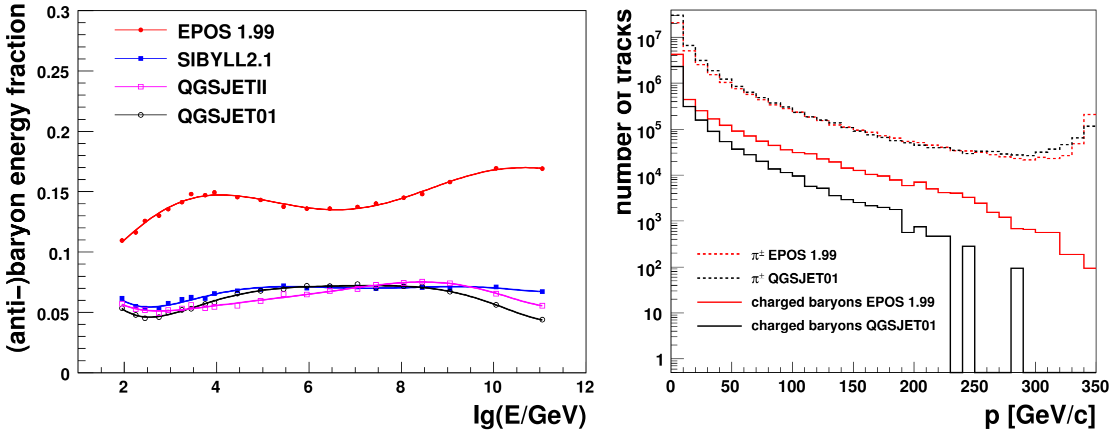

Figure 1.2.: Baryon fraction of produced particles as a function of the projectile energy in $\pi^\pm + \text{air}$ interactions, predicted by different interaction models (left). Spectrum of charged pions and charged baryons in $\pi^- + \text{C}$ interactions at 350 GeV/c predicted by different models (right). Plots taken from [14].

Table 1.1.: Number of triggers recorded by NA61 runs with protons and pions as projectile. The events contain minimum biased and zero biased triggers. Table taken from [14].

	p [GeV/c]	year	$N_{\text{trigger}}[10^6]$
$\pi^- + \text{C}$	158	2009	5.5
$\pi^- + \text{C}$	350	2009	4.6
p + C	31	2007	0.7
p + C	31	2009	5.4
p + p	13	2010	0.7
p + p	20	2009	2.2
p + p	31	2009	3.1
p + p	40	2009	5.2
p + p	80	2009	4.5
p + p	158	2009	3.5
p + p	158	2010	43.9

Pierre Auger Observatory. For comparative reasons, the plots were made with different generator models (QGSJet and SYBILL) and different energy thresholds (80 GeV and 500 GeV) for the transition from the high energy model to the low energy model.

As can be seen in Fig. 1.3, pions are the dominating contribution to the grandmother particles. Moreover, the highest contribution comes from grandmother particles of relatively low energy, beginning at approximately $E = 10$ GeV (right) and going up to $E = 1$ TeV (left).

Due to the geometrical configuration (lateral distance of surface detectors, typical energy range of showers, inclination and height of the maximum of the shower) of the Pierre Auger Observatory and KASCADE it can be concluded that low energy interactions are important for the number of muons at ground level.

1.4. Importance of NA61 for cosmic ray research

NA61 recorded a variety of data sets potentially relevant for the improvement of soft hadronic interaction models. A list is given in Table 1.1. Two dedicated cosmic ray runs, namely $\pi^- + \text{C}$ interactions at 158 GeV/c and 350 GeV/c were performed as well.

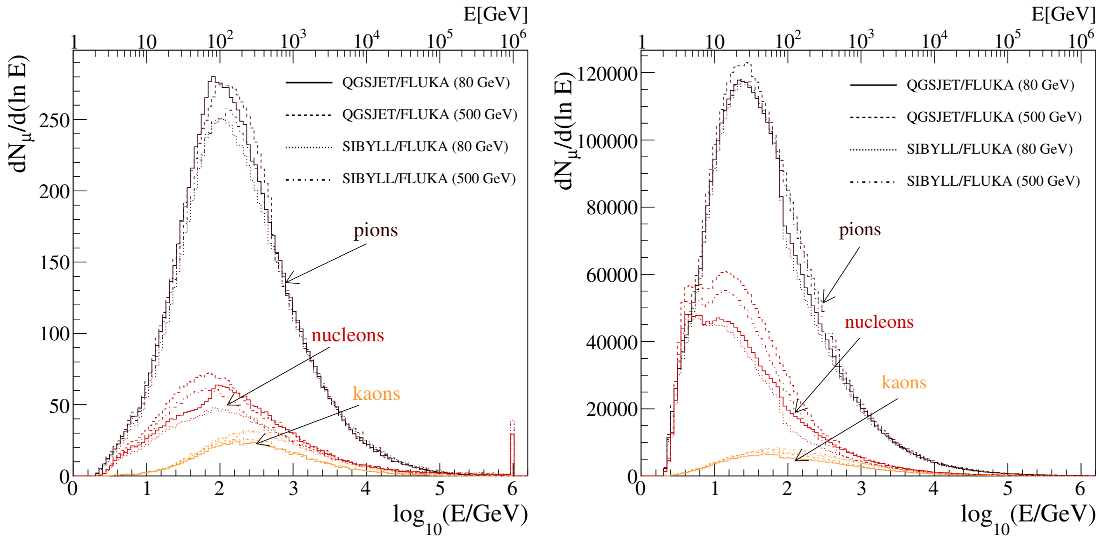

(a) $E = 10^{15}$ eV (b) $E = 10^{19}$ eV

Figure 1.3.: Type and energy distribution of grandmother particles. The y-axis denotes the number of muons resulting from the grandmother particle and measured at a typical configuration of air shower energy and geometry of the detector for KASCADE (left) and Pierre Auger Observatory (right), see Section 1.1. Figures taken from [15].

As presented above, pions at relatively low energies are particularly important for the number of muons on surface detectors. This is the reason why a pion beam was chosen for the cosmic ray runs at NA61. In addition, the selected beam momenta are 158 GeV/c and 350 GeV/c which is well in the region of interest, compare Fig. 1.3.

Another plot showing the importance of the measurements of this work is Fig. 1.4. There, the distribution of mother particles that cause a muon in the surface detectors is plotted against the energy of the grandmother particle.

At NA61, a carbon target was chosen because the collision $\pi^- + \mathrm{C}$ is fairly similar to the most common collision in air showers, $\pi^\pm + \mathrm{air}$, since the primary constituents of air are nitrogen and oxygen which are elements with similar atomic number. In contrast to nitrogen and oxygen, carbon is solid at room temperature which makes it much more convenient to handle as a target. Another reasonably close reaction is $\mathrm{p} + \mathrm{C}$, which is also used to test interaction models.

To date, only very few measurements with $\mathrm{p} + \mathrm{C}$ and $\pi^- + \mathrm{C}$ collisions are available. An overview of existing data and ongoing work in NA61 on pion production is shown in Fig. 1.4.

Apart from the information of particle yields, the cross sections are relevant for air shower simulations as well and are not always known either. A detailed work on cross section measurements was performed in [19].

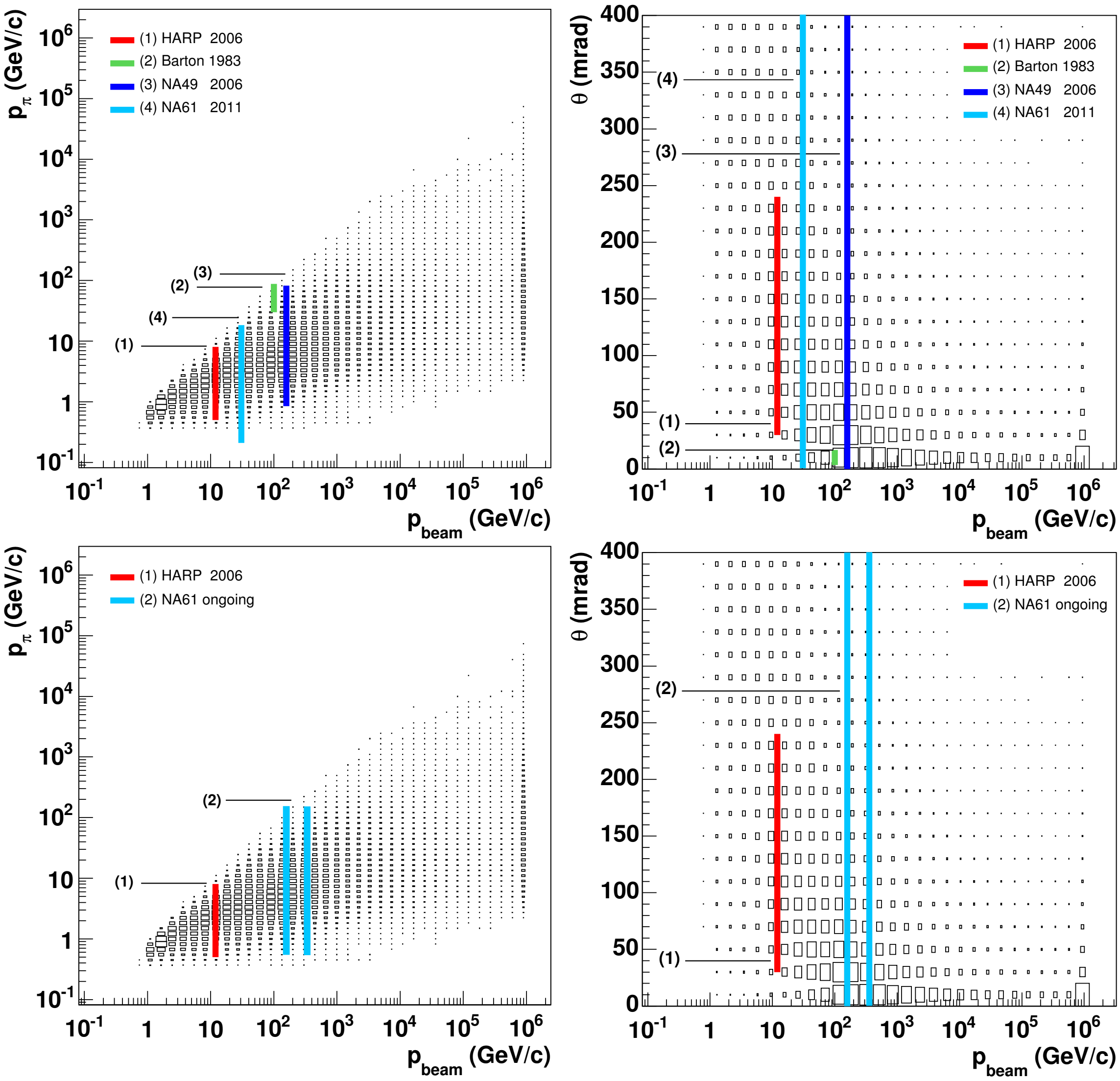

Figure 1.4.: Overview of existing data ([16],[17],[18]) and ongoing work in NA61 on pion production in p + C collisions (top panels) and π^- + C collisions (bottom panels). The box histogram shows the relative importance of the beam energy and secondary pion angle (left panels) and momentum (right panels) for the number of measured muons at ground level in KASCADE. Figures adapted from [16].

2. The NA61 detector

In this chapter, the NA61 detector is described. First, basic facts about the detector, the beam, and its production and surveillance are presented. In the second part, the main components of the detector are explained, including readout electronics, software and reconstruction.

The NA61[1]/SHINE[2] experiment is a fixed target experiment, located at the North Area at CERN[3]. It is provided with a primary or secondary beam from the **S**uper **P**roton **S**ynchrotron (SPS), see Fig. 2.1. A schematic view of the detector can be found in Fig. 2.2. The setup is based on the NA49 detector [20] and has undergone several upgrades. By 2009, a new TPC readout system and the installation of an additional time of flight detector had been finished. More upgrades are currently ongoing [21].

The NA61 detector consists mainly of an instrumented beam line and tracking and timing detectors. Fig. 2.2 is a top view illustrating the main components of the detector. The NA61 coordinate system is defined as follows. The z-axis points along the beam direction. The y-axis points upward. The x-axis points to a the left hand side, when looking along the beam axis. Thus, objects are often labeled *left* if they have coordinates with positive x-values. The individual components of the NA61 detector are explained in the following in more detail.

Beam origin

The SPS is a particle accelerator for protons and nuclei with a maximum momentum of $p = Z \times 450$ GeV/c. Beam momenta smaller than 450 GeV/c and other particle species can be obtained from secondaries created in an inelastic collision. For that purpose, the primary beam is shot on a fixed solid target. Particles with any given momentum smaller than 450 GeV/c can be extracted, guided to the beam lines and finally to experiments such as the NA61 detector.

NA61 is located at the H2 beam line. Secondary hadron beams with a momentum from 100 GeV/c to 360 GeV/c are produced in a setup as described in the following. The primary proton beam of the SPS hits a solid target (named T2) and produces a variety of secondary particles. Only particles with a production angle close to zero are used for the secondary beam. Such particles reach a magnet which bends the trajectories of

[1] **N**orth **A**rea 61
[2] **S**PS **H**eavy **I**on and **N**eutrino **E**xperiment
[3] European Organization for Nuclear Research (formerly known as ***C****onseil* ***E****uropéen pour la* ***R****echerche* ***N****ucléaire*)

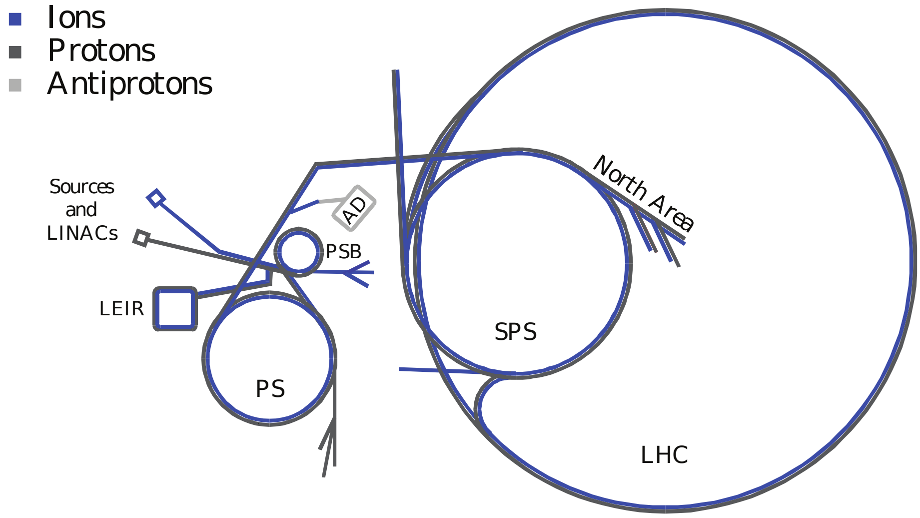

Figure 2.1.: CERN accelerators. NA61/SHINE is located at North Area. Also visible: Antiproton Decelerator (AD), Large Hadron Collider (LHC), Low Energy Ion Ring (LEIR), Proton Synchrotron (PS), PS Booster (PSB), sources and linear accelerators (LINACs), Super Proton Synchrotron (SPS). Figure is not drawn to scale. Picture taken from [22].

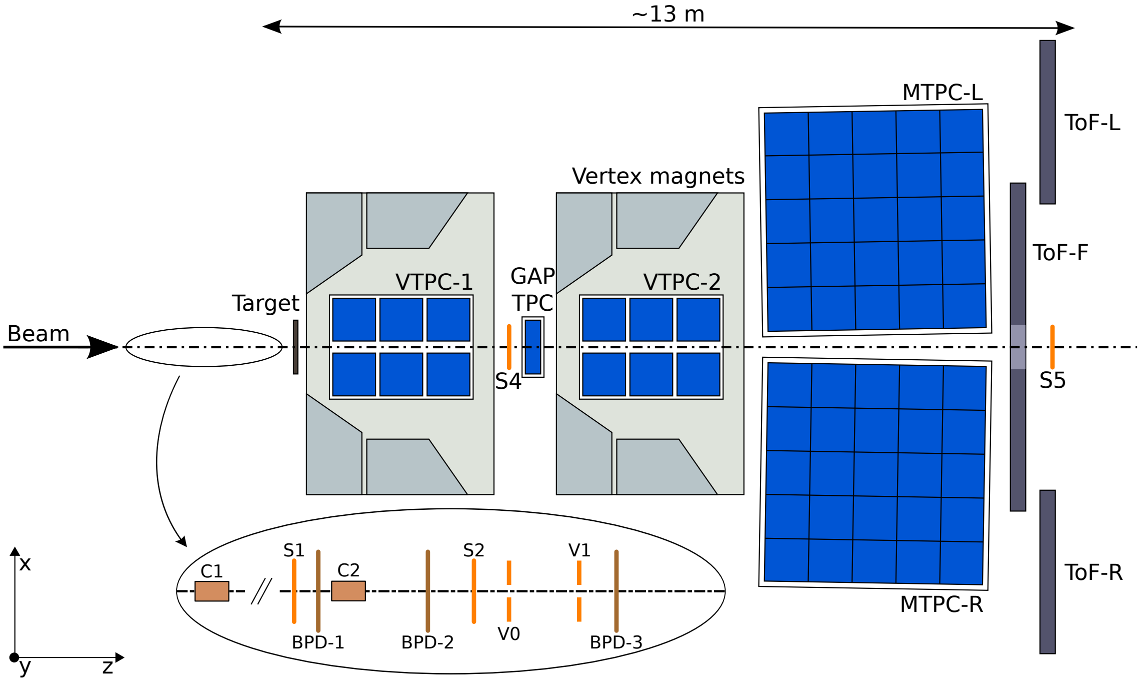

Figure 2.2.: Scheme of the NA61 detector as of 2009. Explanation of the components can be found in Section 2. Figure is not drawn to scale. Picture based on extraction from [23].

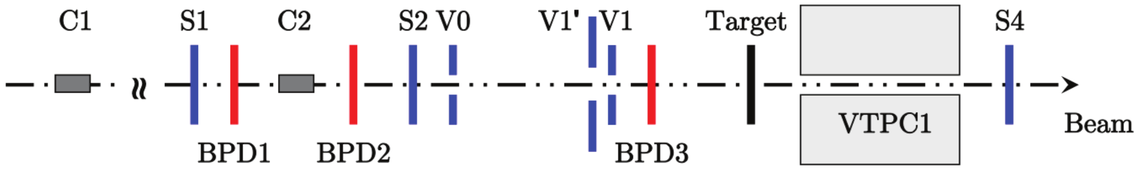

Figure 2.3.: NA61 beam detecotrs. See Section 2.1 for description of the components. Image is not drawn to scale. Picture extracted from [22].

the charged particles. The opening angle depends on the charge and momentum of the particle. By adjusting the polarity and electric current of the magnet, the magnetic field changes accordingly and secondaries of a specific momentum and charge can be selected and directed to a hole in a collimator. Behind the collimator, the beam is directed to the NA61 detector.

In that way, it is possible to obtain a beam of negatively charged particles with a momentum of 158 GeV/c and 350 GeV/c. Since the beam contains all negatively charged secondaries at the particular momentum, the particle identification has to take place at the detector. In the case of NA61, it is done with Cherenkov counters, see next sections.

2.1. Beam detectors

There are numerous target upstream detectors surveying the composition and quality of the beam. Fig. 2.3 illustrates those components. In the following, only the components that are of relevance for the analysis will be discussed in detail.

CEDAR

The **C**herenkov **D**ifferential counter with **A**chromatic **R**ing **F**ocus (CEDAR) [24] is located upstream target in the beam line (labeled C1 in Fig. 2.2) and provides particle identification for the trigger definition or offline analysis.

It consists of a pressure regulated chamber with a set of eight photomultiplier tubes (PMTs) surrounding the beam line. The pressure determines the threshold at which the cone of Cherenkov light emitted by the beam particle hits the PMTs. The PMTs are connected to a trigger logic which can be set to trigger a signal in case of a coincidence of multiple PMTs. For a fixed beam composition and energy, it is possible to plot the Cherenkov signal versus pressure. This is called CEDAR scan and is shown along with fits for the signals of protons, kaons and pions in Fig. 2.4. The height of the fits correspond to the magnitude of contribution of the particles to the total beam composition.

Trigger scintillators

The setup used for data taking of π^-+C interactions contains various scintillators, namely S1, S2, V0, V1', V1, S4, and S5. V0, V1, and V1' are scintillators with a hole to veto large beam divergence. S1 and S2 are scintillators used for the beam trigger. Two more scintillators, S4 and S5 are placed downstream of the target and serve as veto triggers for the definition of T2 and T3 respectively, which are the NA61 interaction triggers. In Fig. 2.2, S4 is visible just before the GTPC and S5 behind the MTPC. S4 and S5 are two identical scintillators with a radius of 1.0 cm.

BPD

The **B**eam **P**osition **D**etector (BPD) is a set of three proportional chambers [26]. Each of the three proportional chambers consists of two wire planes, two cathode readout planes, one central plane and two closing windows. The two layers of readout strips are rotated by 90 degrees to provide two dimensional information of the beam position in transverse

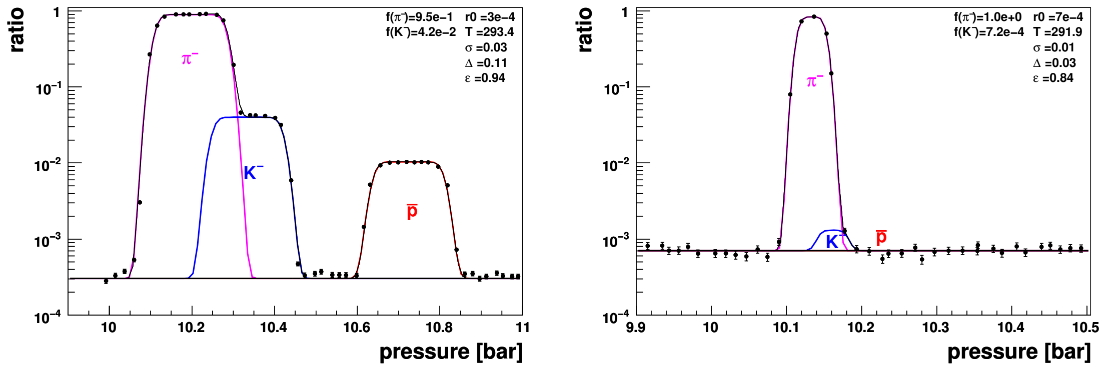

Figure 2.4.: CEDAR scans at 2009 $\pi^- + \mathrm{C}$ runs with negatively charged beam and momentum of 158 GeV/c (left) and 350 GeV/c (right). The plots show the ratio of positive CEDAR trigger to all beam triggers. Plots extracted from [25].

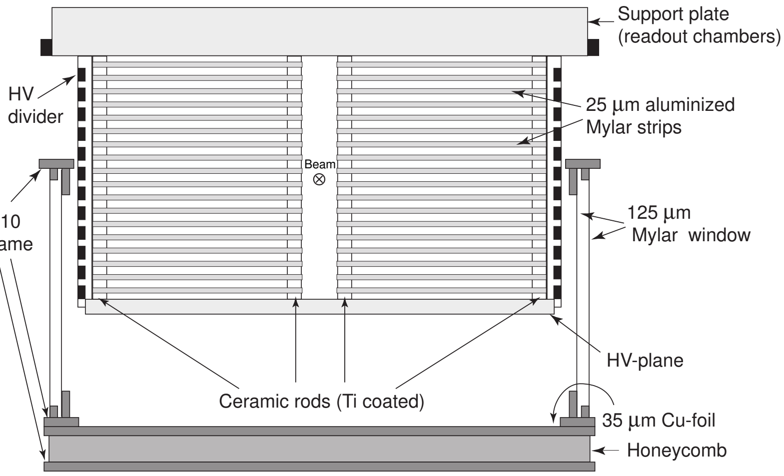

Figure 2.5.: Scheme of a VTPC. Picture taken from [20].

direction. The combination of all BPD chambers makes it possible to reconstruct the direction of the beam, which can eventually be extrapolated to the target and determine the position of impact on the target. The BPD information cannot be used for triggering because its readout time is relatively long.

Target

In the 2009 $\pi^- + \mathrm{C}$ runs, the so called thin target was used. It is made of isotropic graphite with a density of 1.8395 g/cm^2. It is a cuboid with dimensions of 2.5 cm $\times$ 2.5 cm $\times$ 2.0 cm, facing the beam at its thinnest diameter. In the NA61 coordinate system, the center of the target is assumed to be mounted at $z = -681.4$ cm, $x = y = 0$ cm.

2.2. TPC and ToF

The most important component of the detector is a set of **T**ime **P**rojection **C**hambers (TPCs). Two TPCs are within super conducting magnets, they are called **V**ertex TPC 1 and 2 (VTPC-1 and VTPC-2). Between VTPC-1 and VTPC-2, the so called **G**ap TPC (GTPC or GAP TPC) can be found. Further downstream, and outside the magnetic field, the largest TPCs, named **M**ain TPC **L**eft (MTPC-L) and **M**ain TPC **R**ight (MTPC-R) are located. Often the two MTPCs are considered to be a single detector, referred to as MTPC. Fig. 2.2 depicts the positions of the TPCs in relation to other components of the detector.

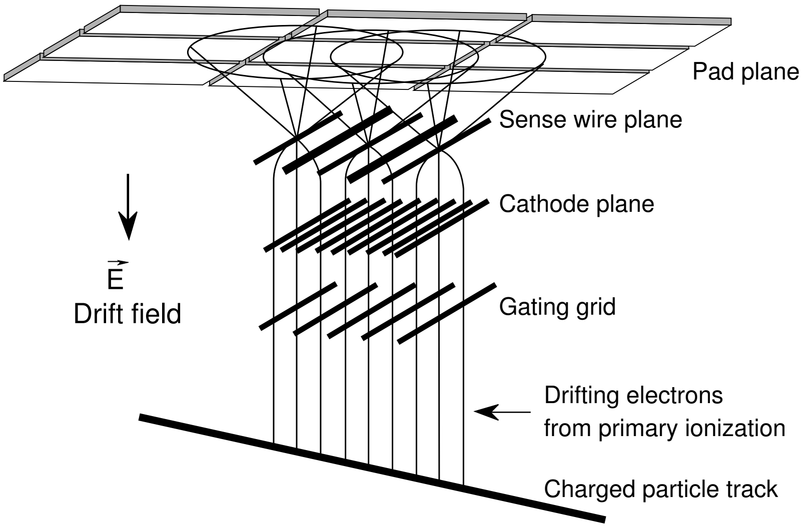

Figure 2.6.: Scheme of the TPC readout. A charged particle ionizes the gas along its trajectory. The electrons from primary ionization then drift vertically upwards in the electric field. Picture from [20].

The idea of a TPC is to project (hence the name) the trajectories of traversing particles on the readout plane. This projection is achieved by drifting elections and ions in an electric field. Furthermore, the time of the arrival of drifting charges is recorded which provides information on the original distance between the charge and the readout plane.

The sensitive volume of a TPC is within an enclosed container, surrounded by an apparatus creating an electric field and providing readout of the signals. The container is filled with a specific gas which ought to have properties beneficial for ionization and transportation of charged particles, in particular regarding drift velocity, diffusion coefficient, and electron attachment. The gas mixture used in the VTPCs and GTPC is Ar/CO_2 (90/10) and Ar/CO_2 (95.5/5.5) in the MTPC. More details on the gas system can be found in [20] and [22].

The electric field strength within the sensitive volume of a TPC is of the order of several kV/m. Aluminized mylar strips around the chamber, which carry different potentials, assure a very homogeneous electric field inside the TPC. The drift velocity in the sensitive volume is then constant and distances y are proportional to the drift time. Typical values are 1.4 cm/μs for the VTPCs, 2.3 cm/μs for the MTPC and 1.2 cm/μs for the GTPC.

Charged particles that traverse the TPC ionize gas molecules along their trajectory through the TPCs. The released electrons then drift vertically upward along the electric field, see Fig. 2.5 and Fig. 2.6. Ions move in the opposite direction.

The drifting elections then reach the so called gating grid, a set of wires which can be set to different potentials to either allow the electrons to pass or to stop them. During readout of the TPC, the potential in the gating grid is set equal to the local vertical electric field potential, thus electrons pass without being disturbed.

To prevent ions from drifting back into the sensitive volume, the gating grid is closed whenever there is no readout. The wires of the gating grid are then alternately put on plus and minus 100 V with respect to the local field.

The cathode wires are at 0 V and are located behind the gating grid. The drift volume ends at the cathode. Between the cathode and the sense wires, the electric field is much higher than in the drift volume so that it becomes an amplification region. This means the electrons are accelerated rapidly and collide with gas molecules and atoms, consequently the electrons ionize more gas. The result is an avalanche which eventually produces a large number of electrons and ions. The electrons are absorbed in a short time by the sense wire, whilst the ions are much heavier and slowly drift back slowly to the gating grid. As soon as the electrons are absorbed, the ions represent an abundance of a positive charge, thus inducing an opposite charge in the readout pads. This induced charge is the actual signal which is readout by the electronics. More on TPCs and their readout system can be found in [27].

The three dimensional position of the original charge created by the traversing particle is determined by the drift velocity in y-direction and by the position of the readout pads in x and z-direction. Such a charge with information of the position is called cluster.

In addition to the position, the amplitude of the charge of a cluster is measured. This information is relevant for particle identification via their specific energy loss. The specific energy loss (in the following called $\mathrm{d}E/\mathrm{d}x$) of a charged particle in matter is characterized by the Bethe Bloch formula [28] and depends primarily on the mass, charge, and momentum of the particle. This makes $\mathrm{d}E/\mathrm{d}x$ information very valuable to distinguish between different particle species such as $e^{\pm}$, $\pi^{\pm}$, $K^{\pm}$, p, $\bar{p}$, and heavier nuclei.

In total, the TPC readout system contains 182000 pads. The pad length is 16 mm and 28 mm in the VTPCs and 40 mm in the MTPC. The pad width is 3.5 mm in the VTPCs and between 3.6 mm and 5.5 mm in the MTPC. To optimize the resolution in $\mathrm{d}E/\mathrm{d}x$ measurements, the pads are aligned in a way that RST traverse the pads at their maximum length. The overall spacial resolution of TPCs is about 200 μm [20].

Furthermore, the NA61 detector contains various **T**ime **o**f **F**light detectors (ToF). As the name implies, they measure the time it takes a particle to travel a certain distance. Together with the information of momentum, the mass of the particle can then be computed. The ToF in forward direction (ToF-F) is a wall made of scintillators, each connected with one PMT on top and one on the bottom. The ToF on the right and left (ToF-R and ToF-L) are so called pixel scintillator arrays. They provide a spacial resultion in x and y direction. As of 2009, the ToF in forward direction (ToF-F) is the most recently installed ToF.

2.3. Reconstruction and calibration procedures

When a main trigger signal is fired, the data taking procedure starts and the information from all parts of the detector have to be collected and recorded. Such unprocessed data is called raw data. Numerous computer processing steps have to be applied on the raw data to extract the information that is wanted for analysis. This procedure is called reconstruction.

The outcome of the reconstruction is determined by many parameters, which have to be calculated on the basis of external measurements (for example pressure and temperature in the TPCs for determining the drift velocity), or on the basis of recorded data from the detector (e.g. corrections of the precise position and orientation of the TPCs by means of all recorded cluster positions). This process is called calibration.

An important part of the reconstruction is the track reconstruction. As described above, every charged particle traversing the TPCs produces trail of ionized gas along its trajectory, which is read out as a series of clusters by the electronics. The track reconstruction combines those clusters to tracks. It is aware of the magnetic field and can therefore fit a curve through every series of clusters. Fig. 2.7 is an example event illustrated in the event browser and depicts the basic concept of tracks and cluster in the NA61 detector.

Tracks from the main vertex, so called main vertex tracks, usually begin at the target and exit the detector at the sides or the downstream end. Additionally, there are tracks beginning downstream of the target. For example, if a neutral particle decays into two charged particles, it produces a relatively well defined pattern. Such a decay is called V_0.

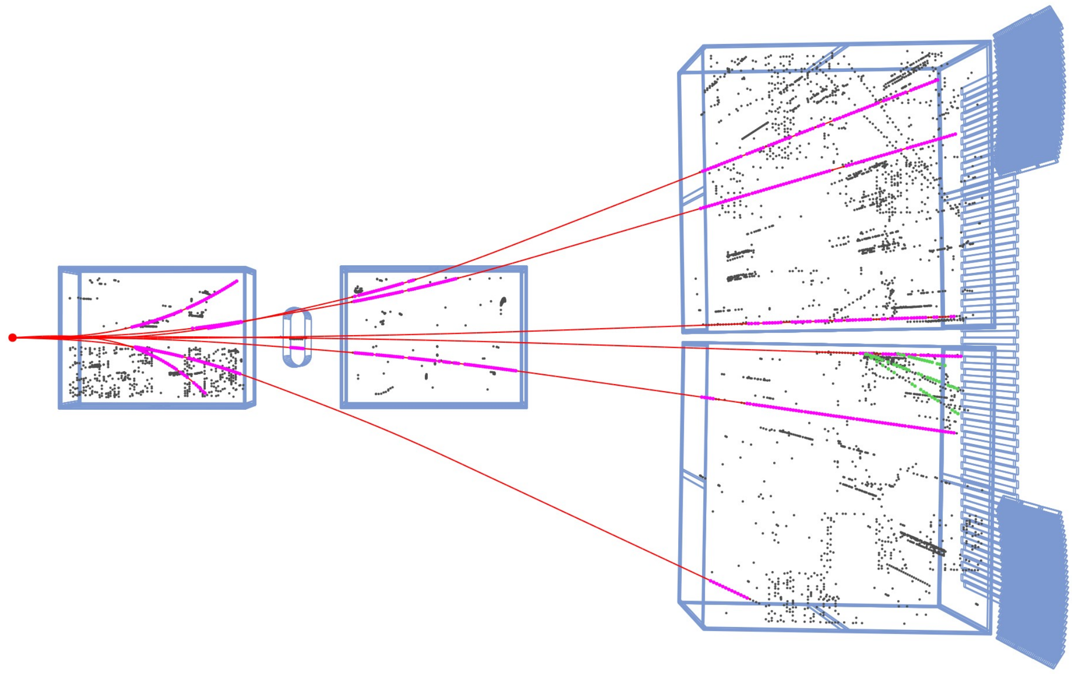

Figure 2.7.: Example event from $\pi^- + C$ run at 350 GeV/c beam momentum. Color code: magenta: clusters assigned to main vertex track; green: clusters assigned to track but not main vertex track; black: clusters without assignment to track; red: reconstructed main vertex tracks

It also occurs that tracks start or end without any obvious reason, or that track fragments of different TPCs cannot be matched to a global track. Such cases lead to inefficiencies or to additional tracks.

Generally the efficiency of the track reconstruction in reactions with low multiplicity is very close to 100% [20], with the exception of geometrical edges of the detector and low energetic tracks that are "on the wrong side" with respect to the magnetic bending. More details on those so called wrong side tracks will be presented in the next chapter. A high overall efficiency can be ensured by selecting bins in phase space that have an intrinsically high reconstruction efficiency, see Section 4.2.3.

Momentum and charge is assigned to every successfully fitted track. If a track has been assigned to the main vertex, in a second step, the reconstruction constrains the origin of the track to the main vertex. The momentum and charge is then recalculated and a more precise result is found. In the context of the Shine $\overline{\text{Off}}\underline{\text{line}}$ Framework [29], tracks with a vertex constraint are called vertex tracks, those without are called tracks. If a vertex track is constrained by the main vertex, it is called main vertex track.

3. Performance studies of detector and simulation

This chapter presents some of the performance studies of the detector and simulation that have been done during the course of this work. The first section focuses on momentum resolution, which is important to justify the chosen binning. In the next step, an interesting observable, the distribution of fitted main vertices along the z-axis is discussed and compared with Monte Carlo. The last section of this chapter deals with cluster distributions and presents yet another comparison of Monte Carlo and measured data, since a good agreement of Monte Carlo and data is crucial if Monte Carlo corrections are applied on the data, as explained in the analysis chapter.

3.1. Momentum resolution

The momentum resolution depends on the local spacial resolution of the track reconstruction and the track topology itself and is approximately Gaussian in $1/p$. It is generally seen as very good, typical values are between $\mathrm{d}p/\mathrm{d}p^2 = 0.3 \cdot 10^{-4}(\mathrm{GeV/c})^{-1}$ and $\mathrm{d}p/\mathrm{d}p^2 = 7.0 \cdot 10^{-4}(\mathrm{GeV/c})^{-1}$, depending on the track topology [20].

It can explicitly be studied by means of Monte Carlo simulations. The following study shows results in the case of 350 GeV/c beam momentum. The case of 158 GeV/c beam momentum is then covered too, since the magnetic field and all other settings were the same in both runs.

A very practical way to study the momentum resolution is to look at the magnitude of migrations from one bin to another, see Fig. 3.1 and Fig. 3.3. A track with a certain momentum has migrated if the reconstructed momentum falls into another bin than the simulated momentum. For that purpose, the study of momentum resolution is done in the same kinematic variables and the same binning as used in the analysis of this work.

A positive migration in a particular bin shall denote a gain of reconstructed tracks in this bin, whilst negative migration refers to the loss of reconstructed tracks in a certain bin. In both cases, only tracks that are successfully reconstructed and pass all quality cuts are counted, which assures that no other detector effects influence the measurement of migration.

Naturally, always both types of migration occur since the momentum resolution is finite. If the momentum resolution is good, positive and negative migrations are low. The inverse is correct as well, thus the study of migration is a way to estimate the momentum resolution with respect to the bin size, assuming that the contribution from the shape of the particle spectrum in p and p_T is not dominating the migration.

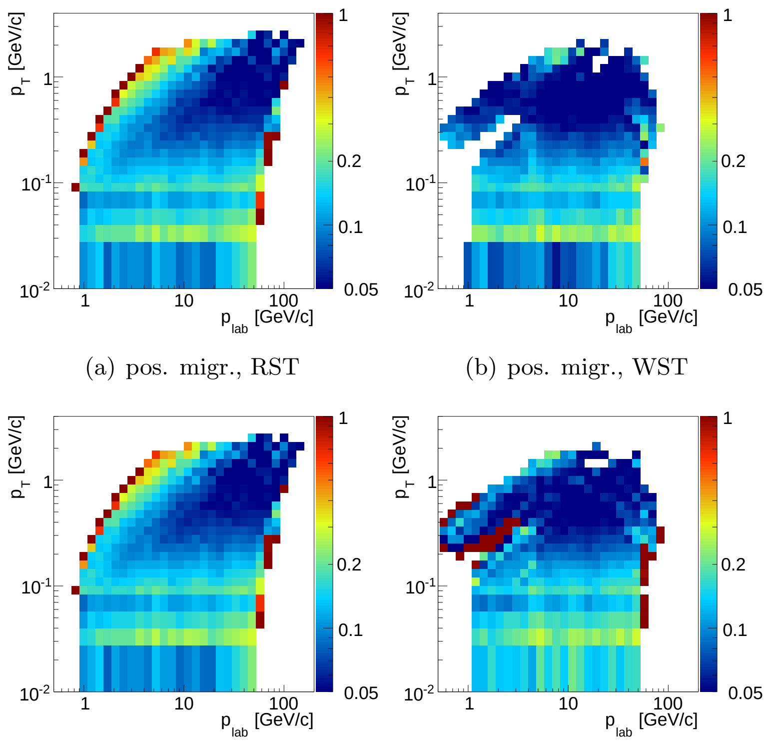

(a) pos. migr., RST (b) pos. migr., WST

(c) neg. migr. RST (d) neg. migr. WST

Figure 3.1.: Positive and negative migration of negative RSTs and WSTs. Plots produced from 10^6 Monte Carlo (VENUS) events at 350 GeV/c beam momentum. Note: lower edge of z-axis refers to less than or equal to 0.05.

The momentum resolution depends on quality cuts of tracks and also on the track topology. It is possible that different track topologies have a significantly different momentum resolution, even if all quality cuts are applied. To check this, tracks have been divided into subsamples, depending on the TPCs they have passed, their charge, and also if they are right side tracks (RST) or wrong side tracks (WST). See Fig. 4.2 for definition of RST and WST. RST are called right because they cross the tilted pad planes at a perpendicular direction, which is optimal for the readout of the charge distribution. WST, on the other hand, cross the pad planes at a suboptimal angle. Taking VTPC1, GTPC, VTPC2, and MTPC into account, the theoretical number of TPC combinations is $2^4 = 16$. Some combinations are impossible, or do not practically occur. Since the total number of track topologies is then very large, not all of them are shown. The plots presented in this work however cover the cases exemplarily. Since it is sufficient to prove that the momentum resolution is not the limiting factor of the bin size, this is a reasonable approach for the study of momentum resolution.

The relationship between migration and resolution can be studied by looking at Gaussian distributions. Assuming particles are uniformly distributed within a bin in momentum and the momentum resolution is of Gaussian form (which is an approximation), one can calculate the negative migration for any fraction of bin width to momentum resolution.

This is done for the one dimensional case and shown in Fig. 3.2. Fig. 3.2(b) shows the method of calculation for a particular bin. The particles are generated uniformly over a bin of width = 8 (ranging from -4 to +4). The reconstructed value, e.g. the value filled in the histogram, follows a Gaussian distribution with $\sigma = 0.66$, meaning $\frac{\text{bin width}}{\sigma} = 12$.

In the two dimensional case, where the bin size is limited by the momentum resolution in two variables, the negative migration is greater than in the one dimensional case. Thus

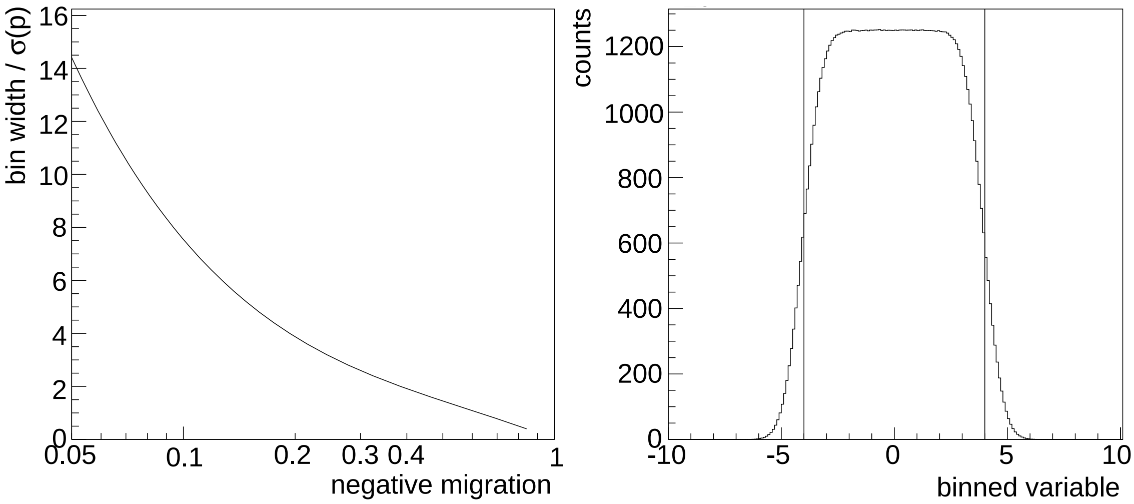

(a) (b)

Figure 3.2.: Negative migration and the relationship to momentum resolution in the one dimensional case. (a) Functional dependency of $\frac{\text{bin width}}{\sigma}$ to negative migration. (b) Calculation of negative migration in a bin with $\frac{\text{bin width}}{\sigma} = 12$ and $\sigma = 0.66$.

the one dimensional case is a conservative estimate for the relation shown in Fig. 3.2(a).

As can be seen in Fig. 3.2(a), the momentum resolution is better than the bin size if the migration is less than approximately 35%. To be exact, this means the bin width is twice the standard deviation of the Gaussian distributed reconstructed momentum in both kinematic variables independently. Henceforth, the choice of binning is reasonable with respect to momentum resolution if the migration is less than 35%.

Fig. 3.1 and Fig. 3.3 illustrate the negative and positive migration. Bins that are colored dark blue have a migration of less than 5%. As can be seen, the migration is generally very low, consequently the width of the bins is much bigger than the momentum resolution. The value 35% is almost never topped. In the plots of negative migration (Fig. 3.1(c) and Fig. 3.1(d)), some bins at the borders of the acceptance have values of 1. Those bins do not actually have acceptance in the reconstruction (compare the positive migration Fig. 3.1(a) and Fig. 3.1(b)). Thus they drop out in the analysis and are no reason for concern. In that sense, the binning is well justified and no further action regarding the finite momentum resolution is needed.

3.2. Fitted main vertex

The distribution of the fitted main vertex is a good cross check to validate the principal of the target-out subtraction and compare the overall agreement of Monte Carlo simulation with real data recordings.

Target-out subtraction

In the beam line and the sensitive volume, there is necessarily a non-negligible amount of matter. This includes gas (air and TPC gas) and solid material such as the entrance and exits of TPCs, support structures, magnets, and so forth.

The cumulative effect of this matter can be studied by so called target-out runs. A target-out run is a run with an identical setup to an ordinary run but the target is removed from its support. As can be seen in Fig. 3.4, the distribution of fitted main vertices along the z-axis is significantly different in target-in and target-out runs. Target-out runs show a flat distribution around the position of the target (right panel in Fig. 3.4).

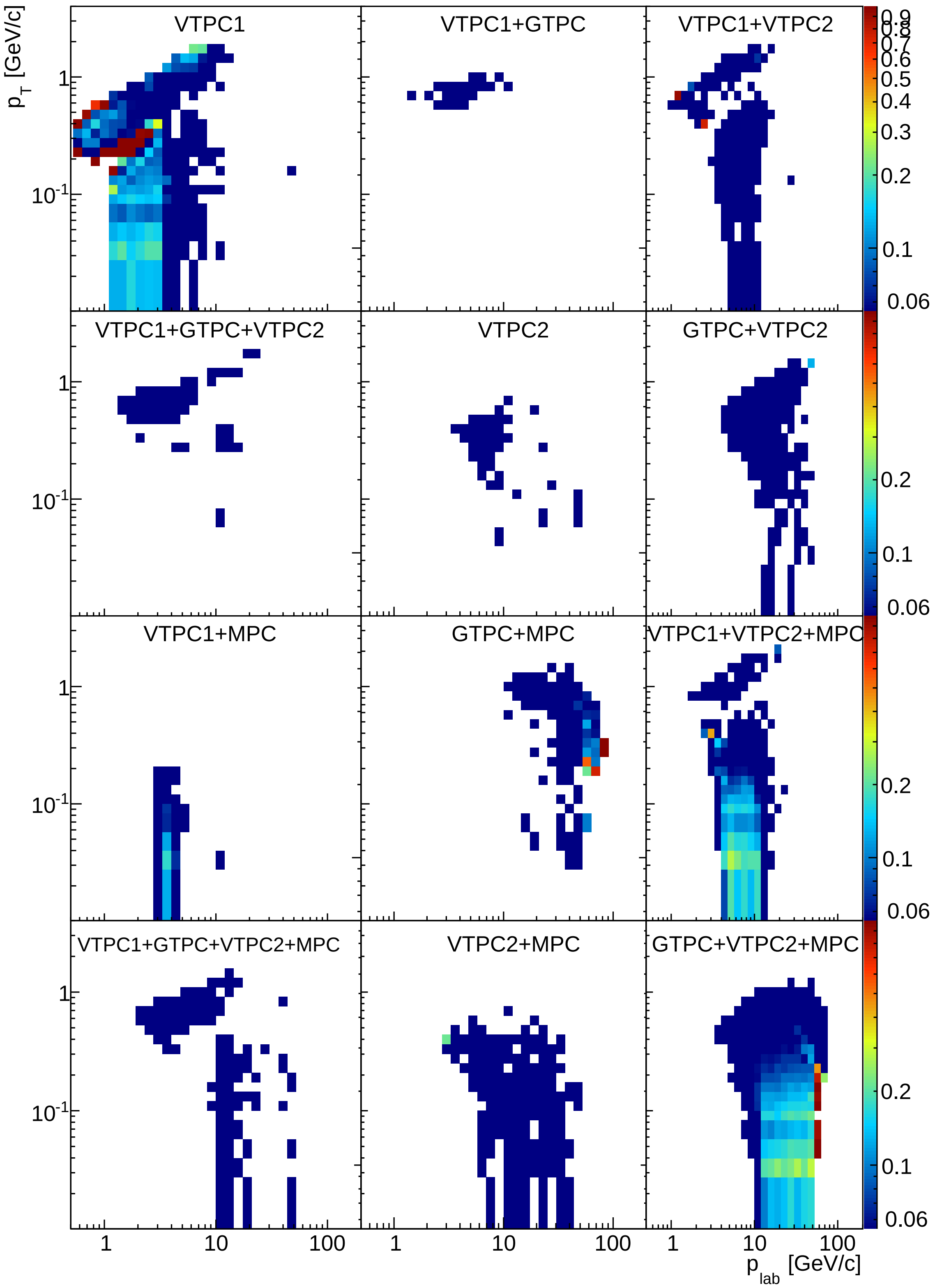

Figure 3.3.: Negative migration of negative WSTs for various TPC topologies after all quality cuts. Plots produced from 10^6 Monte Carlo (VENUS) events at 350 GeV/c beam momentum. Note: lower edge of z-axis refers to less than or equal to 0.05.

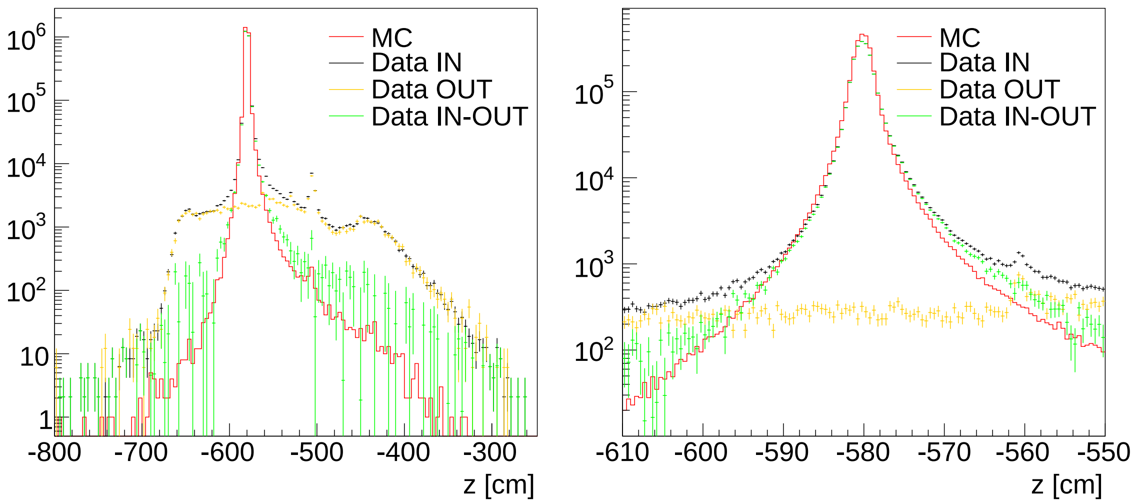

Figure 3.4.: Number of fitted main vertices in $\pi^- + \mathrm{C}$ interactions at 350 GeV/c as a function of z in the NA61 coordinate system. MC: Monte Carlo simulation, IN: Target-in, OUT: Target-out, IN-OUT: Target-out subtraction is applied. Left panel: Full range. Right panel: Magnification of range around the target. Data and Monte Carlo simulations are T2 triggers.

The procedure of subtracting the contribution of additional matter in the detector from the target-in runs is called target-out subtraction, as explained in the analysis chapter, Section 4.3. The result is a data set that exclusively contains information about processes caused by the target. The green data points in Fig. 3.4 are data points with target-out subtraction applied. The result is an almost symmetric and very narrow distribution around the position of the target at $z \approx -581$ cm, as it is expected.

Agreement of Monte Carlo and data

The reconstruction of the fitted main vertex is based on information from main vertex tracks and the BPD extrapolation. The quality of the fit increases with the track multiplicity and is furthermore dependent on the production angle and the number of clusters of tracks. Fig. 3.4 displays the distribution of fitted main vertices along the z-axis. The maximum of the distribution is at the location of the target, $z \approx -581$ cm. After target-out subtraction (green data points), the Monte Carlo simulation (red line) shows a good overall agreement. The similarity of the distribution of the fitted main vertex is an important feature demonstrating the fact that the detector is well reproduced in simulated data. Also it indicates that the simulated event topology, such as track multiplicity, is realistic.

3.3. Distribution of secondary vertices

The distribution of secondary vertices is also an interesting observable to study when evaluating the quality of a Monte Carlo simulation.

The top panel in Fig. 3.5 depicts the distribution of secondary vertices along the z-axis. The plot shows that the data points (black) are generally in good agreement with the Monte Carlo prediction (red). In particular, the largest peaks are present in both cases. Differences are apparent at some of the minor peaks which are only visible in data. Those peaks are support structures of the TPCs and the scintillator S4 that are not simulated in Monte Carlo. A two dimensional comparison of data and Monte Carlo simulations is found in the centered and bottom panel of Fig. 3.5 along with a explanation of the characteristic peaks in Table 3.1. Another discrepancy is the excess of secondaries close to the target and up to $z \approx -500$ cm. Those secondaries are suspected to be primary off-time particles,

Table 3.1.: Explanation of characteristic peaks in distribution of secondary vertices (Fig. 3.5).

z [cm]	Explanation
-592	Tracks from the main vertex
-498	Entrance of VTPC-1
-382	Support structure of VTPC-1
-260	Exit of VTPC-1
-210	Support of S4
-200	Entrance of GTPC
-175	Exit of GTPC
-118	Entrance of VTPC-2
2	Support structure of VTPC-2

which are more than $\Delta t = 25\ \mu$s displaced in time with respect to the main trigger [30]. Since their tracks are well separated in y-direction from the main vertex and identified as tracks from a secondary interaction, they do not interfere with the measurement of tracks from the main vertex.

Cluster distributions

Fig. 3.6 displays the distribution of the number of clusters of reconstructed tracks before and after the acceptance cut (Section 4.2.3). The Monte Carlo curve (red) shows several distinct peaks. Every peak corresponds to a track topology with passage trough a certain combination of TPCs. The maximum number of clusters of a VTPC is 72, of a MTPC it is 90, and of the GTPC it is 7, see [20] for more details. The data points (black) also show peaks but they are smoothed out towards smaller values. This is an expected behavior and comes from the fact that the real detector suffers from imperfections (such as noise or undetected broken pads) in the TPC system that are not simulated. Thus real data tracks have generally less clusters than tracks in Monte Carlo. However, the general agreement between data and Monte Carlo is very good. In the next chapter, a method of defining the geometrical acceptance will be introduced. It minimizes the dependence of the analysis of the exact description of the data by the simulation.

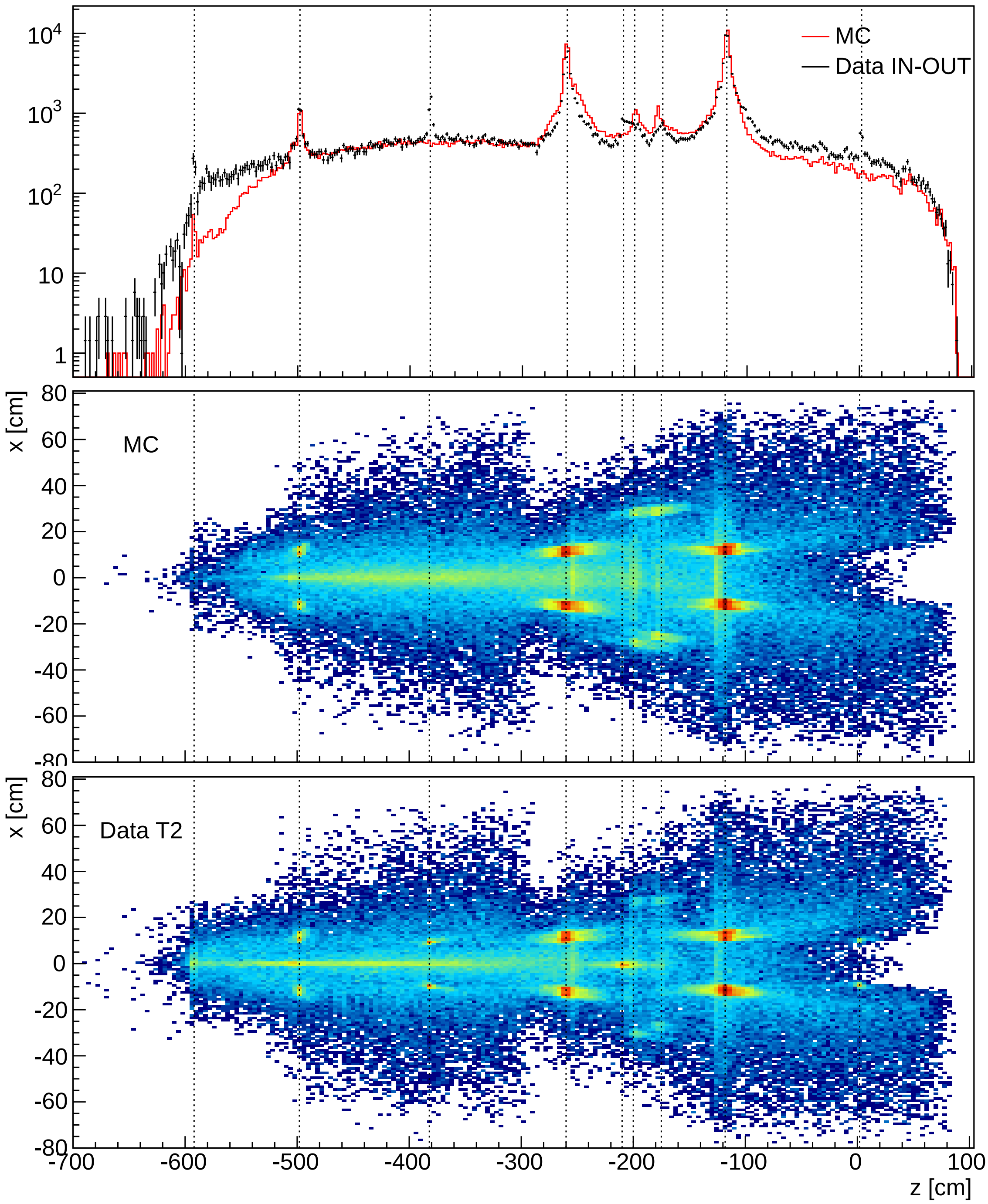

Figure 3.5.: Number of secondary vertices in $\pi^- + \mathrm{C}$ interactions at 350 GeV/c as a function of z in the NA61 coordinate system. Top panel: One dimensional distribution with labels MC: Monte Carlo simulation, Data IN-OUT: Data with target-out subtraction applied. Data and Monte Carlo simulations are T2 triggers. Centered panel: Two dimensional distribution of secondary vertices obtained from simulations. Bottom panel: Two dimensional distribution of secondary vertices obtained from measurements. A maximum WFA cut (no more than one beam particle within the time window) is applied on the data.

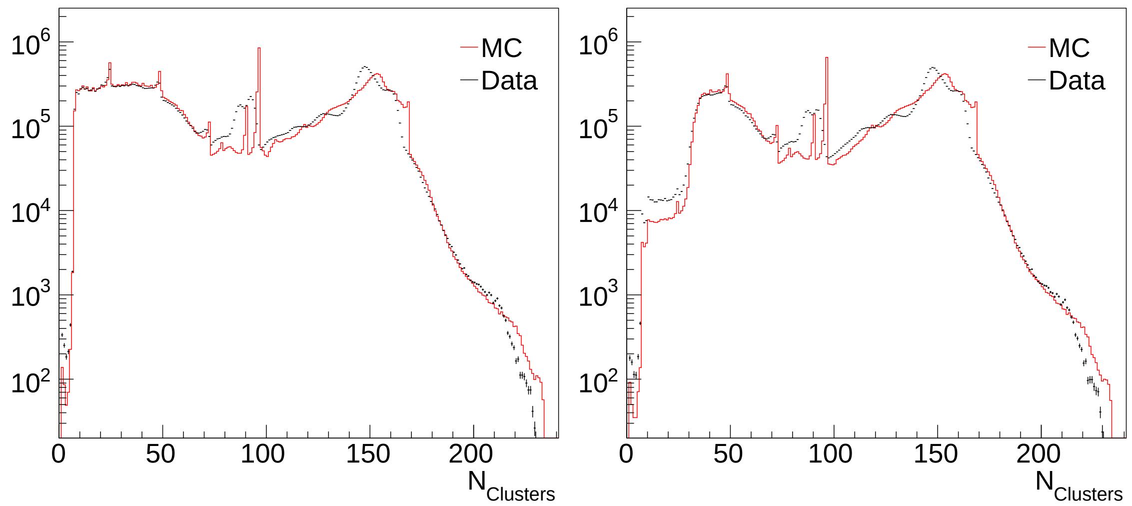

Figure 3.6.: Number of clusters of reconstructed tracks in data and Monte Carlo in $\pi^- + \mathrm{C}$ interactions at 350 GeV/c. Left panel: Before acceptance cut. Right panel: After acceptance cut. No other quality cuts are applied on the reconstructed tracks.

4. Analysis

This chapter deals with the analysis of the data. Analysis is, in a simplified manner, the process of selection and manipulating recorded data to obtain physical distributions of interest. The method used in this work is the so called charged hadron analysis. The goal of this method is to obtain differential cross sections of positively and negatively charged hadrons. The type of particle of the hadrons is irrelevant. The cross sections are obtained from the hadron multiplicities which are in turn calculated from the track multiplicities by means of Monte Carlo corrections. This correction, which removes leptons, is small a the majority of tracks are hadrons.

In the first section, the data used in this analysis is explained. The second section deals with the selection criteria of events and tracks. After a small section on target-out subtraction, two of the main parts of the analysis are described, the Monte Carlo and trigger bias corrections. A section on normalization concludes the calculation of the spectra. Finally, the study of systematic uncertainties is discussed and remaining open questions are stated.

4.1. The data sets

4.1.1. Experimental data

In both $\pi^- + \mathrm{C}$ 2009 runs, data was taken with three different main triggers. They are called T1, T2 and T3. T1 is the so called beam trigger. It fires a signal whenever a beam particle passes the beam detectors. The precise beam definition for those runs is:

$$T1 = S1 \wedge S2 \wedge \overline{V0} \wedge \overline{V1} \wedge \overline{V1'} \tag{4.1}$$

See Fig. 2.3 for the positions of the scintillators.

T2 is a so called interaction trigger. It is supposed to fire a signal when an inelastic interaction has taken place. The definition of T2 is

$$T2 = T1 \wedge \overline{S4}\,, \tag{4.2}$$

with $S4$ being the signal from the scintillator S4 which is located in the beam axis just before the GTPC. As explained in Section 2.1, it is a circular scintillator with a radius of one centimeter positioned at a distance of approximately 369 cm [19] from the target. If no interaction has taken place, the beam is not diverted and will hit S4. In case of an inelastic interaction, new particles are produced. Their momenta are, in general, much smaller than the original beam particle. In the magnetic field, the trajectories of those particles are

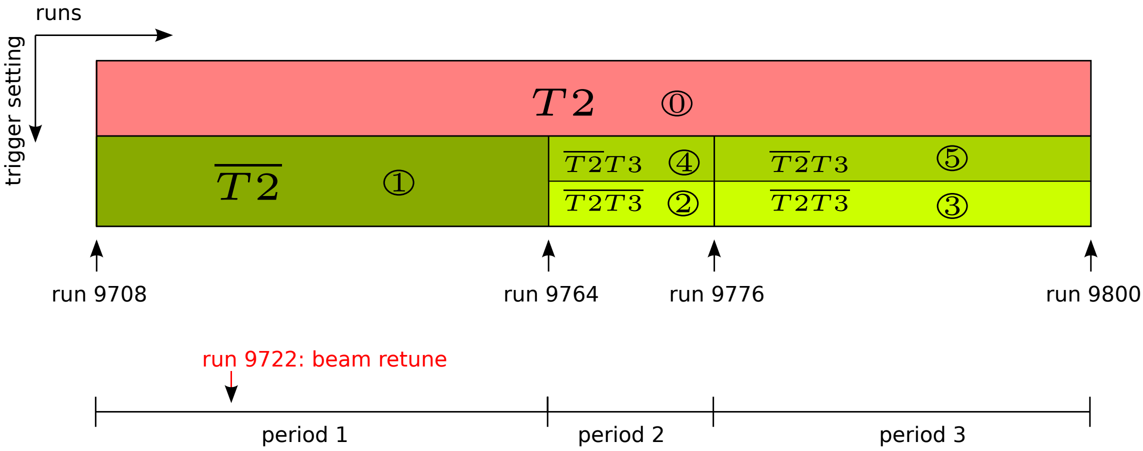

Figure 4.1.: Illustration of trigger sets and periods of 350 GeV/c data. Sets are denoted by circled numbers.

then bend away from the beam axis and do not hit the scintillator S4. However, this is not always true which leads to an inefficiency in S4 and eventually to a non-trivial bias in T2 data, as will be further discussed in Section 4.5.

T3 is also an interaction trigger and defined similarly to T2:

$$T3 = T1 \wedge \overline{S5} \tag{4.3}$$

In this case, the veto scintillator is S5, located behind the MTPC of the detector, as can be seen in Fig. 2.2. Due to its farther distance from the target (approximately 1561 cm [19]), S5 covers a much smaller solid angle ($\Omega \approx 1.3 \cdot 10^{-6}$ sr) than S4 ($\Omega \approx 2.3 \cdot 10^{-5}$ sr) which makes it more efficient for events with small production angles. The drawback of a small solid angle is the fact that the scintillator might not cover the beam entirely, if the beam suffers from a high divergence. Consequently, an additional bias occurs, in the sense that S5 does not trigger even though no interaction has taken place.

Table 4.2 and Table 4.1 show the number of recorded T1, T2 and T3 triggers for target-in and target-out runs after target upstream cuts (compare Section 4.2.1). During the run, all events with a T2 trigger have been recorded. However, only a fraction of the events with a T1 or T3 trigger have been recorded. This concept is called prescaling, typical values are between 100 and 250 for T2 and 20 for T3 [19]. T1 and T3 were mainly recorded for cross checks and as a fall back if T2 turns out be problematic. Indeed, during the course of this work, the trigger sets T1 and T3 have proven to be extremely useful for the correction of the trigger bias in T2, as explained in Section 4.5.

Since the ability to prescale has only been available since 2009, all published analyses of NA49 or NA61 have used T2 data only. Furthermore, T3 has only been used in the cosmic ray runs.

During the 350 GeV/c run, the definition of T3 has changed twice. Up to run 9764, the position of S5 was unknown. At run 9776, the position of S5 changed. In addition, at run 9722 a beam re-tune took place. Both, the position of S5 and the beam tune have an influence on the trigger probability of T3, thus it becomes necessary to divide the data set into different periods and calculate the trigger probabilities individually. Fig. 4.1 depicts the 350 GeV/c runs with the available trigger sets and the definition of periods and sets.

4.1.2. Simulated data

Table 4.3 shows the Monte Carlo sets that have been produced for $\pi^- + \mathrm{C}$ studies. The primary generator (EPOS or VENUS) provides production events (particles with momenta)

Table 4.1.: Selected trigger sets (after upstream target event cuts) for 350 GeV/c runs. Table shows the number of events N_{events}, the trigger probability P_{trig}, the binomial error of the trigger probability in per cent σ_P/P and the total number of tracks before quality cuts N_{tracks}.

Target-in						
Set	Period	Trigger	N_{events}	P_{trig}	σ_P/P [%]	N_{tracks}
⓪	1+2+3	$T2$	2870854	0.0277	0.693	28348860
①	1	$T1 \wedge \overline{T2}$	396604	0.972	0.027	36449
②	2	$T1 \wedge \overline{T2} \wedge \overline{T3}$	65850	0.901	0.12	1492
③	3	$T1 \wedge \overline{T2} \wedge \overline{T3}$	229879	0.915	0.060	4590
④	2	$T3 \wedge \overline{T2}$	72894	0.0710	1.3	56843
⑤	3	$T3 \wedge \overline{T2}$	187885	0.0576	0.80	184355
Target-out						
Set	Period	Trigger	N_{events}	P_{trig}	σ_P/P [%]	N_{tracks}
⓪	1+2+3	$T2$	81338	0.00252	4.1	353203
①	1	$T1 \wedge \overline{T2}$	94506	0.997	0.017	3779
②	2	$T1 \wedge \overline{T2} \wedge \overline{T3}$	12470	0.936	0.28	180
③	3	$T1 \wedge \overline{T2} \wedge \overline{T3}$	121494	0.948	0.065	1783
④	2	$T3 \wedge \overline{T2}$	10766	0.0615	3.4	3144
⑤	3	$T3 \wedge \overline{T2}$	70817	0.0492	1.2	26247

Table 4.2.: Selected trigger sets (after upstream target event cuts) for 158 GeV/c runs. Table shows the number of events N_{events}, the trigger probability P_{trig}, the binomial error of the trigger probability in per cent σ_P/P and the total number of tracks before quality cuts N_{tracks}.

Target-in				
Trigger	N_{events}	P_{trig}	σ_P/P [%]	N_{tracks}
$T1 \wedge \overline{T2} \wedge \overline{T3}$	405439	0.853	0.060	13314
$T2$	3489488	0.0331	0.78	24765352
$T3 \wedge \overline{T2}$	308384	0.114	0.40	68776
Target-out				
Trigger	N_{events}	P_{trig}	σ_P/P [%]	N_{tracks}
$T1 \wedge \overline{T2} \wedge \overline{T3}$	169467	0.886	0.082	4411
$T2$	121989	0.00398	3.6	282755
$T3 \wedge \overline{T2}$	101975	0.110	0.65	15368

Table 4.3.: Simulated data sets for $\pi^- + \mathrm{C}$. Number of events prior to any cut.

p [GeV/c]	Primary generator	Secondary generator	N [10^6]
158	VENUS 4.12	GCALOR	4.0
158	EPOS 1.99	GCALOR	4.0
350	VENUS 4.12	GCALOR	4.0
350	EPOS 1.99	GCALOR	4.0

to the GEANT3 [31] detector simulation. Hadronic decays are already perfromed by EPOS and VENUS In GEANT, the transportation of particles and their physical interaction is simulated. The secondary generator GCALOR [32] simulates inelastic interactions of the particles within the GEANT simulation. This also includes secondary interactions in the target.

4.2. Selection criteria and binning

In the first step, a series of cuts, which are described in the following, are applied on the data to select high quality events and tracks.

4.2.1. Event cuts: Target upstream / beam

The event cuts in this section are only applied on real data sets, as the beam detectors are not implemented in the simulations.

CEDAR cut

The size of the non-pion contributions can be estimated from the CEDAR scans in Fig. 2.4. For 350 GeV/c beam momentum, the contributions form antiprotons and K^- are negligible, therefore no CEDAR cut was applied for the runs with 350 GeV/c beam momentum. However, at $p_{\mathrm{beam}} = 158$ GeV/c, the beam is contaminated with approximately 4.2% K^- and approximately 1% antiprotons.

Since the CEDAR information is not included in the trigger definitions that were used during data taking, the particle identification has to be applied offline. In this analysis, the following CEDAR cut was applied:

- Two-fold coincidence for runs 9804 to 9890
- Six-fold coincidence for runs 9891 to 9900

A n-fold coincidence refers to the requirement that n out of the 8 PMTs of the CEDAR have to give a signal at the same time. This suppresses the noise of PMTs. The efficiency of the CEDAR is studied in [19].

WFA cut

The **W**ave **F**orm **A**nalyzer (WFA) is a component of the detector which collects and analyzes signals from the beam counter S1. It records and buffers the time information of every passing beam particle. In that way it is possible to obtain the time information of beam particles shortly before and after the main trigger. With this information, it is possible to judge whether there are more than one beam particles in the detector during the readout time of the TPCs. If there is an additional beam particle shortly before or after the main trigger, it can lead to the following effects:

- Pile up (multiple primary interactions in the target)
- Delta electrons
- Primary interaction after hit in a trigger scintillators S4 or S5

In 2009, the beam intensity of negatively charged hadrons in $\pi^- + \mathrm{C}$ runs was not larger than 40 kHz (see appendix Fig. C.2). Still, to exclude a possible bias from the effects listed above, a WFA cut of 2 μs is applied. At a drift velocity of 1.5 cm/μs, this corresponds to a vertical displacement of 3 cm which separates such tracks well from the main vertex. Events are removed if there is another beam particle within a time window of

$$|\Delta t| \leq 2000\,\mathrm{ns} \tag{4.4}$$

prior or after the main trigger.

The resolution of the WFA is approximately 100 ns. The possible bias from this limitation is studied in Section C.

BPD cut

The BPD measures the beam divergence and beam position. The extrapolation of the beam to the target plane constrains the position of the main vertex (here the BPD vertex, z-position fixed at center of target). The BPD information is also used to constrain the so called fitted main vertex (z-position is a free parameter as well). In this analysis, the BPD vertex is taken as the main vertex.

Still, a BPD cut is applied to select events with a high quality of the BPD information and to ensure that no interaction has taken place before the last BPD plane. As described in Section 2.1, the BPD comprises a set of 3 detector planes (BPD1, BPD2, BPD3), each with independent x and y measurement [33]. The BPD cut used in this work removes events if

- in at least one plane no valid cluster was found,
- the information from BPD3y was invalid,
- the information from BPD3x was invalid, or
- the BPD fit of the beam failed.

4.2.2. Event cuts: Target downstream

Furthermore, event cuts are applied that depend on measurements downstream of the target. Those cuts can be applied on Monte Carlo simulations too.

Subsets of trigger settings

The division into subsets of trigger settings is only done for real data. In Monte Carlo, the sets are kept unchanged, containing all production events. The data sets are divided into the following trigger sets:

- $T2$
- $\overline{T2} \wedge T3$
- $\overline{T2} \wedge \overline{T3} \wedge T1$

Those sets are disjoint and since $T2 \subset T1$ and $T3 \subset T1$, their union equals T1 (which is important for the trigger bias correction in Section 4.5):

$$T1 = T2 \cup (\overline{T2} \wedge T3) \cup (\overline{T2} \wedge \overline{T3} \wedge T1) \tag{4.5}$$

Existence and type of main vertex

Since the analysis of this work is interested in main vertex tracks only, it is a necessity to require the existence of a reconstructed main vertex in every event. Furthermore, the type of main vertex, namely BPD vertex or fitted vertex is relevant. These cuts ought to be applied on real data and Monte Carlo simulations. In this analysis events are removed if

- there is no main vertex present or
- the type of the main vertex is not BPD vertex.

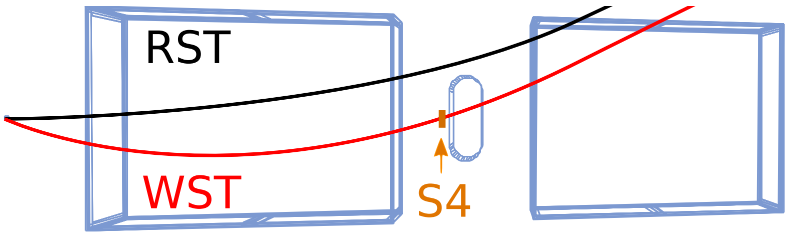

Figure 4.2.: Illustration of direct hits of S4 by low energetic wrong side tracks. The drawing shows VTPC1 (left), GTPC (center) and VTPC2 (right). Right side tracks (RST) are defined by the fact that they are bend away from the beam axis. Wrong side tracks (WST) are bend towards the beam axis.

4.2.3. Track cuts

First of all, a technical cut on the "NA49 iflag" of the vertex track is applied. It removes vertex tracks that are leftovers of failed fit attempts of the reconstruction. In this work, vertex tracks are removed if

$$\text{iflag} \neq 0\,. \tag{4.6}$$

Acceptance cut

The acceptance cut rejects tracks that are not in a momentum bin of the defined acceptance. The acceptance is defined in ϕ, p and p_T and described in the following. The acceptance definition can be divided in two parts, namely

- the removal of direct hits in S4 and
- the removal of bins with a low selection efficiency.

Removal of direct hits in S4

In production events, the scintillator S4 is mainly hit by very high energetic tracks with a very low production angle. Apart from that, there is a second class of track topologies that hits S4, as depicted in Fig. 4.2. Those are necessarily wrong side tracks (WST, see Fig. 4.2 for definition). Since the T2 trigger is vetoed by S4, events with a track that hits S4 are not in the T2 data set. Thus, a *hole* in the phase space is apparent in the T2 data. This hole is a small-scale feature in the phase space and cannot be efficiently corrected for in the T2 bias correction applied later in Section 4.5. Therefore it is necessary to remove the affected bins from the acceptance.

There are two ways to remove the affected bins from the acceptance:

1. Use of full Monte Carlo simulation to look at tracks that have a hit in the simulated S4. Reject momentum bins in which more than 5% of the tracks hit S4 and at least 10 tracks have been simulated.
2. Scan the phase space by tracking charged particles through the magnetic field to the z-position of S4. Remove bins of phase space if the tracks are close to the center of S4 in x and y-direction. Conservative values ($|\Delta x| < 2.8\,\text{cm}$ and $|\Delta y| < 2.0\,\text{cm}$) have been found by comparing the two methods.

In both cases, the loss of statistics due to this cut is very small. In this analysis, the second option was chosen.

Removal of bins with low selection efficiency

The detector naturally comes along with a limited geometrical acceptance. The most trivial factor is the azimuthal angle ϕ, since the physics of $\pi^- + \text{C}$ interactions is symmetrical with respect to ϕ. The geometry of the detector also limits the phase space in p and p_T, which leads to a finely structured three dimensional acceptance.

Table 4.4.: Binning for acceptance definition.

Quantity	Unit	N_{bins}	Lower edge	Upper edge
ϕ	deg	50	-180	180
p_T	GeV/c	50	0.001	10
p	GeV/c	50	0.1	1000

In this analysis, the acceptance of the detector is studied and corrected with Monte Carlo simulations. The acceptance is usually either approximately one or zero. To obtain a correction as accurate as possible, it has proven beneficial to exclude transition regions to become independent of details of boundaries of TPCs, where Monte Carlo and data might disagree noticeable. Such a transition region is characterized by rising or falling acceptance in ϕ.

The idea of the acceptance definition in this work is to look at the *selection efficiency*. It is defined in every (ϕ, p, p_T)-bin as

$$\varepsilon_{\text{sel}} = \frac{N_{\text{selected}}}{N_{\text{sim}}} \tag{4.7}$$

with the number of simulated tracks N_{sim} and the number of selected tracks N_{selected}. More precisely, N_{sim} are tracks that do not decay or interact within or near by the TPCs or are pions with $p > 1$ GeV/c, see appendix Section F for technical details. N_{selected} is the number of simulated tracks that are matched to a reconstructed track that passes the cluster cuts

- $N_{\text{VTPC1+VTPC2}} \geq 12$ or $N_{\text{GTPC}} \geq 6$ and
- $N_{\text{total}} \geq 30$.

$N_{\text{VTPC1+VTPC2}}$, N_{GTPC}, and N_{total} are the number of clusters in the VTPCs, the GTPC and all TPCs respectively. The effect of the restriction of the number of clusters is visible in Fig. 3.6.

Since N_{sim} and N_{selected} are counts of simulated tracks, the momentum of the simulated track is taken to determine the bin in both cases. The matching is based on the maximum common points of the simulated track and the reconstructed track. It is considered successful if

- a valid track could be found and
- the number of common points of the simulated track and the reconstructed track is at least 10.

The selection efficiency is a criterion of the quality of the bins in phase space. Low values of ε_{sel} are expected if

- the spacial coverage of the TPCs is limited or zero (low number of clusters or no track reconstructed),
- the quality of reconstruction is poor (low number of clusters), or
- the bin is in or close to a transition region.

The binning for the acceptance definition is shown in Table 4.4. It is equidistant in ϕ, $\log p_T$, and $\log p$.

In the following, N_{sim} in Eq. 4.7 is also called N_{min} because it statistically limits the feasibility of the procedure. A bin is excluded from the acceptance if

- $N_{\text{min}} < 10$,
- $\varepsilon_{\text{sel}} < 0.9$,
- one of the two points above holds for a bin adjacent in ϕ, or

Table 4.5.: Binning used for the analysis of all data sets. Unoccupied bins are dropped in individual cases.

Quantity	Unit	N_{bins}	Lower edge	Upper edge
p_T	GeV/c	4	0	0.0832
p_T	GeV/c	27	0.0832	10
p	GeV/c	50	0.1	1000

- it has been marked bad due to hits in S4

The acceptance map used in this work can be seen in Fig. 4.3, together with different choices of the parameters N_{min} and ε_{sel}.

Number of clusters cut

As discussed earlier, a reconstructed track is fitted on the basis of a series of clusters. The more clusters are taken for the fit, the more accurate the fit of momentum becomes. Thus, tracks with a large number of clusters are preferable. To ensure a high quality of the fit, i.e. a good momentum resolution, reconstructed tracks are removed if they do not comply with the following requirements:

- $N_{\text{VTPC1+VTPC2}} \geq 12$ or $N_{\text{GTPC}} \geq 6$
- $N_{\text{total}} \geq 25$

$N_{\text{VTPC1+VTPC2}}$ is the sum of the number of clusters in VTPC1 and VTPC2. N_{GTPC} is the number of clusters in the GTPC. N_{total} is the total number of clusters, summed over all TPCs. The first condition ensures that there are clusters found in the magnetic field which is important for tracks that have most clusters in the MTPC, because it then provides a large lever arm for the fit of momentum and consequently a good momentum resolution.

Impact parameter cut

During reconstruction, tracks that are associated to the main vertex are refitted with the vertex constrain and become a so called vertex track, compare Section 2.3.

The impact parameter b is defined as the transverse distance of the extrapolated track at the vertex plane (z-position of the main vertex) to the main vertex. It is a measure of the quality of track reconstruction. Furthermore, large b can hint to wrongly associated tracks or to tracks that come from secondary interactions in the target or from decay.

The impact parameter with respect to the x-coordinate and y-coordinate are labeled b_x and b_y respectively. In this analysis, tracks are removed if

- $b_x \geq 4$ cm or
- $b_y \geq 4$ cm.

4.2.4. Binning

As already mentioned, the kinematic variables of interest are p and p_T. The bins used in this analysis are almost everywhere equally spaced in $\log p$, and $\log p_T$. Exceptions are bins with $p_T \leq 0.0832$ GeV/c, where pairs of two bins are merged and $p_T = 0$ is included, see Table 4.5. The lower and upper edges of each bin are visible in the table of the final results (Table H.4). During the analysis, a bin is removed if the relative statistical error from data (after target-out subtraction) or from Monte Carlo is larger than 40%.

4.3. Target-out subtraction and normalization to N_{beam}

As a first step of normalization, all trigger sets are normalized to the number of beam triggers N_{beam}, even though N_{beam} is not directly measured but has to be calculated from the trigger probabilities.

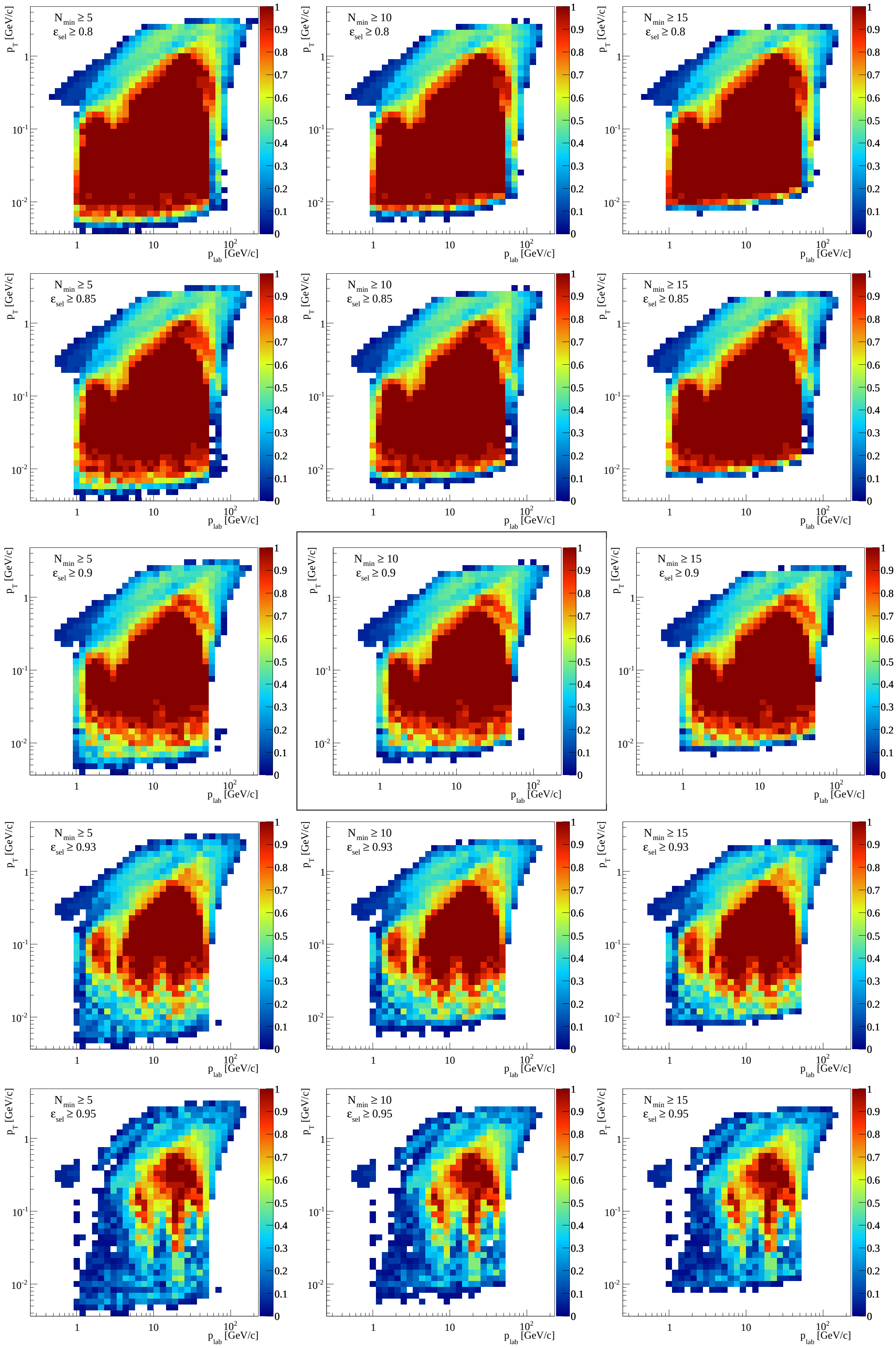

Figure 4.3.: Variation of N_{min} and ε_{sel} in the acceptance map for negative tracks. The z-axis shows the fraction of accepted to rejected bins in ϕ. In this analysis, $N_{\rm min} \geq 10$ and $\varepsilon_{\rm sel} < 0.9$ (plot in the center) is used.

Calculation of trigger probabilities

The trigger probability P relates N_{beam} to the number of triggered events. For the case of $T2$, it holds

$$P(T2) = \frac{N_{T2}}{N_{\text{beam}}} \tag{4.8}$$

The same is true for all other trigger sets, such as $T3 \wedge \overline{T2}$, $T1 \wedge \overline{T2}$, and $T1 \wedge \overline{T2} \wedge \overline{T3}$.

Given the trigger probability, it is possible to normalize the data sets to the number of beam triggers. For example, in the case of T2 this reads as:

$$\left[\frac{\Delta n}{N_{\text{beam}}}\right]_{\text{T2 contribution}} = \frac{\Delta n}{N_{T2}} P(T2) \tag{4.9}$$

Δn is the number of tracks in a particular (p, p_T) bin.

Target-out subtraction

Once a data sets is normalized to the number of beam triggers, the target-out subtraction can be done in the following way:

$$\left[\frac{\Delta n}{N_{\text{beam}}}\right]_{\text{IN/OUT corrected}} = \left[\frac{\Delta n}{N_{\text{beam}}}\right]_{\text{IN}} - \left[\frac{\Delta n}{N_{\text{beam}}}\right]_{\text{OUT}} \tag{4.10}$$

After normalization to N_{beam}, it is also possible to add different trigger settings to obtain an unbiased data set. This is done in Section 4.5.

4.4. Monte Carlo correction

In the Monte Carlo simulation, realistic events are generated and tracked through the detector with a complete list of physical processes being enabled. Also the detector response is precisely simulated. In such a way it is possible to obtain correction (or reweighting) factors for track multiplicities that correct for various effects such as decays, secondary interactions and also geometrical acceptance. A breakdown of the correction factor is discussed in the following subsection.

Since the simulation can not cover all effects that occur in a real experiment, it is reasonable to minimize the use of Monte Carlo simulations. The bias from simulations is the smallest if the properties are examined on small intervals, e.g. track multiplicities in p, p_T and ϕ. Corrections obtained for global variables that depend on event topology, such as event multiplicity or the actual spectra are less reliable.

In this work, Monte Carlo corrections are only taken for track multiplicities and are obtained bin-wise. The correction factor is defined as

$$c = \frac{\Delta n_{\text{gen}}}{\Delta n_{\text{rec}}} \tag{4.11}$$

with Δn_{gen} the generated number and Δn_{rec} the reconstructed number of tracks in a particular bin. The correction factor c can be found in Fig. 4.4 where a breakdown into the purely geometrical part (acceptance) and the nontrivial other factors is shown.

The correction for the final results is done with averaged correction factors from VENUS and EPOS.

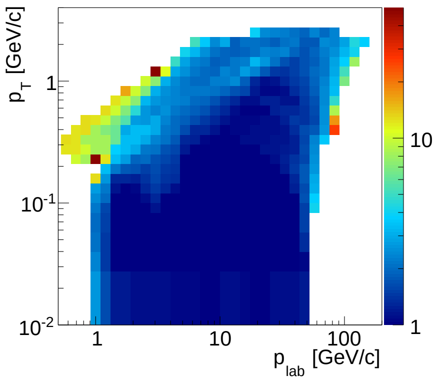

(a) h^-, acceptance correction

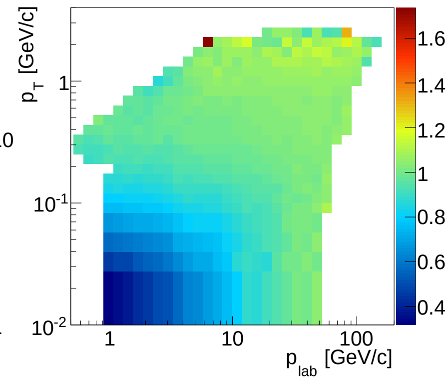

(b) h^-, other MC corrections

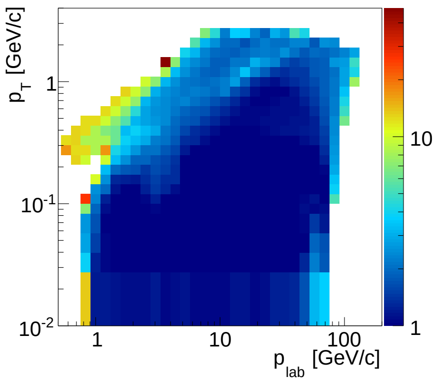

(c) h^+, acceptance correction

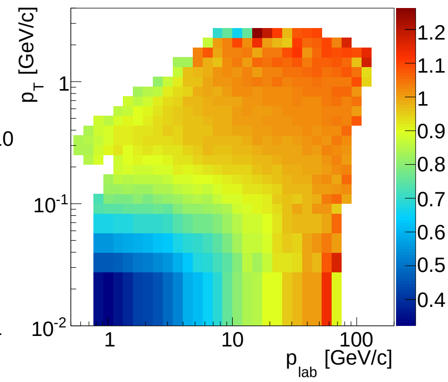

(d) h^+, other MC corrections

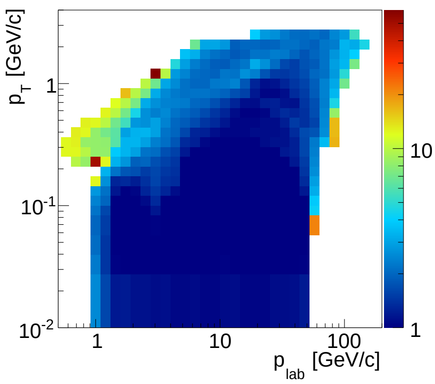

(e) h^-, acceptance correction

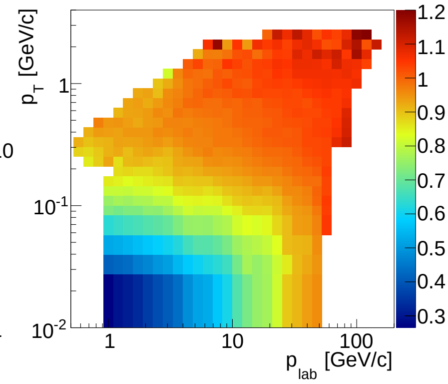

(f) h^-, other MC corrections

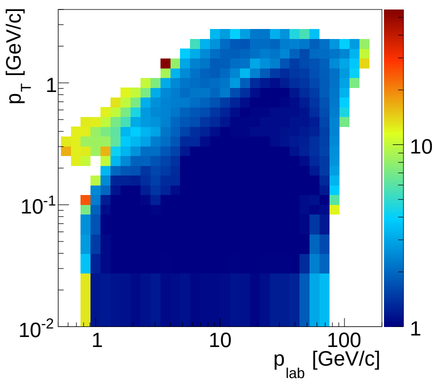

(g) h^+, acceptance correction

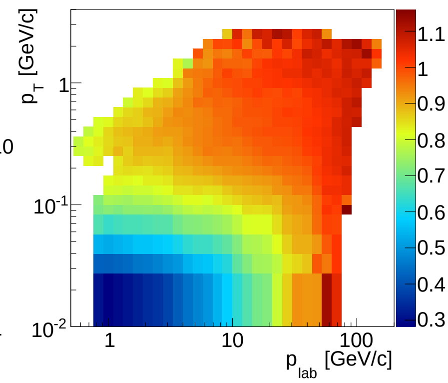

(h) h^+, other MC corrections

Figure 4.4.: Correction factors obtained from EPOS Monte Carlo simulations for 158 GeV/c (a – d) and 350 GeV/c (e – h).

4.4.1. Breakdown of correction factors

To further understand the various origins of the correction factors obtained by Monte Carlo simulations, it is instructive to study their individual components (breakdown). The following (incomplete) list states various contributions to the correction factor:

- Acceptance correction (purely geometrical)
- Track cut efficiency
- Track reconstruction efficiency
- Decay of charged and neutral hadrons (track gain or loss, kinks)
- Secondary interactions in target and in the detector volume
- $e^{\pm}$ contamination (conversion of γ in the target from π^0 decay)

Hadronic decay is not included in this method. The Monte Carlo simulations EPOS and VENUS already produce an output of events where hadronic decay has taken place.

Fig. 4.5 shows the breakdown of the non-geometrical part of the correction factor for negatively charged hadrons for 350 GeV/c beam momentum obtained from EPOS Monte Carlo simulations. The correction factors for positively charged particles as well as those for 158 GeV/c can be found in Section G. The breakdown is calculated as follows. First, the overall correction factor from non-geometrical contributions, in the following called c_{total} has been broken down into three contributions:

The following list depicts the example for negative tracks. If not otherwise specified, a successful match of simulated and reconstructed track is required and the reconstructed momentum is taken for the bin determination.

- c_{gain}: This contribution corrects for a gain of tracks in the reconstruction. Possible reasons are decay and secondary interactions. c_{gain} is always smaller than one.

$$c_{\text{gain}} = \frac{\Delta n_{\text{rec},h^-,\text{from main vertex}}}{\Delta n_{\text{rec},h^-}} \tag{4.12}$$

- c_{loss}: This contribution corrects for a loss of tracks. Possible reasons are decay, secondary interactions, reconstruction inefficiency, and migration out of the bin. c_{loss} is mostly greater than one.

$$c_{\text{loss}} = \frac{\Delta n_{\text{gen},h^-,\text{from main vertex}}{}^{*\,\dagger}}{\Delta n_{\text{rec},h^-,\text{from main vertex}}} \tag{4.13}$$

- $c_{e/\mu\text{ contamination}}$: This contribution corrects for the lepton contamination. Most of the electrons that are reconstructed as main vertex tracks come from the conversion of γ's in the target. The γ's in turn stem from the decay of π^0's. Muons mostly come from the decay of $K^{\pm}$ and $\pi^{\pm}$. The muon contribution is much lower than the electron contribution, however since they are not primary particles their momentum is not equal to the one of the hadron they stem from which is an effect that has to be corrected for. $c_{e/\mu\text{ contamination}}$ is always smaller than one.

$$c_{e/\mu\text{ contamination}} = \frac{\Delta n_{\text{rec},h^-}}{\Delta n_{\text{rec,all neg. tracks}^\dagger}} \tag{4.14}$$

*: simulated momentum taken for bin determination

†: a successful match is not required

Note that h^- stands for hadrons (excluding other negatively charged tracks). This breakdown has been chosen because the original correction factor c_{total} factorizes into the correction factors c_{gain}, c_{loss}, and $c_{e/\mu\text{ contamination}}$, compare Eq. 4.15 and Eq. 4.11.

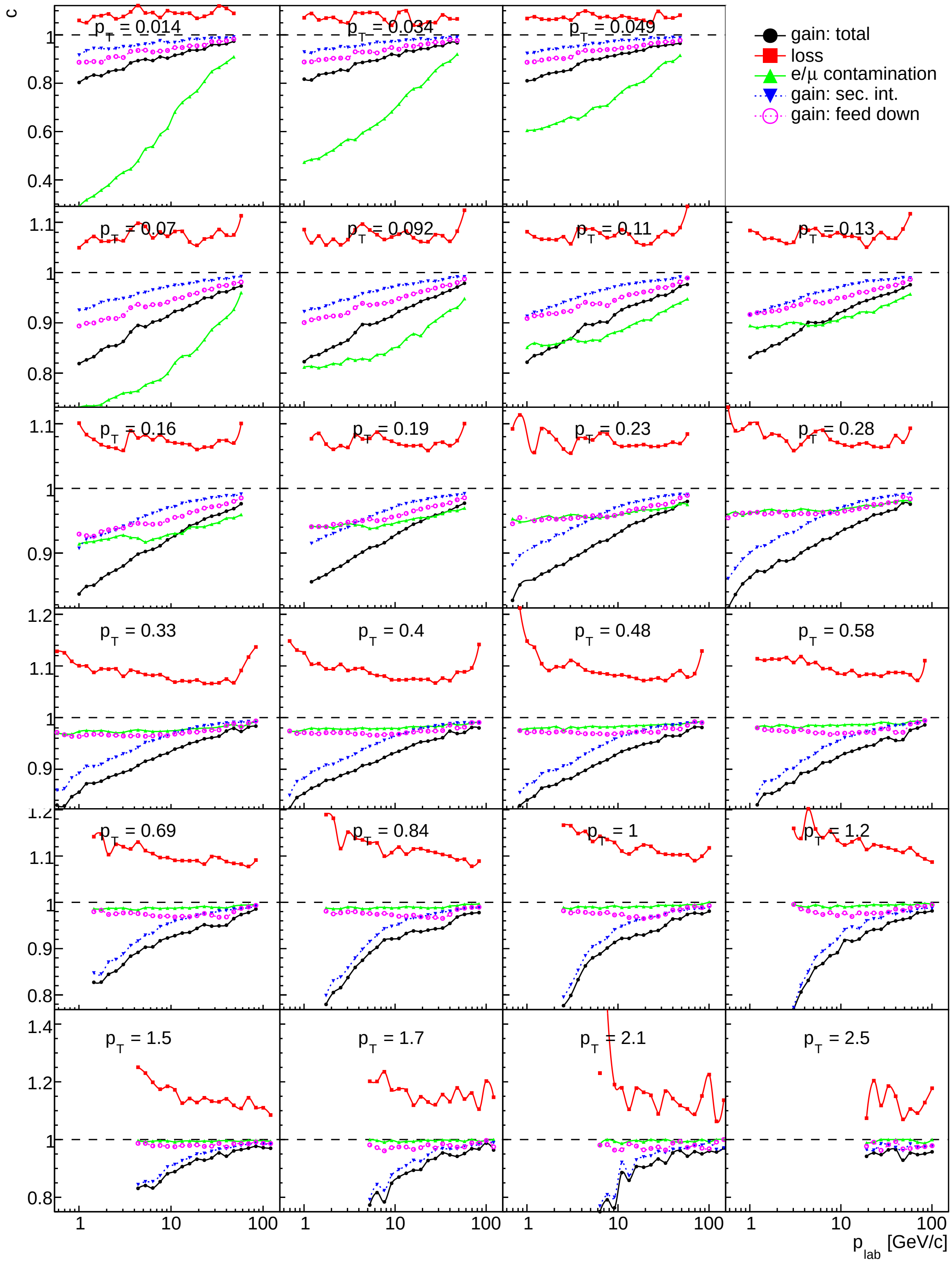

Figure 4.5.: Breakdown of the correction factor for negatively charged hadrons obtained from EPOS Monte Carlo simulations for 350 GeV/c. Transverse momentum p_T is given in GeV/c.

$$\begin{aligned} c_{\text{total}} &= c_{\text{gain}} \cdot c_{\text{loss}} \cdot c_{\text{e}/\mu \text{ contamination}} \\ &= \frac{\Delta n_{\text{rec},h^-,\text{from main vertex}}}{\Delta n_{\text{rec},h^-}} \cdot \frac{\Delta n_{\text{gen},h^-,\text{from main vertex}}}{\Delta n_{\text{rec},h^-,\text{from main vertex}}} \cdot \frac{\Delta n_{\text{rec},h^-}}{\Delta n_{\text{rec,all neg. tracks}}} \\ &= \frac{\Delta n_{\text{gen},h^-,\text{from main vertex}}}{\Delta n_{\text{rec,all neg. tracks}}} \end{aligned} \tag{4.15}$$

In a second step, a more detailed breakdown of c_{gain} into a contribution from feed down (decay) and a contribution from secondary interaction has been performed:

$$c_{\text{gain: sec. interaction}} = \frac{\Delta n_{\text{rec},h^-,\text{not from sec. int.}}}{\Delta n_{\text{rec},h^-}} \tag{4.16}$$

$$c_{\text{gain: feed down}} = \frac{\Delta n_{\text{rec},h^-,\text{not from decay}}}{\Delta n_{\text{rec},h^-}} \tag{4.17}$$

Both quantities are always greater than one. Unfortunately, c_{gain} does not factorize trivially into $c_{\text{gain: sec. interaction}}$ and $c_{\text{gain: feed down}}$. The calculation (Eq. 4.18) shows that an additional factor $c_{\text{factoring compensator}}$ arises, which can be larger than one.

$$\begin{aligned} c_{\text{gain}} &= \frac{\Delta n_{\text{rec},h^-,\text{from main vertex}}}{\Delta n_{\text{rec},h^-}} \\ &= \frac{\Delta n_{\text{rec},h^-,\text{not from sec. int.}}}{\Delta n_{\text{rec},h^-}} \cdot \frac{\Delta n_{\text{rec},h^-,\text{not from decay}}}{\Delta n_{\text{rec},h^-}} \\ &\quad \cdot \frac{\Delta n_{\text{rec},h^-} \cdot \Delta n_{\text{rec},h^-,\text{from main vertex}}}{\Delta n_{\text{rec},h^-,\text{not from sec. int.}} \cdot \Delta n_{\text{rec},h^-,\text{not from decay}}} \\ &= c_{\text{gain: sec. interaction}} \cdot c_{\text{gain: feed down}} \cdot c_{\text{factoring compensator}} \end{aligned} \tag{4.18}$$

Note: "not from sec. int." means that the track must not come from a secondary interaction but may come from the main vertex, from a decay or something else not further specified.

From Fig. 4.5 it is possible to judge what contributions to the correction factor are dominating at certain momenta.

For low p_T bins up to $p_T \approx 0.11$ GeV/c, the lepton contamination is the largest contribution to the correction factor. For $p_T = 0.014$ GeV/c, the smallest value of c is 0.4, which means only 40% of the observed tracks are hadrons. The correction is the greatest for low momenta and goes down with p. For p_T bins from $p_T \approx 0.69$ GeV/c, the lepton contribution is negligible.

The correction due to gain of tracks (black line) is divided into gain from secondary interactions (blue dashed line) and gain from feed down (magenta dashed line). Generally it can be seen that the correction of gain becomes smaller with increasing momentum. For p_T bins up to $p_T \approx 0.19$ GeV/c, both contributions to the gain are of a similar order of magnitude. The shape of $c_{\text{gain: sec. interaction}}$ comes from the fact that secondary particles are created by primary particles which necessarily have an energy smaller than the beam momentum. Thus the creation of low energetic secondaries is much more probably than the creation of high energetic particles.

The correction for this gain is dominating for p_T bins from $p_T \approx 0.28$ GeV/c and goes up further for increasing p_T. This can be explained by the fact that the transverse momentum from the primary particle and the secondary particle add up, thus spreading the secondary particles more into the regions of high p_T. High p_T bins are less densely populated by primary particles but the contribution from secondary particles is only marginally lower thus making the relative effect of secondaries large.

The limited statistics of Monte Carlo introduces wiggles for high p_T bins, especially visible in the contribution from loss in $p_T \geq 1.7$ GeV/c. Another rise of the contribution from loss can also be seen for high and low p in bins around $p_T = 0.48$ GeV/c. This can be explain by the fact that this contribution also contains negative migration effects which can enhance at the edge of the acceptance.

4.5. Trigger bias correction

As mentioned in Section 4.1.1, most of the recorded triggers are T2, which is a biased trigger set because the veto scintillator S4 necessarily removes events of certain event topologies. From the point of statistics, T2 data is much larger compared to the other trigger sets. For this reason, the results of this work are directly obtained from the T2 data set but a correction for the T2 bias is applied. The statistical error on the number of tracks in the individual bins then comes only from the T2 data set while additional uncertainties from the T2 bias correction are treated as systematics.

In the following, the method of T2 bias correction used in this work is explained. Alternative methods of trigger bias correction are discussed in the appendix in Section A.

4.5.1. Unbiased trigger set

T1, the beam trigger, is an unbiased (or zero biased) trigger set. Since the interaction probability is of the order of 3%, the T1 set contains mostly events without interaction thus being statistically insufficient for a full analysis.

It is, however, possible to combine the information of all recorded trigger sets T1, T2, and T3 to obtain an unbiased data set with the maximum information (thus the minimal statistical uncertainty).

After the normalization to N_{beam} (see Section 4.3) of all data sets, especially $T2$, $T3 \wedge \overline{T2}$, and $T1 \wedge \overline{T2} \wedge \overline{T3}$, the following equation holds due to Eq. 4.5:

$$\left[\frac{\Delta n}{N_{\text{beam}}}\right]_{\text{T1 (unbiased)}} = \left[\frac{\Delta n}{N_{\text{beam}}}\right]_{T2} + \left[\frac{\Delta n}{N_{\text{beam}}}\right]_{T3\wedge\overline{T2}} + \left[\frac{\Delta n}{N_{\text{beam}}}\right]_{T1\wedge\overline{T2}\wedge\overline{T3}} \tag{4.19}$$

The terms in square brackets denote the contributions to the number of tracks normalized to N_{beam} from individual trigger sets in a particular (p, p_T) bin. In other words, the terms in square brackets are the contributions to the mean multiplicity from individual trigger sets. Thus, the sum of the contributions equals the total, unbiased value for the mean multiplicity (term on the left hand side) in a particular (p, p_T) bin.

Going back to the definition of the normalization to N_{beam} (Section 4.3), Eq. 4.19 can be written as:

$$\begin{aligned}\left[\frac{\Delta n}{N_{\text{beam}}}\right]_{\text{T1 (unbiased)}} &= \underbrace{\frac{\Delta n_{T2}}{N_{T2}}P(T2)}_{\alpha} + \underbrace{\frac{\Delta n_{T3\wedge\overline{T2}}}{N_{T3\wedge\overline{T2}}}P(T3\wedge\overline{T2})}_{\beta} \\ &+ \underbrace{\frac{\Delta n_{T1\wedge\overline{T2}\wedge\overline{T3}}}{N_{T1\wedge\overline{T2}\wedge\overline{T3}}}P(T1\wedge\overline{T2}\wedge\overline{T3})}_{\gamma}\end{aligned} \tag{4.20}$$

Table 4.6.: Summary of contributions and their uncertainties to the unbiased data set. The corresponding numbers can be found in Table 4.2 and Table 4.1.

Term in Eq. 4.20	Trigger sample	Statistical error	Contribution to Eq. 4.20
α	T2	small	large
β	T3	large	small
γ	T1	very large	very small

Δn_i stands for the number of tracks of an individual trigger set i in a particular (p, p_T) bin. N_i is the number of events of an individual trigger set. $P(i)$ is the trigger probability of an individual trigger set. Values for N_i and $P(i)$ can be found in Table 4.2 and Table 4.1. The magnitude of the contributions and uncertainties of the terms α, β and γ are summarized in Table 4.6.

Note, the numbers Δn and N_{beam} on the left hand side of Eq. 4.20 are not individually known but their fraction is given by the very equation.

The unbiased result (left hand side of Eq. 4.20) is obtained for target-in and target-out data. The target-out subtraction (as shown in Section 4.3) is then performed on the unbiased terms.

Additional considerations for the 350 GeV/c runs

During the run with 350 GeV/c beam momentum, the definition of T3 has and the position of S5 has changed. This means that the 350 GeV/c run has to be divided into three periods (see Fig. 4.1) with different trigger definitions and a total number of six trigger sets for target-in and target-out respectively. Each set has a different trigger probability and has to be normalized to N_{beam}. Due to the uncertainties in the trigger probability it is not trivial to merge all available trigger sets to an unbiased set. In fact, a procedure that simultaneously minimizes the total uncertainty of the result has to performed to obtain the weights which are used to merge the sets. Since the statistics of $\overline{T2}$ trigger sets was low in period 2 (see Table 4.1) and T3 was not used in period 1, the periods 1 and 2 have not been used in this work. The calculation according to Eq. 4.19 has been done with set 0, 3, and 5.

4.5.2. Obtaining T2 correction factors

As described qualitatively in Table 4.6, the statistical limitations of the T1 and T3 trigger sets lead to rather large statistical uncertainties in the unbiased data set. Thus it is not directly used for the results. Instead, the unbiased trigger set is used to obtain a correction factor for the T2 data set that corrects for the trigger bias. This factor f relates the mean multiplicity of T2 data to the unbiased mean multiplicity in a particular (p, p_T) bin:

$$f = \frac{\Delta n_{\text{T2}}}{\Delta n_{\text{unbiased}}} \tag{4.21}$$

Δn_{T2} and $\Delta n_{\text{unbiased}}$ are the mean multiplicities in a particular bin of the T2 data set and the unbiased set respectively.

The fraction f is calculated and then fitted with an empirical function in p and p_T:

$$f(p, p_T) = c_0 + c_1 p_T + [c_2 + c_3 p_T] \log p \tag{4.22}$$

$f(p, p_T)$ is motivated by two aspects. Firstly, the trigger bias is not expected to have any small scale features since the direct T2 hits have been removed, see Section 4.2.3. Secondly, the trigger bias is expected to go to zero for large momenta and generally increase for falling p. This is due to the fact that tracks that hit S4 ought to have a very high

Table 4.7.: Goodness of fit of T2 bias correction for positively and negatively charged tracks in 158 GeV/c and 350 GeV/c beam momentum.

p [GeV/c]	Tracks	NDF	χ^2	χ^2_{red}
158	h^-	499	381.6	0.77
	h^+	528	348.5	0.66
350	h^-	498	464.5	0.93
	h^+	530	464.2	0.88

momentum (otherwise they would have been bend away in the magnetic field) which makes it kinematically impossible that another track with very high momentum has been created. The linearity in p_T and the logarithmic behavior in p are found empirically. The goodness of the fit is validated via its χ^2. Table 4.7 shows the number of degrees of freedom (NDF), χ^2 and the reduced version $\chi^2_{\text{red}} = \chi^2/\text{NDF}$. The value of χ^2 depends on the estimate of the uncertainty of the data points. In this case, the uncertainty is the statistical uncertainty only. The fit parameters can be found in the appendix in Table G.3.

The statistical error of the fit of $f(p, p_T)$ can be calculated form its covariance matrix and is treated as a systematic effect, as discussed in the next section.

Fig. 4.6 shows f as calculated from Eq. 4.21 and the values obtained from the fitted function $f(p, p_T)$. As can be seen, the fit smooths out the statistical fluctuations in f thus making the correction less dependent on the statistical limitations of the unbiased trigger set.

Once the T2 correction factor f (taken from the fitted function $f(p, p_T)$) and the Monte Carlo correction c are calculated for every (p, p_T) bin, both corrections are applied on the data:

$$\Delta n_{\text{corrected, unbiased}} = \Delta n_{\text{uncorrected, T2}} \frac{c}{f} \tag{4.23}$$

4.6. Normalization

Thus far, the track multiplicity of a particular bin is normalized to N_{beam}. In this section it is shown how to calculate the inclusive cross section and the mean multiplicity in production events.

4.6.1. Inclusive cross section

The relationship between the probability of a production event and the production cross section is given by

$$P_{\text{prod}} = 1 - \mathrm{e}^{-C \cdot \sigma_{\text{prod}}} \tag{4.24}$$

where $C \approx 0.18446$ b^{-1} [19] is the target constant. The target constant only depends on parameters of the target, such as its length and composition but not on the projectile.

The relationship between the track multiplicity normalized to production events and the inclusive cross section is given by

$$\frac{\Delta n}{N_{\text{prod}} \Delta p_{\text{lab}} \Delta p_T} = \frac{1}{\sigma_{\text{prod}}} \cdot \frac{\Delta\sigma}{\Delta p_{\text{lab}} \Delta p_T} \ , \tag{4.25}$$

compare Equation (2) in [34].

The interaction probability of a particular type relates the number of events with an interaction of that particular type to the number of beam particles:

$$N_{\text{beam}} \cdot P_{\text{int}} = N_{\text{int}} \tag{4.26}$$

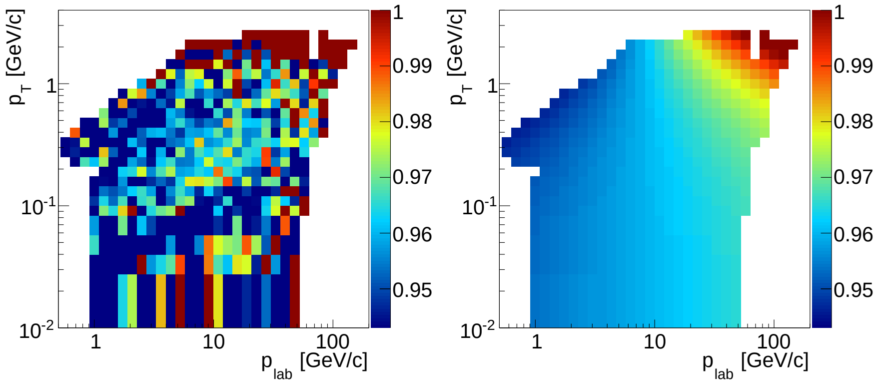

(a) h^-, 158 GeV/c, raw

(b) h^-, 158 GeV/c, fitted

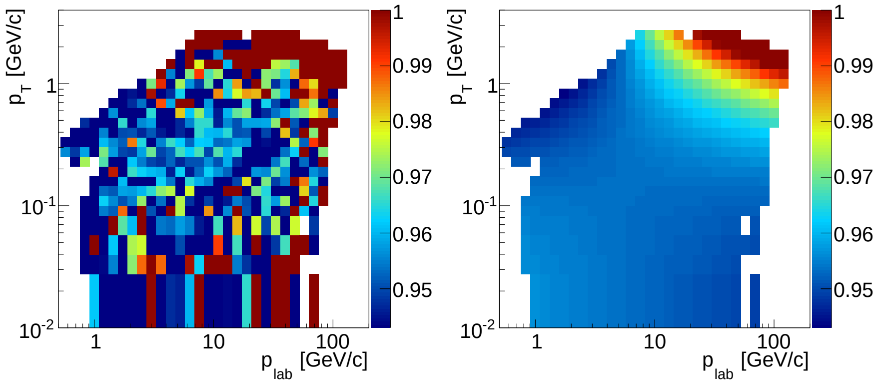

(c) h^+, 158 GeV/c, raw

(d) h^+, 158 GeV/c, fitted

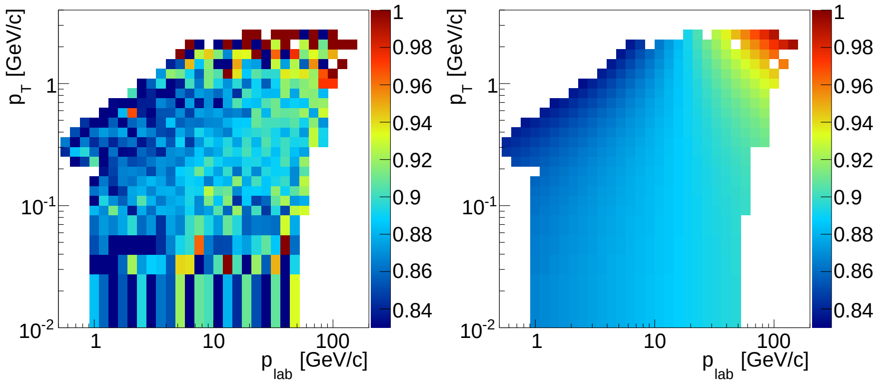

(e) h^-, 350 GeV/c, raw

(f) h^-, 350 GeV/c, fitted

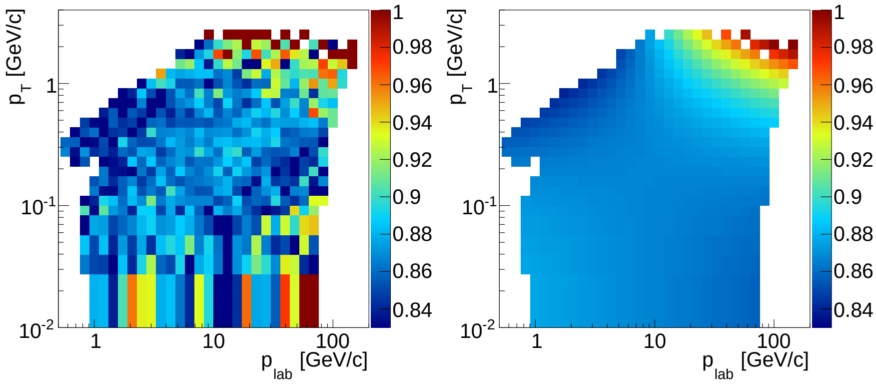

(g) h^+, 350 GeV/c, raw

(h) h^+, 350 GeV/c, fitted

Figure 4.6.: T2 correction factors for negatively and positively charged hadrons at 158 GeV/c and 350 GeV/c beam momentum. Left panels: f prior to fit. Right panels: f after fit.

With Eq. 4.24, Eq. 4.25, and Eq. 4.26, track multiplicities can be written as cross sections:

$$\frac{\Delta\sigma}{\Delta p_{\text{lab}}\Delta p_T} = \frac{\Delta n}{N_{\text{beam}}\Delta p_{\text{lab}}\Delta p_T} \cdot \frac{\sigma_{\text{prod}}}{1 - \mathrm{e}^{-C\sigma_{\text{prod}}}} \tag{4.27}$$

The expression can be simplified by defining an effective target constants for each beam momentum:

$$C_{\text{eff},p_{\text{beam}}} = \frac{1 - \mathrm{e}^{-C\sigma_{\text{prod}}}}{\sigma_{\text{prod}}} \tag{4.28}$$

The denominator of the second term in 4.27 can be expanded via

$$1 - \mathrm{e}^{-C\sigma_{\text{prod}}} = C\sigma_{\text{prod}} - \frac{(C\sigma_{\text{prod}})^2}{2} + \frac{(C\sigma_{\text{prod}})^3}{6} + O((C\sigma_{\text{prod}})^4) \;, \tag{4.29}$$

which makes it possible to cancel out the first order in σ_{prod}, showing the dependency of the correction on σ_{prod}:

$$\frac{\Delta\sigma}{\Delta p_{\text{lab}}\Delta p_T} = \frac{\Delta n}{N_{\text{beam}}\Delta p_{\text{lab}}\Delta p_T} \cdot C^{-1}\left[1 - \frac{C\sigma_{\text{prod}}}{2} - \frac{(C\sigma_{\text{prod}})^2}{6} + O((C\sigma_{\text{prod}})^3)\right]^{-1} \tag{4.30}$$

The term $C\sigma_{\text{prod}}$ is a small correction. With $\sigma_{\text{prod}} = 172$ mb for $p_{\text{beam}} = 158$ GeV/c and $\sigma_{\text{prod}} = 178$ mb for $p_{\text{beam}} = 350$ GeV/c [35] the correction can be computed. As a result, the target constant is corrected by approximately 1.6 % towards a smaller value. If the correction to C is rounded to the third significant digit, the same effective target constant appears for 158 GeV/c and 350 GeV/c beam momentum:

$$C_{\text{eff},158} \approx C \cdot 0.984 \approx 0.1816 \text{ b}^{-1} \tag{4.31}$$

$$C_{\text{eff},350} \approx C \cdot 0.984 \approx 0.1816 \text{ b}^{-1} \tag{4.32}$$

Henceforth, the index for the beam momentum in C_{eff} can be dropped and the formula reads as follows:

$$\frac{\Delta\sigma}{\Delta p_{\text{lab}}\Delta p_T} = \frac{\Delta n}{N_{\text{beam}}\Delta p_{\text{lab}}\Delta p_T} \cdot C_{\text{eff}}^{-1} \quad \text{in} \quad \left[\frac{\text{mb}}{(\text{GeV}/c)^2}\right] \tag{4.33}$$

This quantity is called “differential inclusive cross section of negatively/positively charged hadrons” and is shown in the final results (Fig. 5.1, Fig. 5.2, and Table H.4).

4.6.2. Mean multiplicity in production events

In this work, production events are defined as events with an inelastic interaction in which particles are created via pair production. This excludes quasi-elastic interaction.

The track multiplicities calculated in the previous sections include all types of interaction. However, as described in the following, contributions from elastic and quasi-elastic interactions can be neglected.

In an elastic interaction, the absolute value of the momentum of the projectile stays practically unchanged. The spectrum of the scattered projectile is very rapidly decreasing with θ [19]. Thus, there are practically no tracks expected within the acceptance for 158 GeV/c and 350 GeV/c beam momentum.

In a quasi-elastic interaction, the nucleus disintegrates and releases numerous core fragments. However, the momentum of the fragments is generally very low so that they are barely within the acceptance of this work.

Assuming that all tracks selected for the track multiplicity are production events, the inclusive cross section calculated in the previous section can be used to compute the “mean multiplicity in production events” via Eq. 4.25 with σ_{prod}, the production cross section measured in [19].

Table 4.8.: List of systematic and statistical uncertainties studied in this work. The individual components are discussed in Section 4.7.

Uncertainty	Calculation
Model uncertainty of MC correction	multiple contributions with $\frac{\lvert c_{\text{VENUS}}-c_{\text{EPOS}}\rvert}{2}$
Statistic Monte Carlo	Gaussian error
Normalization procedure	Error propagation of $P(T2_{in})$ and $P(T2_{out})$
T2 bias correction	Statistical error of fit of $f(p, p_T)$
Track topology	$\frac{\lvert \Delta n_{\text{WST}}-\Delta n_{\text{RST}}\rvert}{2}$
Statistic measured data	Gaussian error

4.7. Study of uncertainties

Table 4.8 lists the uncertainties studied in this work. The systematic uncertainty is an estimation based on a list of contributions without any claim to completeness. For example, it does not cover every possible contribtution from the open questions described in the next section. Fig. 4.8 illustrates the contributions to the total uncertainty for negatively charged tracks at 350 GeV/c beam momentum. Similar plots for positively charged tracks and for 158 GeV/c beam momentum can be found in the appendix, see Section G.

Model uncertainty of Monte Carlo correction

The Monte Carlo correction is a crucial part of this analysis. To study its reliability and estimate an uncertainty of the correction is very important. In the following, the method of estimating the model uncertainty is presented.

For this analysis, two different primary generators have been chosen, namely VENUS and EPOS. Since they generate different particle spectra, it is expected that the two generators will predict slightly different correction factors. This is especially true for the number of electrons, the number of decaying particles (feed down) and secondary interactions. Some of the quantities might cancel out with each other, such as the loss and gain due to secondary interactions. In order to recognize this behavior, four individual parameters of the Monte Carlo correction have been compared individually. They are

- e/μ contamination,
- loss,
- gain from feed down, and
- gain from secondary interaction.

The uncertainty $\sigma(c)$ of an individual parameter is estimated as

$$\sigma(c) = \frac{\lvert c_{\text{VENUS}} - c_{\text{EPOS}}\rvert}{2} \tag{4.34}$$

with c being the corresponding correction factor. Since the correction factors c are proportional to the track multiplicities, the relative uncertainty $\sigma(c)/c$ propagates directly to the final results, making $\sigma(c)/c$ a direct estimator of the uncertainty. The factor two in Eq. 4.34 accounts for the fact that the Monte Carlo correction for the final results is done with averaged correction factors from VENUS and EPOS.

In a second step, the uncertainties of the individual parameters are combined by taking the quadratic sum of the relative uncertainties labeled with index i:

$$\frac{\sigma(c_{\text{total}})}{c_{\text{total}}} = \sqrt{\sum_i \frac{\sigma(c_i)}{c_i}} \tag{4.35}$$

Before calculating the quadratic sum, the individual contributions have been smoothed, and where applicable, interpolated and extrapolated according to the procedure described in Section B.

The individual components of the model uncertainty of MC correction are shown in Fig. 4.7 for negatively charged hadrons at 350 GeV/c beam momentum. Similar plots for positively charged tracks and for 158 GeV/c beam momentum can be found in the appendix, Section G.

Generation of secondary interactions

The Monte Carlos simulations used in this work both rely on the same secondary generator, namely GCALOR. Thus, it is not directly possible to study a systematic uncertainty regarding the loss and production of particles due to secondary inelastic interactions. Indirectly, however, this is done by the fact that the primary spectrum (from EPOS / VENUS) differs which in turn leads to different magnitudes of loss and production in secondary inelastic interactions. Further discussion can be found in Section 4.8.4.

Statistical uncertainty of Monte Carlo correction

In addition to the uncertainties estimated from the comparison of VENUS and EPOS, the Monte Carlo correction factor has also a statistical uncertainty. It has been approximated as a Gaussian uncertainty stemming from number of selected tracks in a particular bin, which is a reasonable approximation since the number of tracks is usually large.

The number of simulated tracks is considered to be accurate. In the Monte Carlo correction for the final results a total number of $8 \cdot 10^6$ simulated events is used for each beam momentum. Thereby, the statistical uncertainty of the Monte Carlo correction factor is approximately half that of the data, see Fig. 4.8 for comparison.

Uncertainty of normalization procedure

Since $T2 \subset T1$, and the trigger probabilities are calculated in a T1 sample, the T2 events are a selection of the T1 events. Hence, N_{T2} is described by a binomial distribution in a sample of size N_{beam}. The estimated uncertainty of P is then given by

$$\sigma(P) = \sqrt{\frac{P \cdot (1-P)}{N_{\mathrm{beam}}}} \,. \tag{4.36}$$

The systematic uncertainty of the normalization is estimated by the propagation of the uncertainty of $P(T2_{\mathrm{in}})$ and $P(T2_{\mathrm{out}})$ to the result via Eq. 4.9 and Eq. 4.10 and is correlated for all bins.

Uncertainty of T2 bias correction

As described in the previous section, the T2 bias correction is based on a fit of unbiased data points. The data points are afflicted with statistical uncertainties. Those uncertainties propagate to the covariance matrix of the fit and eventually to every value that is evaluated by means of the fitted function. This is the uncertainty meant by the reference of the uncertainty of "T2 bias correction".

The uncertainty attributed to the fact that the fit function is an approximation is not studied in this work.

Uncertainty associated with track topology

Uncertainties regarding the track properties can be studied by looking at RST and WST (see Fig. 4.2 for definition of RST and WST). RST and WST are two clearly separable sets of track topologies. Henceforth, the uncertainty obtained from the comparison of RST and WST is referred to as track topology.

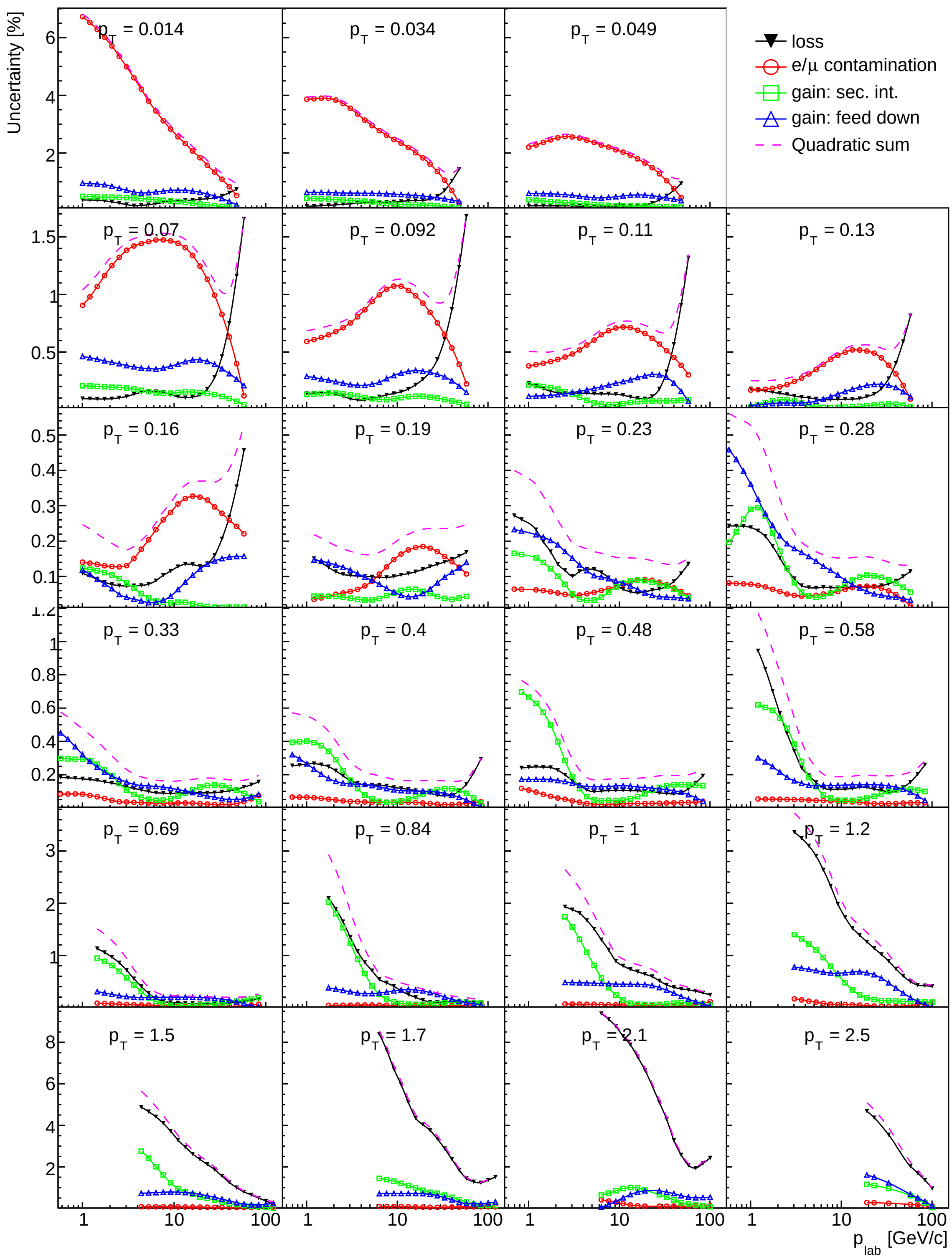

Figure 4.7.: Calculation of the model uncertainty of MC correction for h^- at 350 GeV/c. The individual components are discussed in Section 4.7. Transverse momentum p_T is given in GeV/c.

The track multiplicities are obtained on the basis of RST and WST separately and then compared with each other. The uncertainty σ is estimated as:

$$\sigma = \frac{|n_{\mathrm{WST}} - n_{\mathrm{RST}}|}{2} \tag{4.37}$$

The factor two accounts for the fact that the final results are obtained with the full data set of RST and WST.

Statistical uncertainty of measured data

As the number of measured events is limited, the number of selected tracks in an individual bin is limited too. This becomes especially important for bins in phase space with a relatively low multiplicity, namely large p_T and large p. The statistical uncertainty is expected to be Gaussian, thus calculated by the square root of the number of selected tracks in a particular bin.

Calculation of systematic and total uncertainty

The total uncertainty is calculated as the quadratic sum of the contributions listed in Table 4.8. The systematic uncertainty is calculated as the quadratic sum of all but the last of the contributions.

Discussion of uncertainties

This paragraph addresses the dominant features of the total uncertainty on the example of negatively charged hadrons at 350 GeV/c beam momentum (Fig. 4.8). Plots for positively charged hadrons and 158 GeV/c beam momentum (Section G) are not discussed in detail.

Looking at bins with $p_T \leq 0.07$ GeV/c in Fig. 4.8, the uncertainty of Monte Carlo is dominating. This can be explained with the high electron contamination in those bins, as can be seen in the breakdown of the Monte Carlo uncertainty (Fig. 4.7). From $p_T = 0.092$ GeV/c to $p_T = 1.2$ GeV/c the contributions from various sources to the total uncertainty are of the same order of magnitude and mostly smaller than 1%.

The statistical uncertainty of the data goes up for large and small p, as well as for small and large p_T, which is due to the acceptance cut at the edges of the geometrical acceptance. It also goes up when there is a partial *hole* in the acceptance, for example at $p_T = 0.23$ GeV/c around $p = 1$ GeV/c.

The statistical uncertainty of the Monte Carlo is always smaller than that of the data. The uncertainty estimated from the T2 bias is small compared to other contributions. The normalization procedure, however, contributes to the total uncertainty with a value around 1% relatively homogeneously over the entire phase space. The uncertainty associated with the track topology is mostly small but shows some rises at high p, which are due to limited statistics in the estimation of the uncertainty.

Bins with $p_T \geq 1.5$ GeV/c show increasingly large uncertainties. This is mainly due to the statistical uncertainty of the data and Monte Carlo. The estimation of other errors then becomes less efficient and a possible double counting of statistical fluctuations can not be fully excluded.

Generally, the total uncertainty is less than 2% for bins of high statistics. Only where the statistics is limited or the Monte Carlo corrections dominate, the total uncertainty rises up to values in the order of 30%.

4.8. Open questions

During the time of this work not all open problems could be solved. This section presents a brief discussion of each of them.

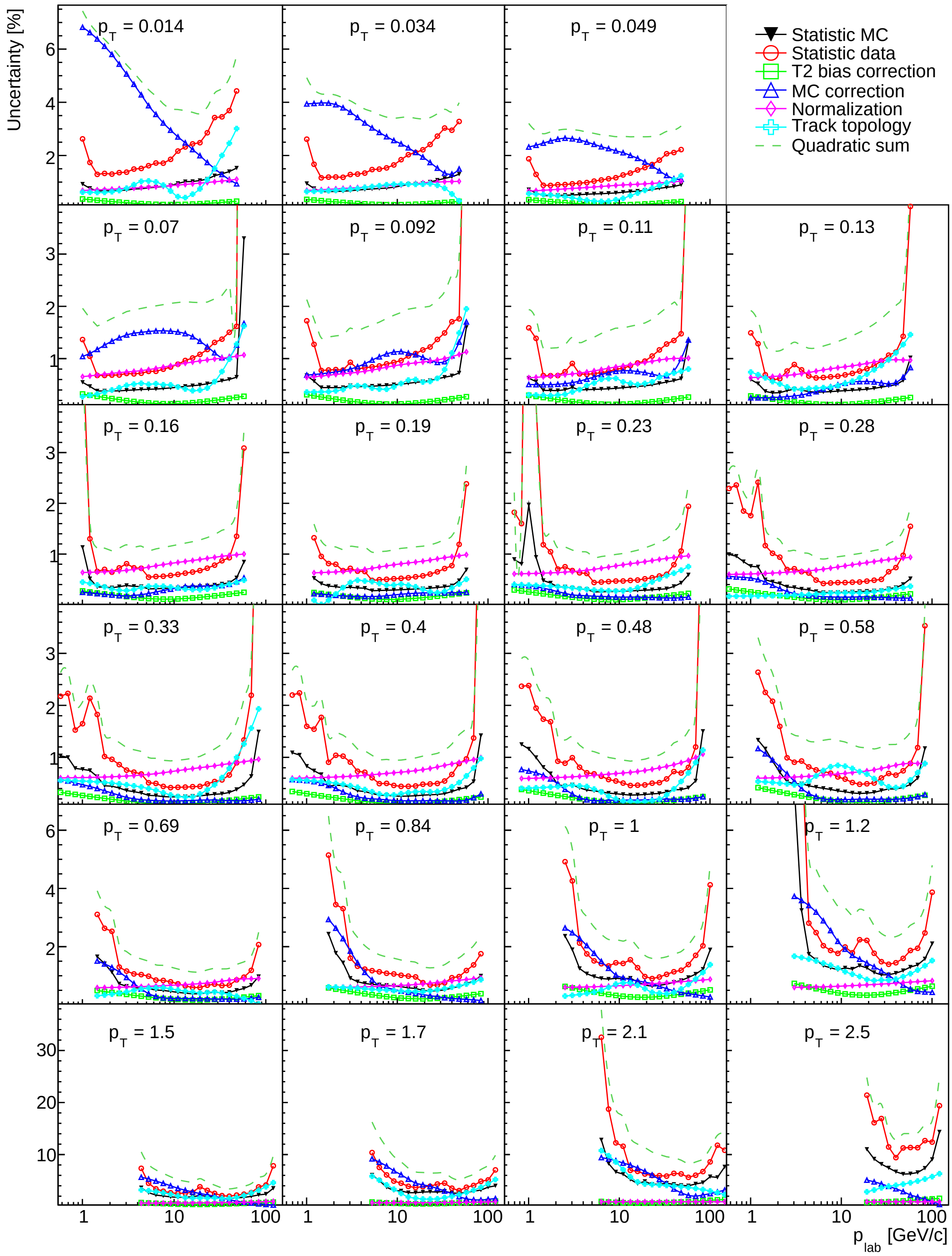

Figure 4.8.: Calculation of the total uncertainty for h^- at 350 GeV/c. The individual components are discussed in Section 4.7. Transverse momentum p_T is given in GeV/c.

4.8.1. Target position

Originally, the z position of the thin target in 2007 was measured to be $z = -580.4$ cm [22]. The value which was assumed for 2009 is somewhat inconsistent. Recent investigations showed that the most probable value for center of the real target position in 2009 is $z = -580.8$ cm [36].

In this analysis, the BPD vertex position of reconstructed data and Monte Carlo is at $z = -581.41$ cm. In the MC simulations, the vertices are simulated at $z = -580.41 \text{ cm} \pm 1$ cm, suggesting the center of the target at $z = -580.41$ cm.

Ideally, one would use the best guess of the real target position and adjust the geometry in the simulation as well as change the BPD vertex position in the reconstruction of the data and the MC files. This, however, requires a rerun of data and Monte Carlo reconstruction which was not available at the time of this thesis.

However, as it seems the simulated target position differs only by 0.4 cm form the real one. The effect is likely to be negligible. Also the fact that the BPD vertex position is non-ideal (offset: 0.6 cm) will most certainly have a negligible impact, since it is a small displacement and the same mistake in done in MC and data, thus it is corrected for in the MC correction procedure.

4.8.2. Calibration

The data sets that were used in this work are not fully calibrated. The final drift velocity correction for the GAP-TPC was not included in the data sets yet. The possibility of a bias on the results due to this fact has not been studied systematically but is expected to be negligible.

4.8.3. Momentum resolution

The study of momentum resolution performed in Section 3.1 relies fully on Monte Carlo. If the Monte Carlo does not reproduce the reality sufficiently well, the correction of the migration could be slightly wrong.

4.8.4. Systematics regarding the secondary Monte Carlo generator

As presented in Section 4.7, the systematic uncertainty of the secondary generator can not be determined directly. For direct estimation, a set of Monte Carlo simulations with different secondary generators would be needed.

A large fraction of the secondaries that are reconstructed as main vertex tracks stem from inelastic interactions in the target. The effect of the choice of secondary generator for those secondaries could be studied separately.

For that purpose, a dedicated simulation of the target only would be applicable. In this case, the particles from the primary generator (for example VENUS or EPOS) are placed in the target. The transportation trough the target is done with GEANT. Any given secondary generator can be used for the inelastic interactions in the target. The hadroproduction spectrum of different secondary generators can then be compared, thus providing an estimate on the model uncertainty of this Monte Carlo correction.

4.8.5. Beam divergence

The beam divergence during the runs is approximately 0.3 mrad for the runs at 350 GeV/c beam momentum and approximately 0.1 mrad for the runs at 158 GeV/c [19]. In the binning of this work, the upper edges of bins for the highest momenta are as small as 0.3 mrad. This is in the order of the beam divergence. The momenta of tracks are calculated with respect to the detector coordinates and not with respect to the beam coordinates. Thus, the measured momenta have to be disentangled from the beam divergence. The influence on the spectra can be neglected if the production angles are large. However, for bins with low production angle, a non negligible migration is expected.

Still, the momenta cannot simply be calculated with respect to the beam momentum for two reasons. Firstly, the systematic uncertainty of the alignment of the beam position detectors have not been evaluated yet. The application of it might introduce an unnecessary bias. Secondly, the acceptance definition would not be valid anymore in the way it is used in this work. In the Monte Carlo simulations, no beam divergence is simulated. The correction of the acceptance assumes that particles are produced with zero beam divergence, thus being symmetric in ϕ. But since in the real detector the production of particles is folded with the beam profile, this assumption does not hold anymore. Indeed, it has been found that the beam profile is not symmetric with respect to ϕ and its mean in x and y direction is substantial larger than zero.

A solution would be a Monte Carlo simulation with the proper beam divergence simulated. Then, future studies should take advantage of the known beam of every event and calculate the momenta with respect to the beam vector, assuming the reconstruction of the beam vector is precise and well calibrated.

From a comparison of the spectra obtained from the momentum with respect to the detector and with respect to the beam, it was found that the difference in the spectra is up to 30% for less than 5 bins for each charge. For the other bins the difference is less than 10% and the average is 0.7%. The comparison was performed with T2 events at 350 GeV/c beam momentum

4.8.6. RST/WST issue for positively charged hadrons

In this work RST and WST are assumed to be of equal quality. This is not a trivial statement because RST and WST ought to have a different detector response. In fact, at NA49, WST have not been used for analysis.

The analysis of this work exhibits a discrepancy between positive RST and WST that is currently not understood. The discrepancy appears at both beam momenta but not for negatively charged hadrons. If the analysis (including the Monte Carlo corrections) is performed independently for RST and WST, the resulting spectra look different, as can be seen in Fig. 4.9. The difference appears more dramatic if the difference of RST and WST in units of standard deviation (pull) is compared (Fig. 4.9).

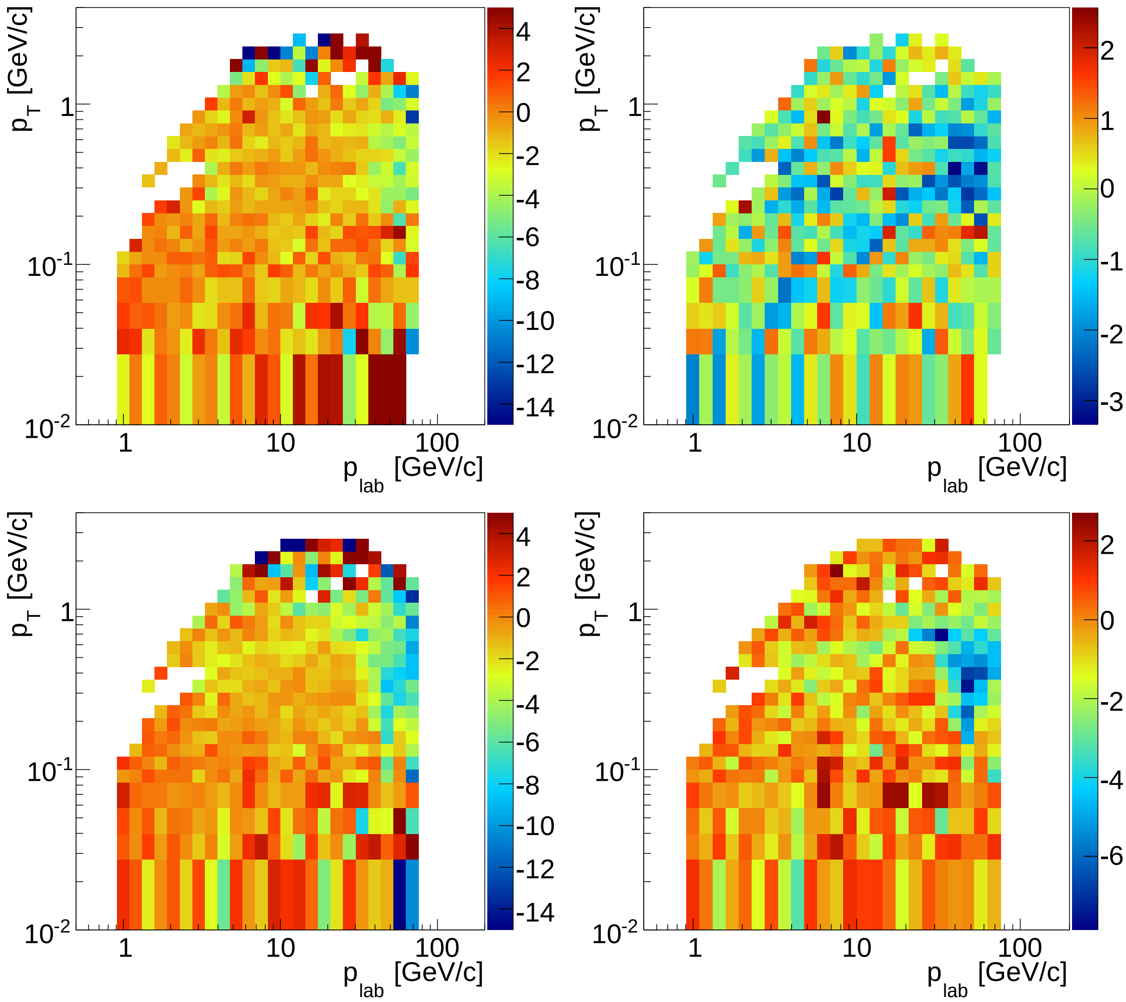

Figure 4.9.: Illustration of RST/WST issue for positively charged hadrons at 158 GeV/c beam momentum (top panels) and 350 GeV/c beam momentum (bottom panels). Left panels: Relative difference of WST and RST in %. Right panels: Pull of WST and RST in units of standard deviation.

5. Results and discussion

In this chapter, the results of this analysis, namely the inclusive spectra of charged hadrons, are presented. Furthermore, the phase space coverage of the results is shown along with its relevance for the measurements of muons at ground level for surface detectors. Finally, the mean multiplicity in production events of the results of this work is compared with the predictions of a variety of hadronic interaction models used for the analysis of data of extensive air showers.

Differential inclusive cross section

Fig. 5.1 and Fig. 5.2 show the differential inclusive cross section (Eq. 4.33) with its total uncertainty for negatively and positively charged hadrons in $\pi^- + \mathrm{C}$ interactions at 158 GeV/c and 350 GeV/c beam momentum respectively. In the appendix, Table H.4 lists the differential inclusive cross section of all measured data including exact values of the binning and the size of the statistical and systematic uncertainty.

Phase space coverage and its relevance for the measurement of muons

One of the major goals of this work is to present measurements that are relevant for interactions models that predict the number of muons of extensive air showers at ground level. For that purpose, Monte Carlo simulations of extensive air showers have been performed with the focus on the momentum distribution of grandmother, mother and daughter particles [15]. To study the relevance of phase space bins, the spectrum of the mother particles that are expected to cause a muon signal in the surface detectors of a typical experiment is plotted for grandmother momenta around 158 GeV/c and 350 GeV/c. The acceptance of this work is superimposed for comparison. Fig. 5.3 shows the comparison for typical shower energies and detector setups of KASCADE, KASACDE-Grande, and the Pierre Auger Observatory.

As can be seen, the acceptance of this work covers a large part of the regions of interest in all three detector arrays.

Comparison with models

Given the importance of the low energy region for the number of muons, it is interesting to compare the results of this work with interaction models that are used in shower simulations. In the following the results are compared with a selection of models, namely EPOS [2], FLUKA [37], QGSJet-01 [38], QGSJet-II [39], Sibyll [40], UrQMDpatched [41], and VENUS [42]. The version number can be found in the plots. UrQMDpatched refers to the fact that changes to the source code, as proposed in [43], are applied. The simulation

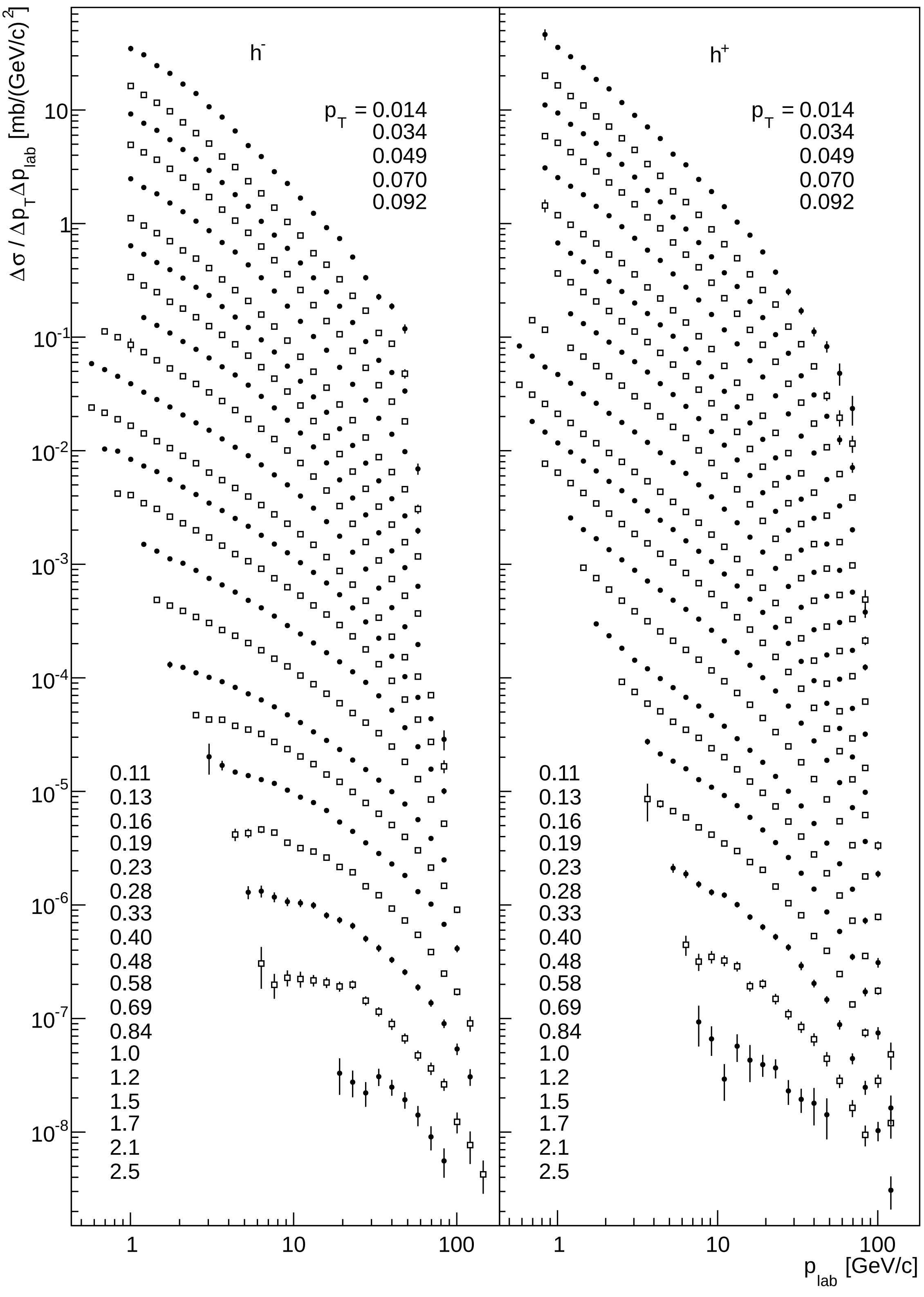

Figure 5.1.: Differential inclusive cross section for negatively and positively charged hadrons in π^-+C interactions at 158 GeV/c beam momentum. Error bars show total uncertainty. Except for p_T = 0.014 GeV/c, the data points are divided successively by 6 up to p_T = 0.034 GeV/c, by 2.5 up to p_T = 0.11 GeV/c, by 2 up to p_T = 0.33 GeV/c, and by 1.5 up to p_T = 0.84 GeV/c to allow for a better separation. Data points from p_T = 1 GeV/c are not divided by additional factors. Transverse momentum p_T is given in GeV/c.

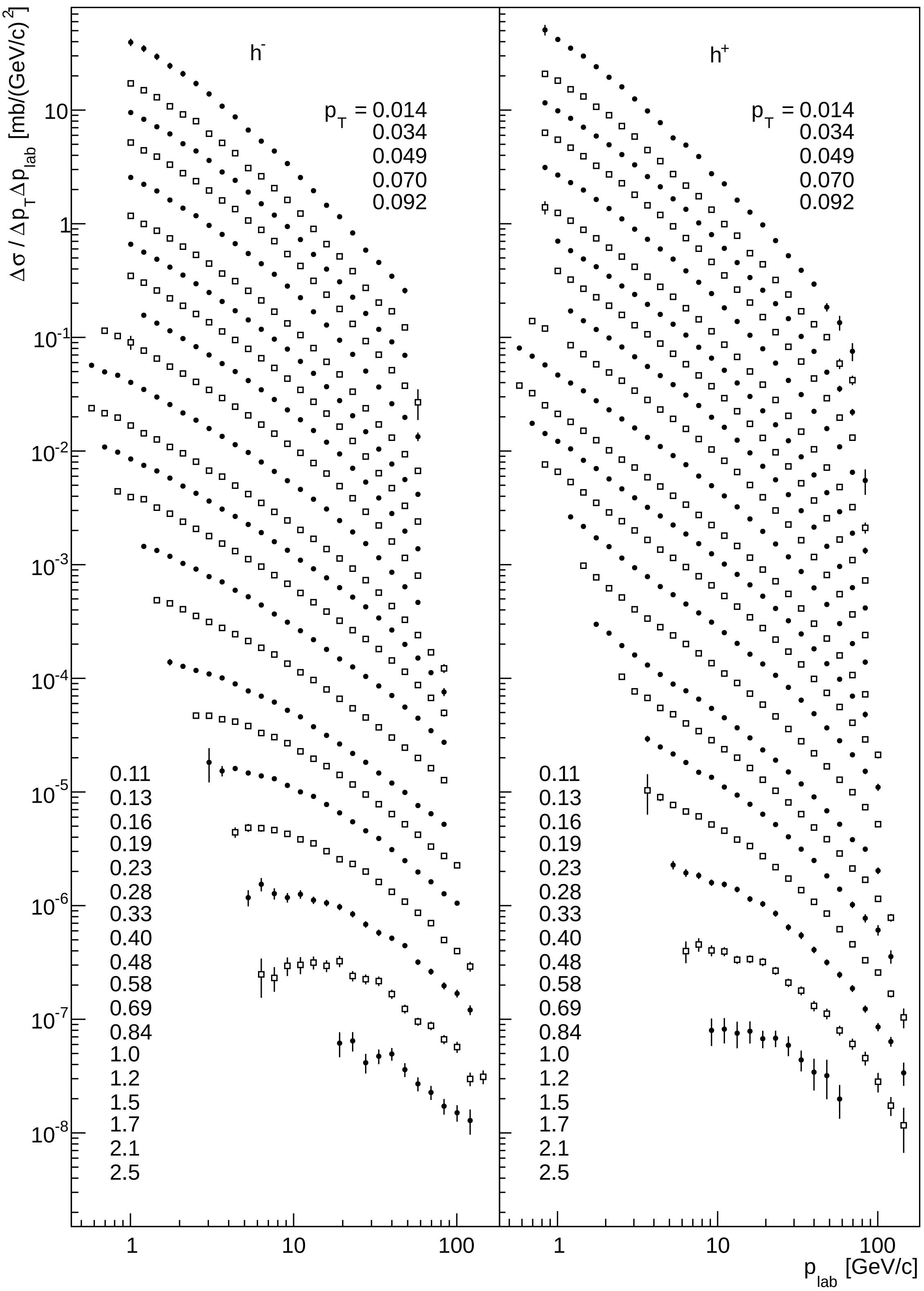

Figure 5.2.: Differential inclusive cross section for negatively and positively charged hadrons in π^-+C interactions at 350 GeV/c beam momentum. Error bars show total uncertainty. Except for $p_T = 0.014$ GeV/c, the data points are divided successively by 6 up to $p_T = 0.034$ GeV/c, by 2.5 up to $p_T = 0.11$ GeV/c, by 2 up to $p_T = 0.33$ GeV/c, and by 1.5 up to $p_T = 0.84$ GeV/c to allow for a better separation. Data points from $p_T = 1$ GeV/c are not divided by additional factors. Transverse momentum p_T is given in GeV/c.

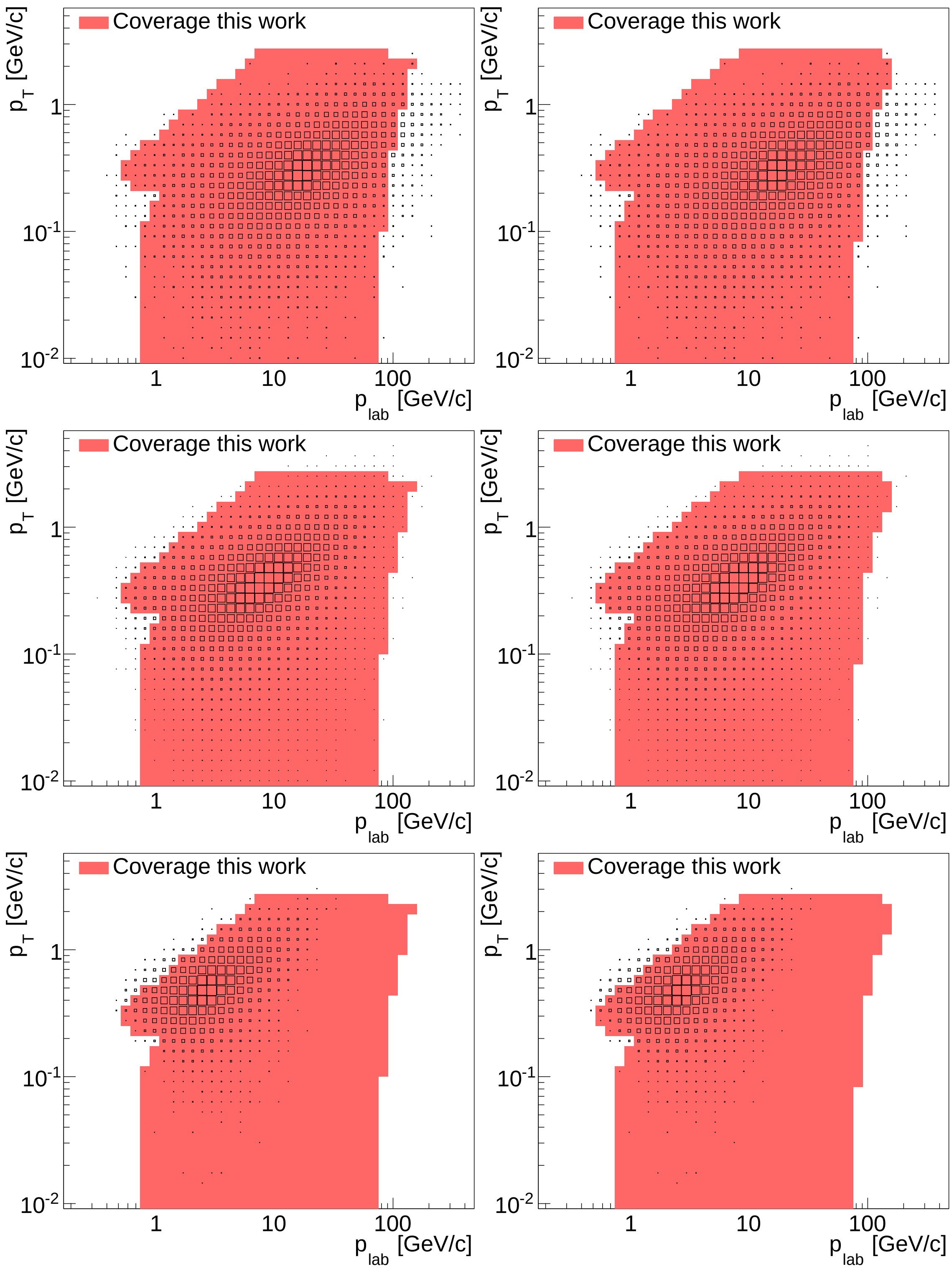

Figure 5.3.: Relative importance of phase space bins (boxes) for the number of measured muons on ground level for the experiments KASCADE (top panels), KASACDE-Grande (centered panels), and the Pierre Auger Observatory (bottom panels) superimposed with the NA61 acceptance (red contour) of this work at beam energies of 158 GeV/c (left panels) and 350 GeV/c (right panels). The momentum of the selected grandmother particles ranges from 148 GeV/c to 168 GeV/c (left panels) and from 330 GeV/c to 370 GeV/c (right panels). Shower simulation performed with QGSJet-II and Fluka with a transition from the high energy model to the low energy model at $E = 80$ GeV [15].

output was produced with CORSIKA-6990 [44]. The events obtained from the CORSIKA output are production events. A comparison with the measurements of this work can be done if

- the measured data is normalized to the mean multiplicity in production events or
- the cross section that is used in the models to generate the production spectra is used to calculate the inclusive cross section.

Since the latter was not possible at the time given, the first option was chosen even though the uncertainty of the cross section additionally increases the uncertainty on the measured data.

Fig. 5.4, Fig. 5.5, Fig. 5.6, and Fig. 5.7 show the ratio of data to Monte Carlo of the mean multiplicity in production events. The uncertainty is depicted with a gray band around one and is estimated by calculating the quadratic sum of the total uncertainty from this analysis and the statistical and systematic uncertainty from the cross section measurement [19].

Generally it can be said that the measurements of this work provide an extensive data set that could be used to tune interaction models. In many bins, the total uncertainty is smaller than the typical difference of models. Thus, it is possible, to make a judgment on the basis of this work regarding the quality of the models to describe the data.

The impression from the figures is that QGSJet-II and EPOS describe the data best. However, discrepancies at the level of 30% or more still exist in both models which would suggest that a tuning of the models to the data can be performed.

From the sole comparison of the spectra it is not easy to foresee how the measurements of $\pi^- + \mathrm{C}$ interactions at 158 GeV/c and 350 GeV/c will influence the model predictions of the number of muons at ground level and the related open questions mentioned in the beginning. However, there is one feature that might hint in a direction that would diminish the muon deficit as observed in the Pierre Auger Observatory. In high p_T bins, the fraction of measurement to model prediction is for most bins significantly above one. This means, the measurement has found a high inclusive cross section for high p_T hadrons, the spectrum is *harder* in p_T than predicted by most models. Due to the geometrical setup of the surface detectors at the Pierre Auger Observatory, muons that are detected are particularly created in decays of mother particles of a large production angle. High p_T corresponds to large angles, thus predictions on the basis of this work would enhance the number of measured muons by suggesting an increased number of high p_T mother particles. Nevertheless, it must be said that despite this feature, the measurements of this work not necessarily suggest that the total number of muons measured at ground level will also increase. To judge this, the relative importance of the individual regions of phase space to the number of muons at ground level has to be taken into account as well.

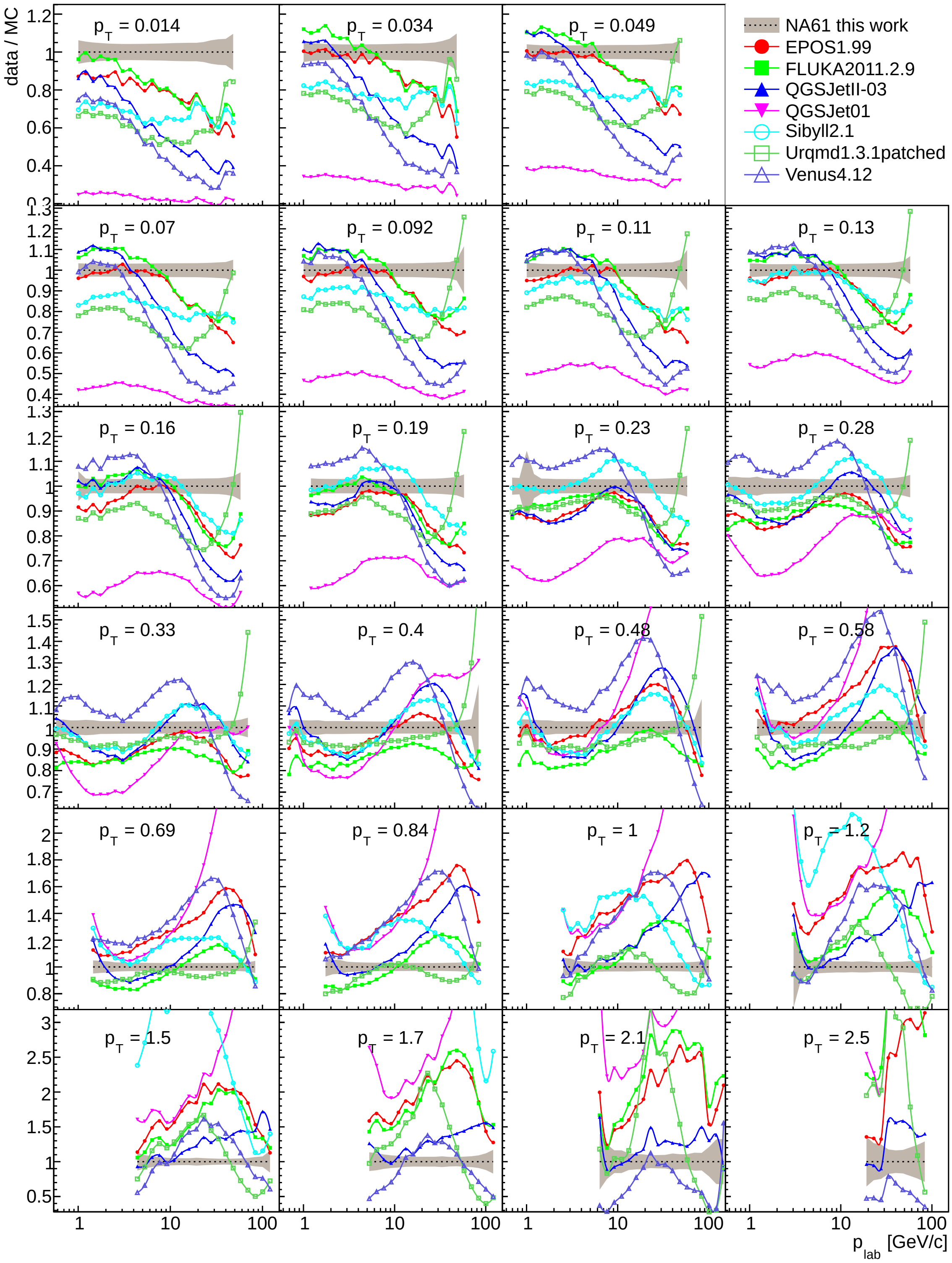

Figure 5.4.: Comparison of mean multiplicity in production events between data and various interaction models for negatively charged hadrons produced at 158 GeV/c beam momentum. The uncertainty, depicted by the gray band around one, includes the total uncertainty from this analysis and from the production cross section measurement [19]. Transverse momentum p_T is given in GeV/c.

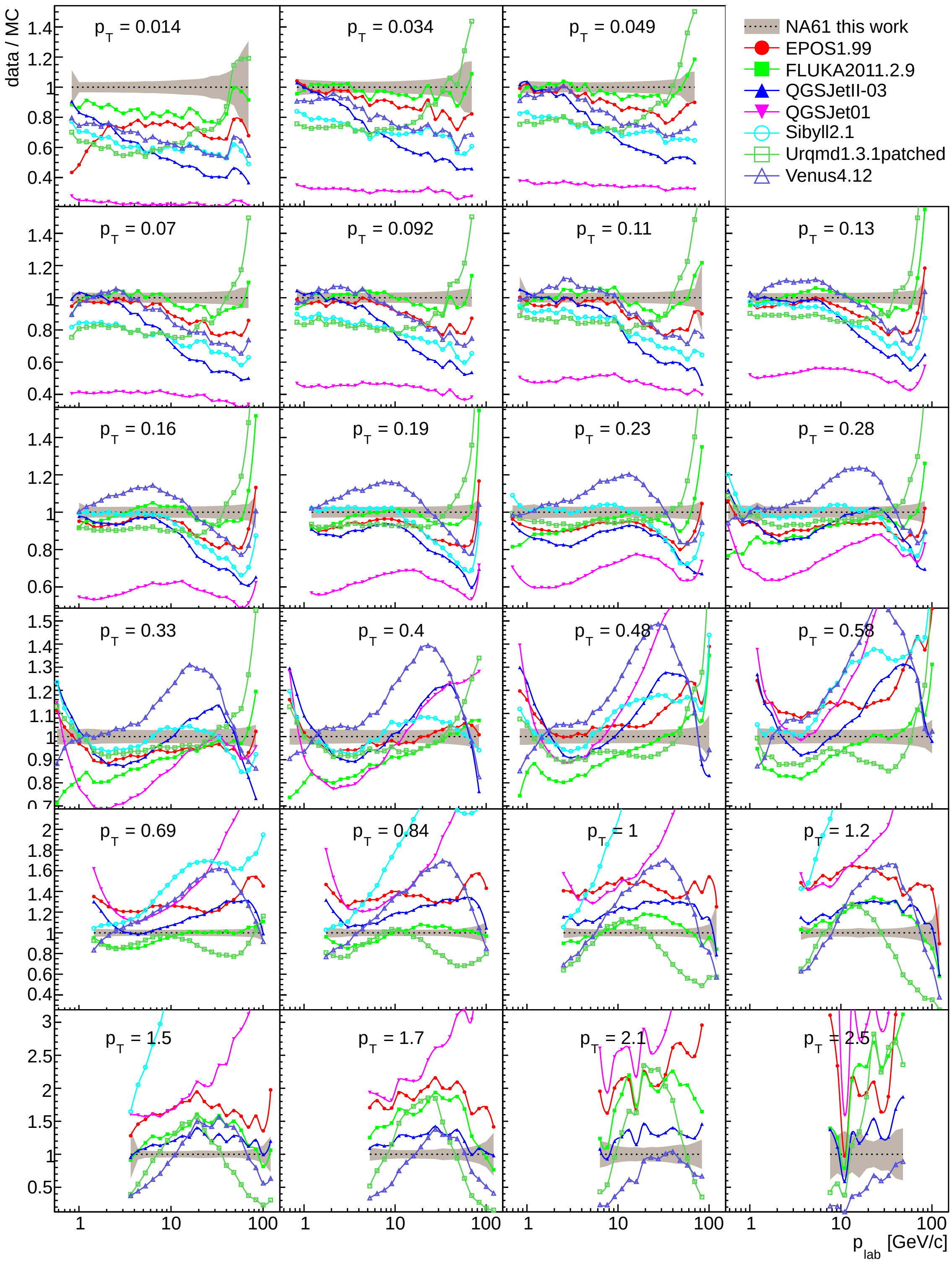

Figure 5.5.: Comparison of mean multiplicity in production events between data and various interaction models for positively charged hadrons produced at 158 GeV/c beam momentum. The uncertainty, depicted by the gray band around one, includes the total uncertainty from this analysis and from the production cross section measurement [19]. Transverse momentum p_T is given in GeV/c.

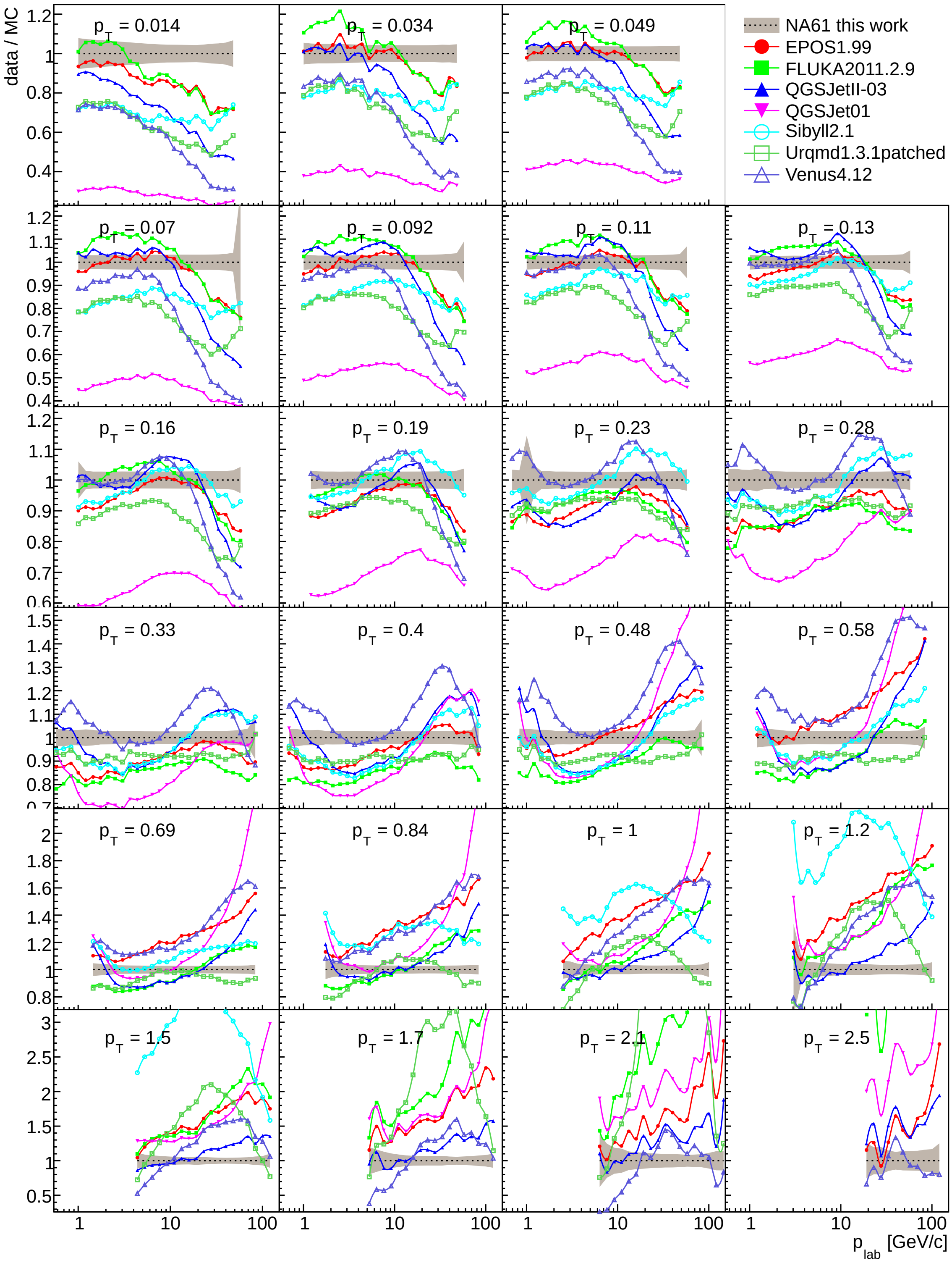

Figure 5.6.: Comparison of mean multiplicity in production events between data and various interaction models for negatively charged hadrons produced at 350 GeV/c beam momentum. The uncertainty, depicted by the gray band around one, includes the total uncertainty from this analysis and from the production cross section measurement [19]. Transverse momentum p_T is given in GeV/c.

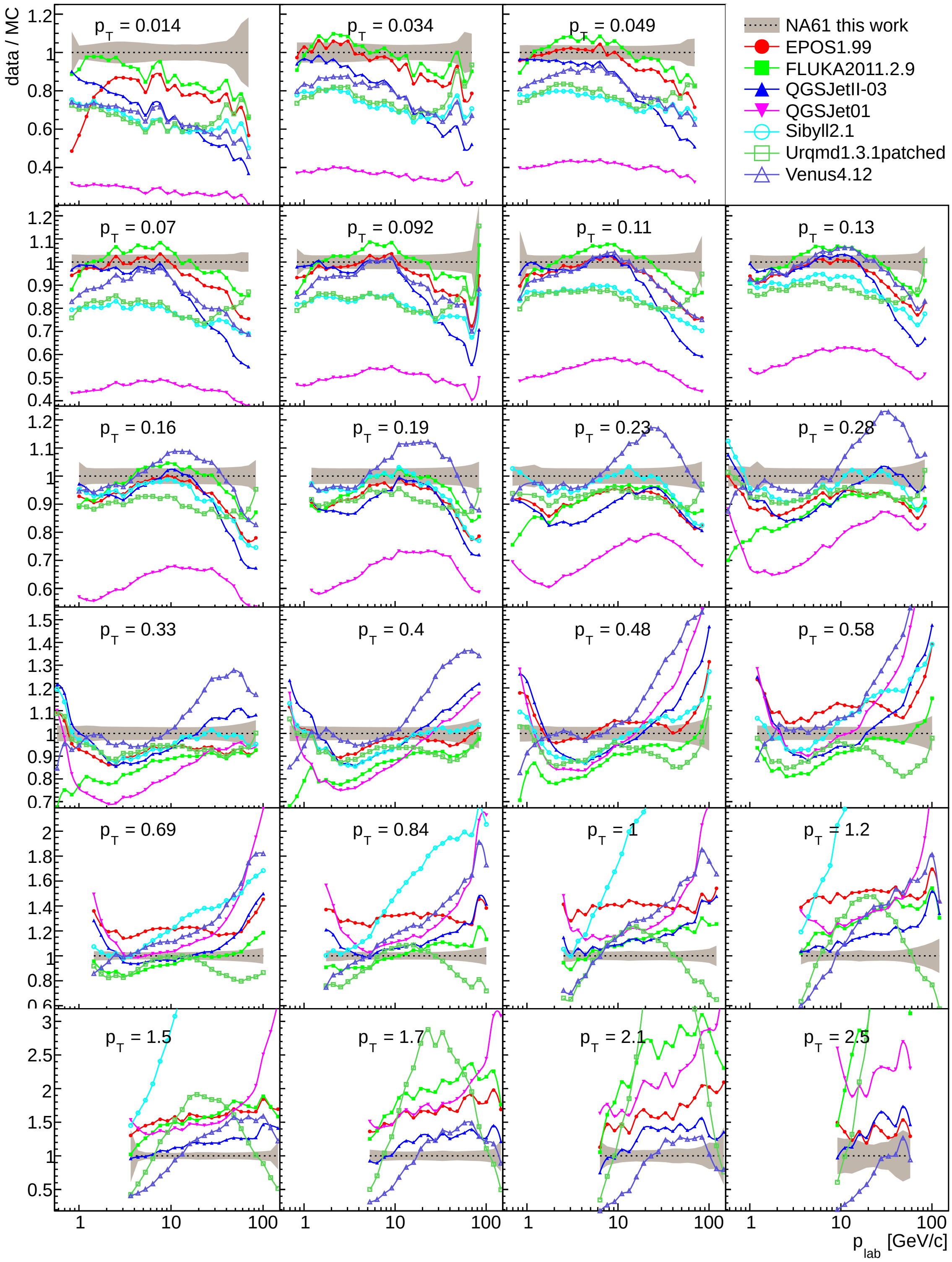

Figure 5.7.: Comparison of mean multiplicity in production events between data and various interaction models for positively charged hadrons produced at 350 GeV/c beam momentum. The uncertainty, depicted by the gray band around one, includes the total uncertainty from this analysis and from the production cross section measurement [19]. Transverse momentum p_T is given in GeV/c.

6. Summary and outlook

The last stages of particle cascades initiated by ultra-high-energy cosmic rays are important for the number of muons measured at ground level. Due to the lack of reference measurements, current interaction models are based on extrapolations to predict the relevant particle spectra in the low energy region of an air shower. Thus, measurements such as the one studied in this work are important for a better understanding of observations of extensive air showers with ground based detectors.

In this work, a measurement of the differential inclusive cross section of negatively and positively charged hadrons in $\pi^- + \mathrm{C}$ collisions at beam energies of 158 GeV/c and 350 GeV/c was presented. The estimated total uncertainty of the measurements is on average 3% with a maximum of 47%.

It was shown that the acceptance of this analysis covers well the regions of interest with respect to the number of muons at ground level for the selected beam energies at three major surface detector experiments for extensive air showers.

In the analysis chapter, the method of extracting the inclusive cross sections was described. The selection criteria of events and tracks were introduced along with the method of target-out subtraction and normalization. In particular, a new, geometrical approach for the definition of the acceptance was developed, based on a selection of fiducial regions in ϕ for which the track detection efficiency of the time projection chambers is close to unity. Furthermore, Monte Carlo corrections were discussed and a novel method of a data-driven correction of the trigger bias, which takes advantage of other trigger sets with less bias and sets without bias, was introduced. Both, the fiducial acceptance and the method for the correction of the trigger bias developed in this work, are now standard methods in NA61 analyses. Moreover, studies of statistical and systematic uncertainties were performed with a focus on uncertainties that arise from different contributions to the Monte Carlo correction factors.

A comparison of the results with current interaction models showed that there is indeed room for improvement of the latter. The total uncertainty of the results of this work is small enough to allow a bin-wise discrimination between models that fit the data well and those that do not. According to the measurements of this work, even the most recent interaction models show deviations in the order of 30% and do not fully reproduce the measurements over the phase space covered by this work.

As decided at the NA61 Collaboration meeting in Budapest, Hungary (14-19 May 2012), preliminary results of charged hadron spectra will be released in summer 2012. The spectra will be largely based on the methods and results of this work.

Nevertheless, this work will not be the last analysis performed on the $\pi^- + \mathrm{C}$ data sets recorded in 2009. For future studies, the cause of one of the largest contributions to the systematic uncertainty should be addressed, namely the fact that the contamination with electrons is removed on the basis of model predictions only. This will be possible by using the energy deposit per track for particle identification, for which the data is currently reprocessed with new calibration constants.

Once the method of particle identification is implemented, the next step is a full particle identification of hadrons. This would result in differential spectra for $\pi^{\pm}$, $K^{\pm}$, p, and $\bar{p}$ individually. Hence, measurements of the baryon fraction would be available for those interactions and could, for instance, validate or falsify one of the proposed solutions [2] to the muon deficit in ultra-high-energy cosmic ray showers.

Bibliography

[1] J. Linsley, "Evidence for a Primary Cosmic-Ray Particle with Energy 10^{20} eV," *Phys. Rev. Lett.*, vol. 10, pp. 146–148, Feb 1963.

[2] T. Pierog and K. Werner, "Muon production in extended air shower simulations," *Phys. Rev. Lett.*, vol. 101, p. 171101, 2008.

[3] J. Abraham *et al.*, "Properties and performance of the prototype instrument for the Pierre Auger Observatory," *Nucl. Instrum. Meth.*, vol. A523, pp. 50–95, 2004.

[4] T. Antoni *et al.*, "The cosmic-ray experiment KASCADE," *Nucl. Instrum. Meth.*, vol. A513, no. 3, pp. 490 – 510, 2003.

[5] W. Apel *et al.*, "The KASCADE-Grande experiment," *Nucl. Instrum. Meth.*, vol. A620, no. 2–3, pp. 202 – 216, 2010.

[6] K. Nakamura *et al.*, "Review of particle physics," *J. Phys.*, vol. G37, p. 075021, 2010.

[7] R. M. Ulrich, "Measurement of the proton-air cross section using hybrid data of the Pierre Auger Observatory," Ph.D. dissertation, Universität Karlsruhe (TH), 2008.

[8] J. Alvarez-Muñiz, R. Engel, T. K. Gaisser, J. A. Ortiz, and T. Stanev, "Hybrid simulations of extensive air showers," *Phys. Rev. D*, vol. 66, p. 033011, Aug 2002.

[9] J. Bluemer, R. Engel, and J. Hoerandel, "Cosmic Rays from the Knee to the Highest Energies," *Prog.Part.Nucl.Phys.*, vol. 63, pp. 293–338, 2009.

[10] J. Allen, "Interpretation of the signals produced by showers from cosmic rays of 10^{19} eV observed in the surface detectors of the Pierre Auger Observatory," prepared for 32nd International Cosmic Ray Conference (ICRC2011), Beijing, China, 2011.

[11] G. Farrar, "New Physics at UHE energies," presented at the International Symposium on Future Directions in UHECR Physics, CERN, Switzerland, 13-16 February 2012.

[12] T. Antoni *et al.*, "KASCADE measurements of energy spectra for elemental groups of cosmic rays: Results and open problems," *Astropart. Phys.*, vol. 24, pp. 1–25, 2005.

[13] W. Apel *et al.*, "Energy spectra of elemental groups of cosmic rays: Update on the KASCADE unfolding analysis," *Astroparticle Physics*, vol. 31, no. 2, pp. 86 – 91, 2009.

[14] M. Unger, "Hadroproduction Measurements with NA61/SHINE for the Understanding of Extensive Air Showers," 2011, Presented at the 32nd International Cosmic Ray Conference, 2011, Beijing, China.

[15] I. C. Maris, "Hadron Production Measurements with the NA61-SHINE Experiment and their Relevance for Air Shower Simulations," 2009, Presented at the 31st International Cosmic Ray Conference, 7-15 Jul 2009, Lodz, Poland.

[16] C. Meurer, "Muon production in extensive air showers and fixed target accelerator data," Ph.D. dissertation, Universität Karlsruhe (TH), 2007.

[17] T. Eichten *et al.*, "Particle production in proton interactions in nuclei at 24 GeV/c," *Nuclear Physics B*, vol. 44, no. 2, pp. 333 – 343, 1972.

[18] C. Alt *et al.*, "Inclusive production of charged pions in p+C collisions at 158-GeV/c beam momentum," *Eur.Phys.J.*, vol. C49, pp. 897–917, 2007.

[19] M. A. Haug, "Messung des Wirkungsquerschnitts von Pion-Kohlenstoff Wechselwirkungen mit Hilfe des NA61 Detektors," Diploma thesis, Karlsruhe Institute of Technology (KIT), May 1, 2012.

[20] S. Afanasev *et al.*, "The NA49 large acceptance hadron detector," *Nucl. Instrum. Meth.*, vol. A430, pp. 210–244, 1999.

[21] K. Grebieszkow, "NA49 and NA61/SHINE experiments: results and perspectives," *Acta Phys. Polon.*, vol. B41, pp. 427–440, 2010.

[22] C. Strabel, "Evaluation of Particle Yields in 30 GeV Proton-Carbon Inelastic Interactions for Estimating the T2 Neutrino Flux," Ph.D. dissertation, ETH Zurich, 2011.

[23] L. S. Esposito *et al.*, "Cross Sections and Charged Pion Spectra in Proton-Carbon Interactions at 31 GeV/c," 2011, arXiv 1105.5240.

[24] C. Bovet, R. Maleyran, L. Piemontese, A. Placci, and M. Placidi, "The Cedar counters for particle identification in the SPS secondary beams: A description and an operation manual," Sep 1982, CERN-82-13.

[25] M. Unger, "Cosmic runs 2009," 2009, Indico[1] presentation.

[26] Beam detectors and triggering. NA61 webpage. [Online]. Available: https://na61.web.cern.ch/na61/xc/index.html?O=detector/beam-detectors-and-triggering

[27] W. Blum, W. Riegler, and L. Rolandi, *Particle Detection with drift Chambers; 2nd ed.* Berlin: Springer, 2008.

[28] Bethe, H. A. and Ashkin, J., *Experimental Nuclear Physics, Vol.1.*, Segre, E., Ed. John Wiley and Sons, New York, 1953.

[29] R. Sipos, "The Offline Software Framework of the NA61/Shine Experiment," 2012, Presented at the 19th International Conference on Computing in High Energy and Nuclear Physics (CHEP), 21-25 May 2012, New York City, NY, USA.

[30] M. Ruprecht, "Pion-Carbon at 350 GeV/c Charged Hadron Analysis: Selected Issues," 2011, Indico presentation, T2K/CR Analysis EVO Meeting Nov 02, 2011.

[31] F. C. R. Brun and S. Giani, GEANT *Detector Description and Simulation Tool*, CERN Application Software Group, Geneva, Switzerland, March 1994, version 3.21.

[32] C. Zeitnitz and T. Gabriel, "The GEANT-CALOR interface and benchmark calculations of ZEUS test calorimeters," *Nucl. Instrum. Meth.*, vol. A349, no. 1, pp. 106 – 111, 1994.

[33] A. Marcinek. (2010) Bits of bpd_vertex.iflag and possible cuts. [Online]. Available: https://twiki.cern.ch/twiki/pub/NA61/EventTrackCuts/bpd_vertex_iflag.pdf

[34] N. Abgrall *et al.*, "Measurements of Cross Sections and Charged Pion Spectra in Proton-Carbon Interactions at 31 GeV/c," *Phys.Rev.*, vol. C84, p. 034604, 2011.

[35] M. A. Haug, "Messung des Wirkungsquerschnitts von Pion-Kohlenstoff Wechselwirkungen mit Hilfe des NA61 Detektors, überarbeitete Fassung," Diploma thesis, revised version, Karlsruhe Institute of Technology (KIT), May, 2012.

[36] B. Popov. (2012, Jan 31) Geometers' survey measurements to NA61 coordinates system. [Online]. Available: https://twiki.cern.ch/twiki/bin/viewauth/NA61/SurveyToNA61CoordinatesConversion

[37] G. Battistoni, F. Cerutti, A. Fasso, A. Ferrari, S. Muraroi, J. Ranft, S. Roesler, and P. R. Sala, "The fluka code: Description and benchmarking," *AIP Conf. Proc.*, vol. 896, no. SLAC-REPRINT-2007-184, pp. 31–49. 19 p, 2007.

[38] N. N. Kalmykov, S. S. Ostapchenko, and A. I. Pavlov, "Quark-gluon-string model and eas simulation problems at ultra-high energies," *Nuclear Physics B - Proceedings Supplements*, vol. 52, no. 3, pp. 17 – 28, 1997.

[1]Indico (Integrated Digital Conferencing), project site: http://indico-software.org

[39] S. Ostapchenko, "QGSJET-II: towards reliable description of very high energy hadronic interactions," *Nuclear Physics B - Proceedings Supplements*, vol. 151, no. 1, pp. 143 – 146, 2006.

[40] E.-J. Ahn, R. Engel, T. K. Gaisser, P. Lipari, and T. Stanev, "Cosmic ray interaction event generator SIBYLL 2.1," *Phys. Rev. D*, vol. 80, p. 094003, Nov 2009.

[41] M. Bleicher, E. Zabrodin, C. Spieles, S. Bass, C. Ernst *et al.*, "Relativistic hadron hadron collisions in the ultrarelativistic quantum molecular dynamics model," *J.Phys.G*, vol. G25, pp. 1859–1896, 1999.

[42] K. Werner, "Strings, pomerons and the venus model of hadronic interactions at ultrarelativistic energies," *Physics Reports*, vol. 232, no. 2-5, pp. 87 – 299, 1993.

[43] V. Uzhinsky, "How to Improve UrQMD Model to Describe NA61/SHINE Experimental Data," 2011, arXiv 1107.0374.

[44] D. Heck, G. Schatz, T. Thouw, J. Knapp, and J. Capdevielle, "CORSIKA: A Monte Carlo code to simulate extensive air showers," 1998, FZKA-6019.

[45] C. Alt *et al.*, "Inclusive production of charged pions in p+p collisions at 158-GeV/c beam momentum," *Eur.Phys.J.*, vol. C45, pp. 343–381, 2006.

[46] R. Brun and F. Rademakers, "ROOT — An object oriented data analysis framework," *Nucl. Instrum. Meth.*, vol. A389, no. 1-2, pp. 81–86, 1997.

[47] J. H. Friedman, "Smart user's guide," Laboratory for Computational Statistics, Stanford University, Tech. Rep., 1984, technical Report No. 1.

[48] ——, "A variable span scatterplot smoother," Laboratory for Computational Statistics, Stanford University, Tech. Rep., 1984, technical Report No. 5.

Acknowledgment

First, I would like to thank Prof. J. Blümer for reviewing this work and providing me with the opportunity to write the thesis at the “Institute of Experimental Nuclear Physics”.

Prof. M. Feindt, I thank for the intriguing lectures on “Nuclear and Particle Physics” and serving as second reviewer of this thesis.

Furthermore, I acknowledge the support from Dr. R. Engel who organized regular meetings and supervised me particularly in the strategic decisions during the course of my thesis.

In addition, I would like to express my appreciation to all members of the NA61 collaboration, who have helped me with fruitful discussions and advice in numerous meetings and private communications.

I would also like to gratefully acknowledge the exceptional supervision of Dr. M. Unger, who has guided me closely through the entire process of this thesis. His input and feedback was invaluable to this work. Many helpful discussions also arose together with M. Haug.

Appendix

A. Alternative methods for T2 bias correction

There are at least three plausible methods to correct for the trigger bias of the S4 scintillator:

1. Use of Monte Carlo simulations
2. Extrapolation method (artificially enlarge size of S4 and extrapolate to $r = 0$)
3. Use of trigger sets T1 and T3 (done in this work, see Section 4.5)

Correction with Monte Carlo simulations

Since the S4 is actively simulated in the Monte Carlo sets used in this work, it is of course possible to obtain a precise prediction for the correction of the T2 bias. However such a prediction highly depends on the simulation model. Unlike corrections of tracks, which are done differentially in small bins of phase space, the loss by T2 events is a phenomenon on global event level. It explicitly depends on properties of the event, such as multiplicity and particle distributions in θ, ϕ and p. Furthermore it depends on the physics simulated by the transport code and secondary generator like secondary interactions and feed down (decay).

The simulation sets used in this work are production events. Table A.1 shows the prediction of the efficiency of T2 events for the case of production events. This means, a fraction of (1 - efficiency) of the production events is not recorded in the T2 data set. As one can see, the models predict significantly different efficiencies of T2. Assuming that the differences between models are similarly large for differential correction of the T2 bias in individual bins in phase space, the model correction would come along with a large systematic uncertainty on the results.

It appears that the predictions from Monte Carlo simulations are not very well reproducing the measurement, compare Fig. A.1. In some regions of phase space, a bias of several per cent would result from a T2 correction by means of Monte Carlo simulations. Due to

Model	158 GeV/c	350 GeV/c
VENUS	87.94 %	71.36 %
EPOS	91.36 %	78.60 %

Table A.1.: Predicted T2 efficiency for $\pi^- + \mathrm{C}$ interactions.

the high dependency on event topology, it sounds plausible that Monte Carlo simulations fail to describe such a trigger bias with sufficient accuracy.

Correction with extrapolation method

The extrapolation method has been used in two recent NA49 papers, [45] and [18]. The latter deals with p + C collisions at 158 GeV/c beam momentum which is a reaction very comparable to those studied in this work.

Fig. A.1 demonstrates the extrapolation method for a selection of (relatively large) bins in p and p_T for 350 GeV/c beam momentum. In addition to T2 data, the unbiased data is plotted. Monte Carlo predictions for T2 and for unbiased production events are shown as well.

The extrapolation method works on offline data and takes advantage of an imaginary counter, similar to S4 but enlarged in size. The precise workflow of the extrapolation method is the following:

1. Define a new event trigger (here called *enlarged S4*); its fiducial volume has the shape of a circular disk centered at the exact position of S4.
2. The radius, or solid angle of this new trigger can now be varied at will.
3. The enlarged S4 shall fire a trigger signal if any charged track has traversed its fiducial disk. To achieve this, it is necessary to track all reconstructed tracks (including GTPC-only tracks) through the magnetic field to the z-position of S4 and calculate its distance to the center of S4.
4. With increasing solid angle of the enlarged T2, more and more events are removed from a given data set.
5. Plot the number of tracks in individual momentum bins, i.e. (p,p_T), versus solid angle (or radius) of the enlarged S4. For T2 data, only information for radii larger than 1 cm is available, since the radius of S4 is 1 cm. The number of particles will be flat in the region $r < 1$ cm.
6. Fit a straight line (or another function) to the data points in the range from $r_{low} =$ 1 cm to a value $r_{high} > 1$ cm.
7. Extrapolate the fitted curve to $r = 0$ and obtain the corrected number of tracks for the bin in question.

Fig. A.1 shows the application of the extrapolation method for 350 GeV/c data. The y-axis refers to the number of tracks in a particular bin.

B. Smoothing, interpolation, and extrapolation of plots

Where applicable, data points are smoothed, interpolated and extrapolated according to the methods explained in the following.

Smoothing

To remove high frequency fluctuations, or "wiggles" in one dimensional plots, the ROOT[46] helper class `TGraphSmooth` is used. More specifically, the implementation `SmoothSuper` with default arguments `bass = 0` and `span = 0` is used for smoothing, see [47] and [48] for more details.

Interpolation and extrapolation within a p_T bin

Within a p_T, such as in Fig. 4.8, it may happen that some of the original data histograms do not have entries in all bins of p. But since there is a combination (e.g. calculation of quadratic sum) of all different contributions done, an estimator is needed for missing data points. This is done with the ROOT implementation `TGraph::Eval` at default settings. It interpolates points in the graph using a linear interpolation between the two closest points. For points outside the range of the graph, a linear extrapolation is used.

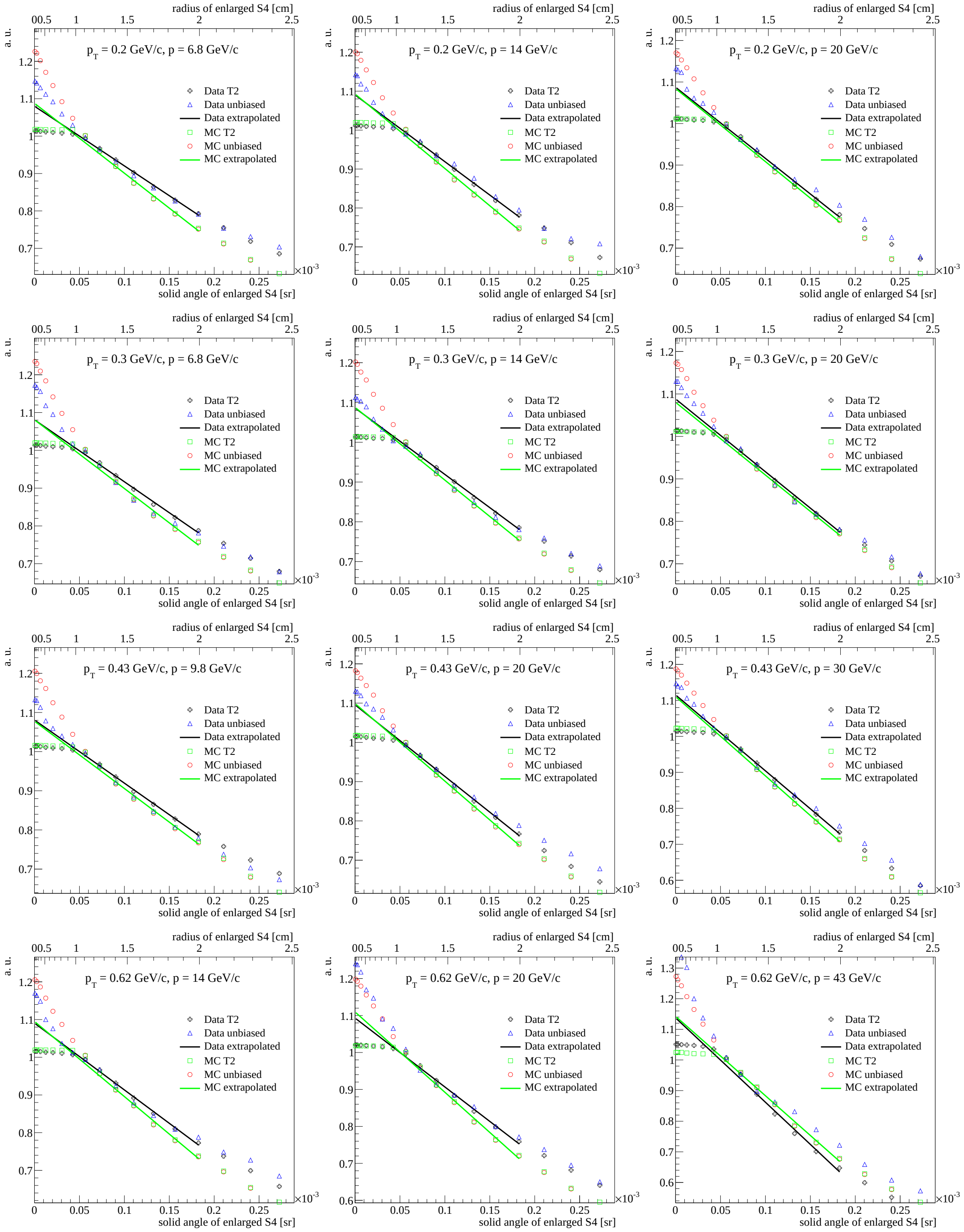

Figure A.1.: Extrapolation method for 350 GeV/c data. Various bins in p and p_T are shown. Y-axis refers to number of tracks in arbitrary units. The T2 sets of data and Monte Carlo have been fitted with a linear function $f(\Omega)$ in the range from $\Omega_{low} = 6 \cdot 10^{-5}$ to $\Omega_{low} = 1.8 \cdot 10^{-4}$ and extrapolated to $\Omega = 0$.

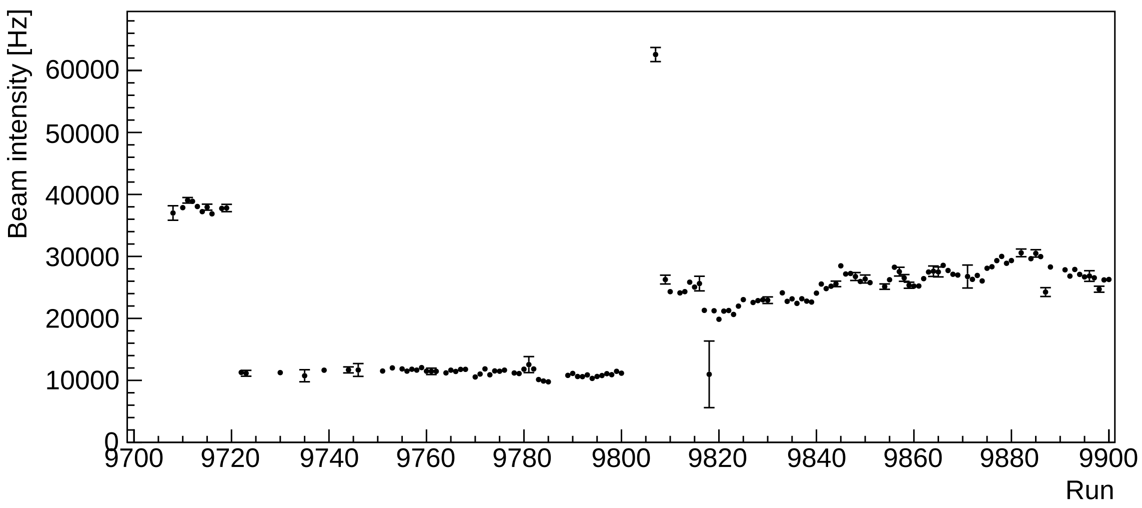

Figure C.2.: Beam intensity for $\pi^- + \mathrm{C}$ runs at 350GeV/c. Values are calculated from WFA information and represent an average beam intensity during a spill. Clearly visible, the beam intensity has changed around run 9720 (beam retune) and run 9800 (change of beam momentum).

Extrapolation to larger p_T bins

In graphs similar to Fig. 4.8, it may occur that some of the original histograms do not have entries in high p_T bins. In order to be able to give an estimate nevertheless, the maximum value of the next lower p_T bin is taken for all p bins of the unoccupied p_T bin.

C. Beam intensity and limited resolution of the WFA

The resolution of the WFA is limited in a manner that two particles, that are very close to each other in time, are counted as one. The WFA information in the framework has a bin size of 100 ns, which corresponds to its resolution. For the following calculation, it will be assumed that two beam particles can be identified as two individuals if they are separated by more than 100 ns in time. If the separation is less than 100 ns, the two particles will be counted as one. The probability of this occurrence can easily be calculated with Poisson statistics.

The probability of exactly k particles in an interval ΔT is given by the Poisson distribution

$$P(k) = \frac{\lambda^k e^{-\lambda}}{k!} \tag{C.1}$$

with λ being the expected number of beam particles per time interval. For a time interval $\Delta T = 100$ ns and a beam intensity of $I \approx 40kHz$ (see Fig. C.2), it holds $\lambda = I \cdot \Delta t \approx 40000Hz \cdot 100\text{ ns} = 0.004$.

The probability for one or more additional particles ($k \geq 1$) within 100 ns is $P(\geq 1) \approx 0.4\%$. Given an interaction probability of 3%, the probability of two interactions within a 100 ns interval is $P(\geq 1) \approx 0.012\%$. Thus the effect on the multiplicity can be neglected.

D. ToF efficiency at full magnetic field

The ToFs measure the time of a hit in the scintillator array behind the MTPC. Together with the time of the trigger, a time interval is measured. As the momentum of particles increases, their velocity approaches the speed of light. Thus making it increasingly difficult to measure its dependence of the mass.

As a general statement it can be said, the ToF information for mass measurement is only useful for particles with a momentum $p \lesssim 12$ GeV/c. The runs used in this work are

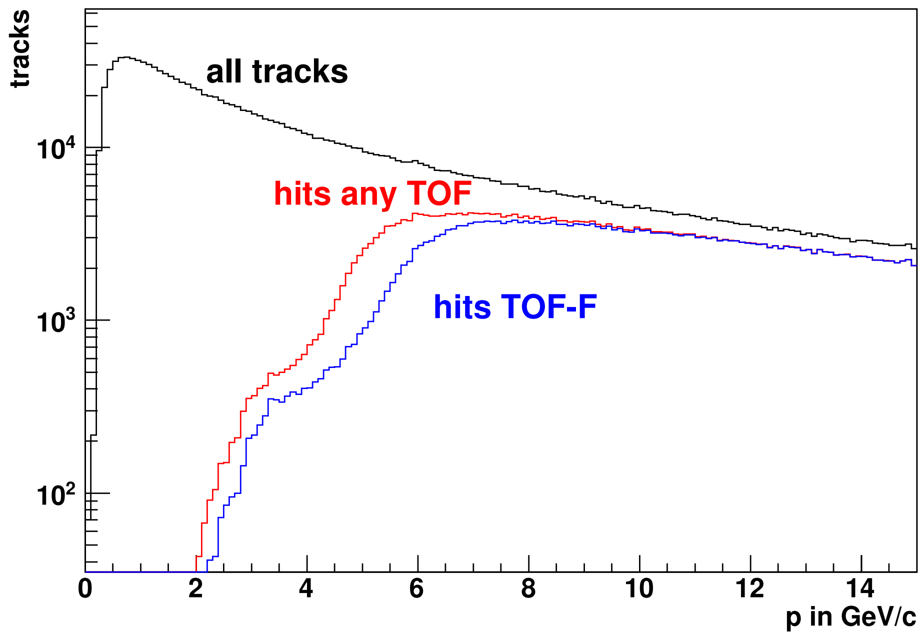

Figure D.3.: ToF efficiency at full magnetic field. The black curve shows all reconstructed tracks. Red shows reconstructed tracks with a hit in any of the ToFs. The blue curve shows reconstructed tracks with a hit in ToF-F. Plot made from 158 GeV/c $\pi^- + \mathrm{C}$ data set with non-perfect ToF calibrations.

Table E.2.: Reconstruction releases and versions of $\overline{\text{Off}}\underline{\text{line}}$ used for DS2SHOE conversion of all data sets used in this analysis.

Type	p [GeV/c]	Rec. tag	Date of rec.	$\overline{\text{Off}}\underline{\text{line}}$ version
Data	350	09J	Oct 8, 2011	trunk 5162
Data	158	09K	Nov 1, 2011	v0r1p0
MC (VENUS)	350	09J	Dec 27, 2011	v0r1p0
MC (VENUS)	158	09J	Dec 25, 2011	v0r1p0
MC (EPOS)	350	09J	Feb 12, 2012	trunk 5234
MC (EPOS)	158	09J	Feb 08, 2012	trunk 5234

performed at full magnetic field, thus low energetic tracks are bend thoroughly away from the beam axis. As a consequence, very little tracks with $p \lesssim 12$ GeV/c reach the ToFs, which are located at the far end of the detector. A qualitative study on the ToF efficiency has been performed on the data set of π^-+C at 158 GeV/c, see Fig. D.3.

E. Software and reconstruction releases

Table E.2 lists the versions of the reconstruction and $\overline{\text{Off}}\underline{\text{line}}$ that were used to create data files in the SHOE[2] format.

The software used to run the analysis scripts on SHOE files is ROOT 5.30/01 and $\overline{\text{Off}}\underline{\text{line}}$ trunk 5453.

F. Selection of simulated tracks for acceptance study

For the acceptance study the following selection of simulated tracks is applied. A simulated track is selected if the charged particle

- is a proton or antiproton

[2]SHOE is a file format containing all reconstructed information needed for analysis

- is a pion with $p > 1$ GeV/c
- does not decay at all
- does decay outside of a manually defined volume.*

* holds if the following code snippet returns true:

```
const evt::sim::Vertex& stopVertex =
   simEvent.Get<evt::sim::Vertex>(simVtxTrack.GetStopVertexId());
if (stopVertex.GetPosition().GetX() > +400*cm
    || stopVertex.GetPosition().GetX() < -400*cm
    || stopVertex.GetPosition().GetZ() > 740*cm
    || stopVertex.GetPosition().GetY() < -60*cm
    || stopVertex.GetPosition().GetY() > 60*cm
    || (stopVertex.GetPosition().GetX() > 100*cm
        && stopVertex.GetPosition().GetZ() < 0*cm)
    || (stopVertex.GetPosition().GetX() < -100*cm
        && stopVertex.GetPosition().GetZ() < 0*cm)
   )
return true;
```

G. Additional tables and figures

Table G.3.: Paramters of fit of T2 bias correction with uncertainties estimated from the fit procedure.

p [GeV/c]	Tracks	c_0	c_1	c_2	c_3
158	h^-	0.95±0.003	-0.014±0.009	0.0066±0.003	0.016±0.008
	h^+	0.96±0.003	-0.022±0.009	-0.0043±0.003	0.03±0.008
350	h^-	0.87±0.003	-0.059±0.009	0.016±0.003	0.047±0.007
	h^+	0.88±0.003	-0.056±0.009	-0.011±0.003	0.062±0.007

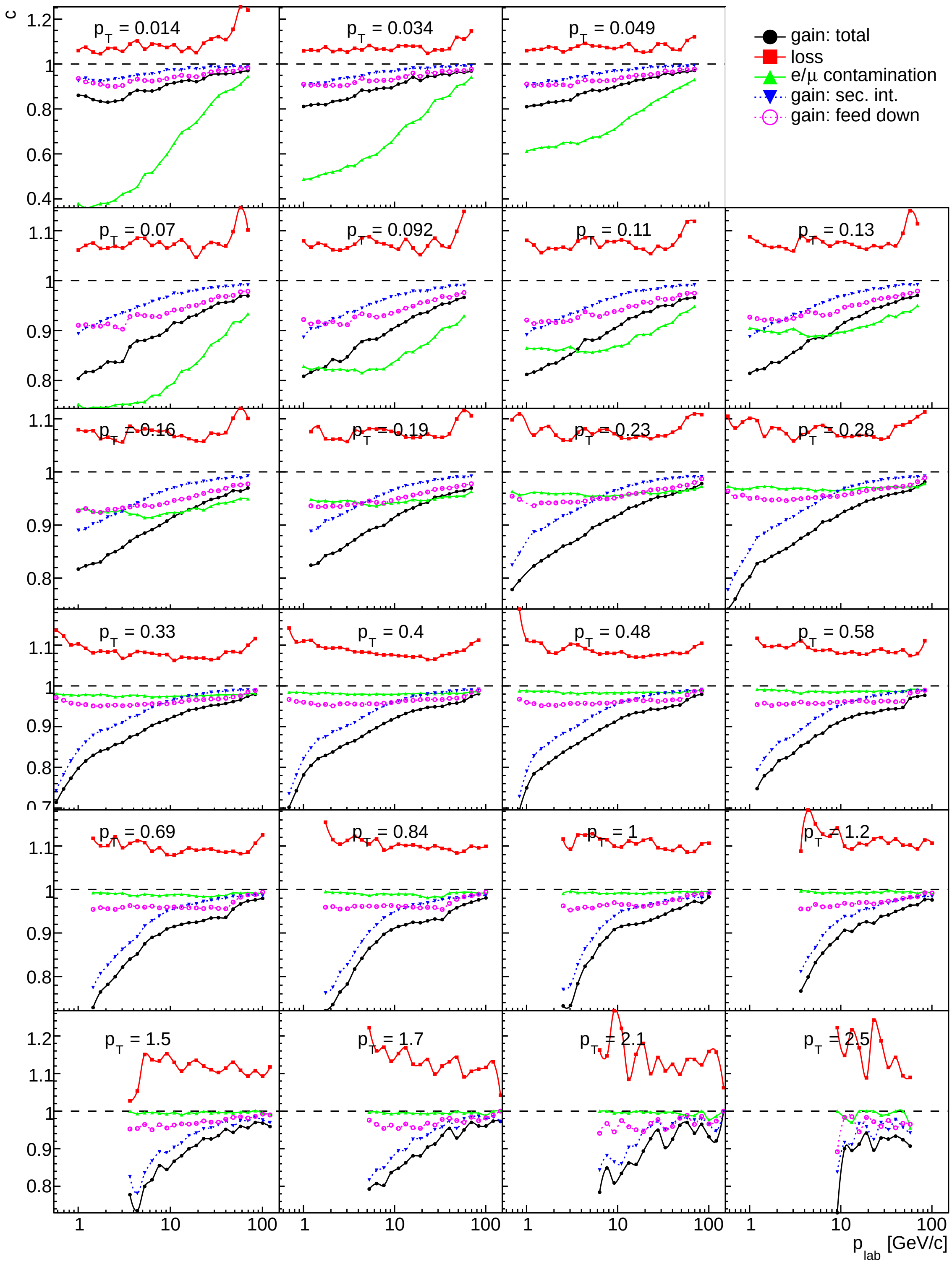

Figure G.4.: Breakdown of the correction factor for positively charged hadrons obtained from EPOS Monte Carlo simulations for 350 GeV/c. Transverse momentum p_T is given in GeV/c.

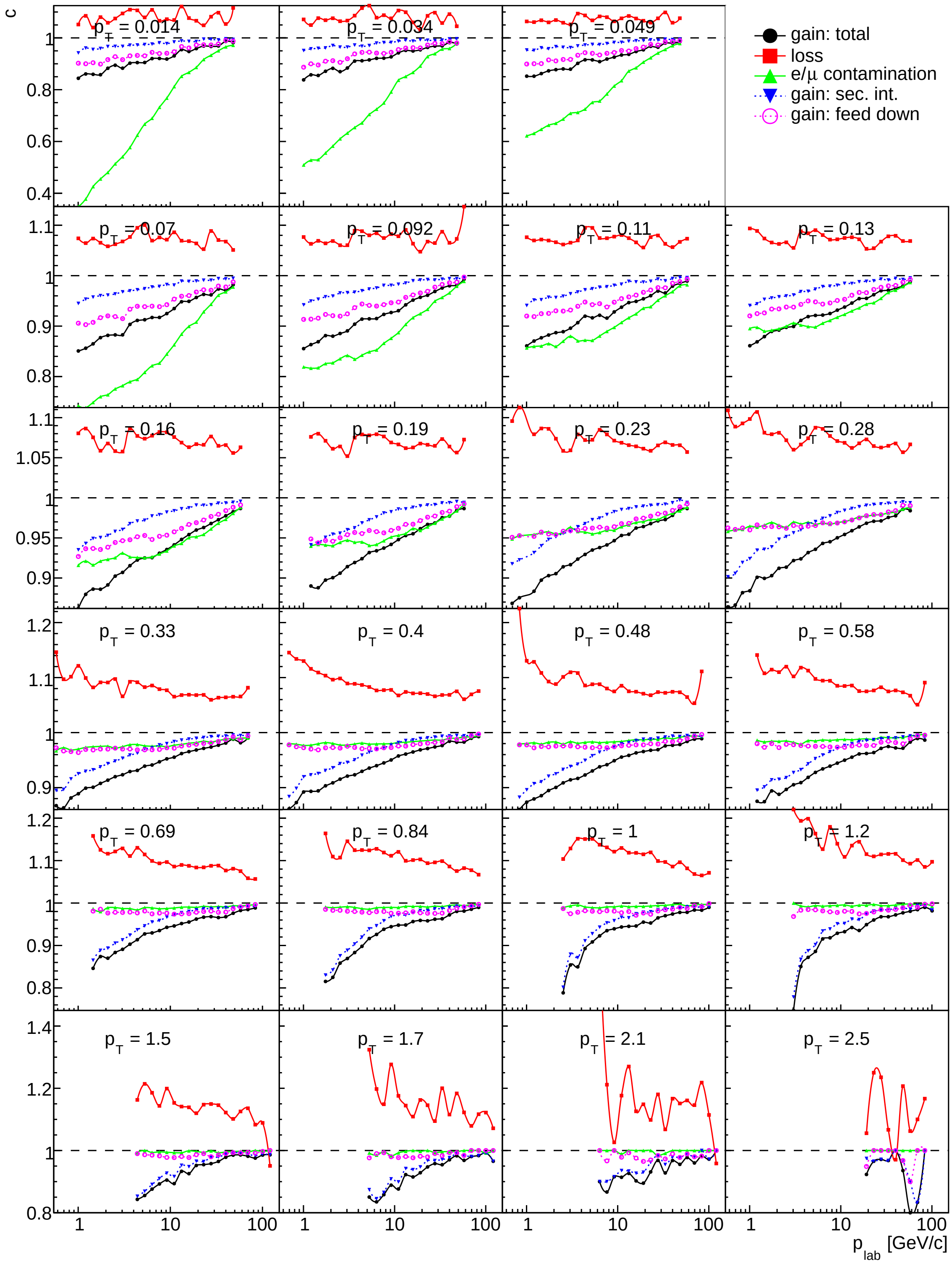

Figure G.5.: Breakdown of the correction factor for negatively charged hadrons obtained from EPOS Monte Carlo simulations for 158 GeV/c. Transverse momentum p_T is given in GeV/c.

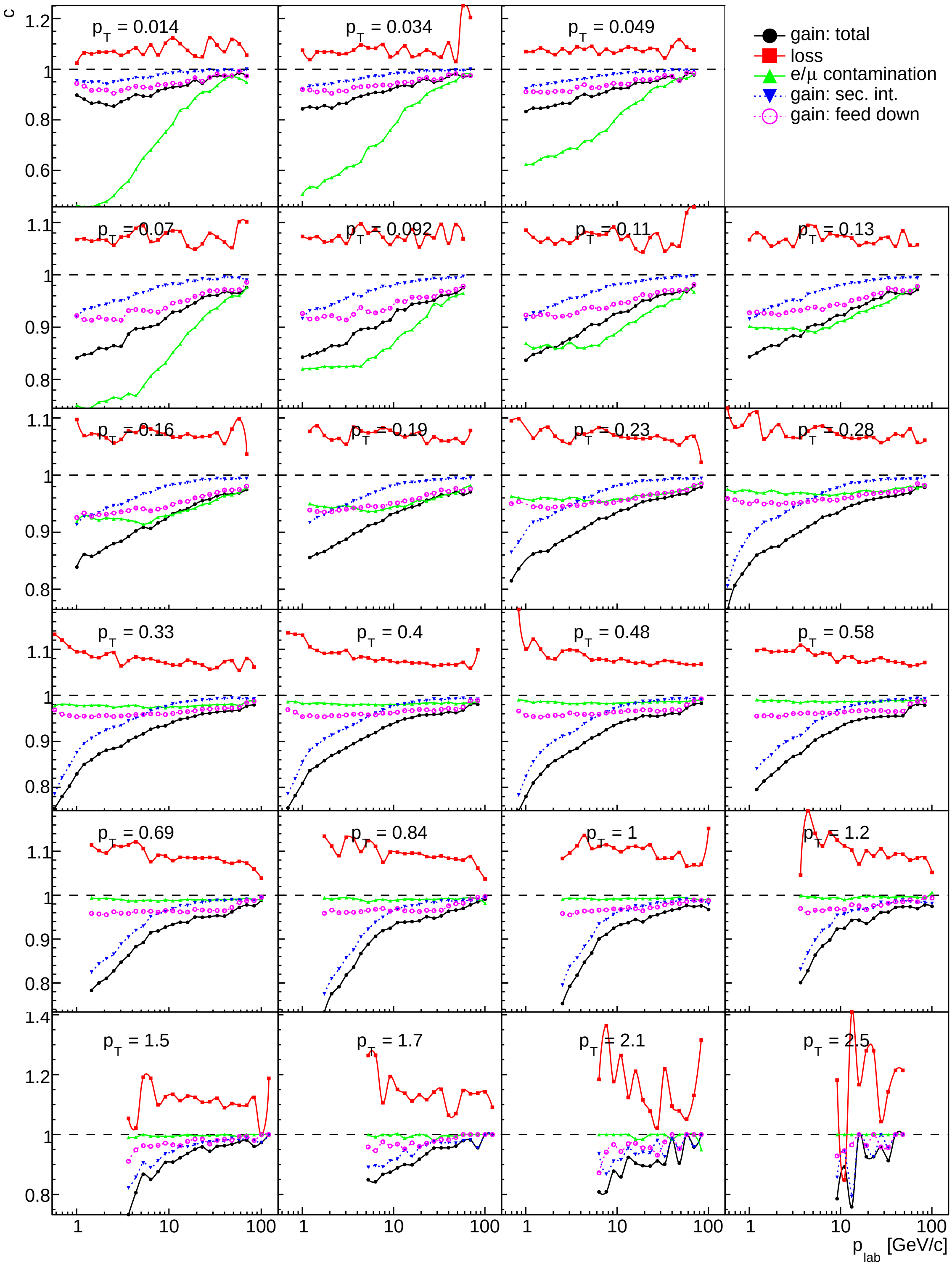

Figure G.6.: Breakdown of the correction factor for positively charged hadrons obtained from EPOS Monte Carlo simulations for 158 GeV/c. Transverse momentum p_T is given in GeV/c.

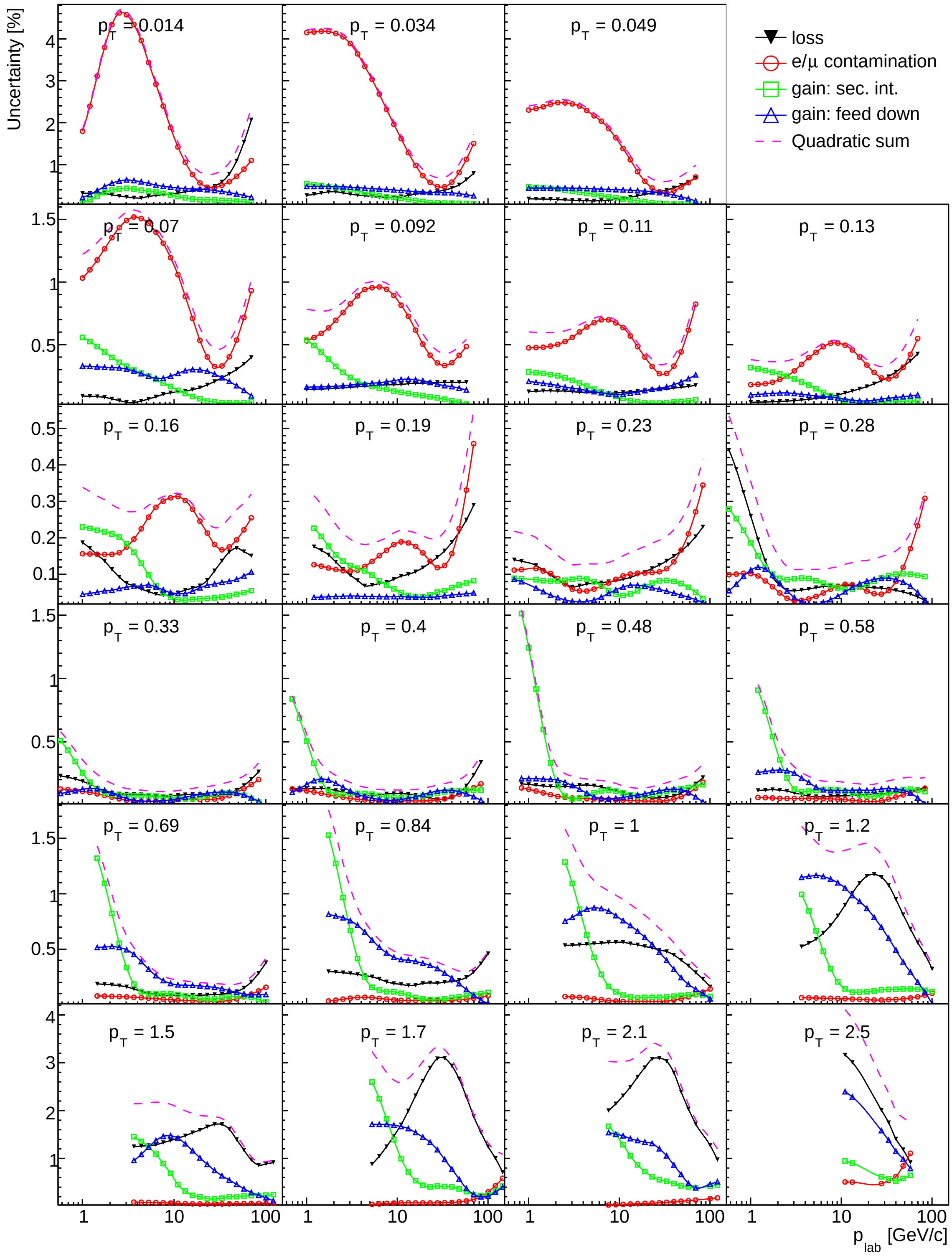

Figure G.7.: Calculation of the model uncertainty of MC correction for h^+ at 350 GeV/c. The individual components are discussed in Section 4.7. Transverse momentum p_T is given in GeV/c.

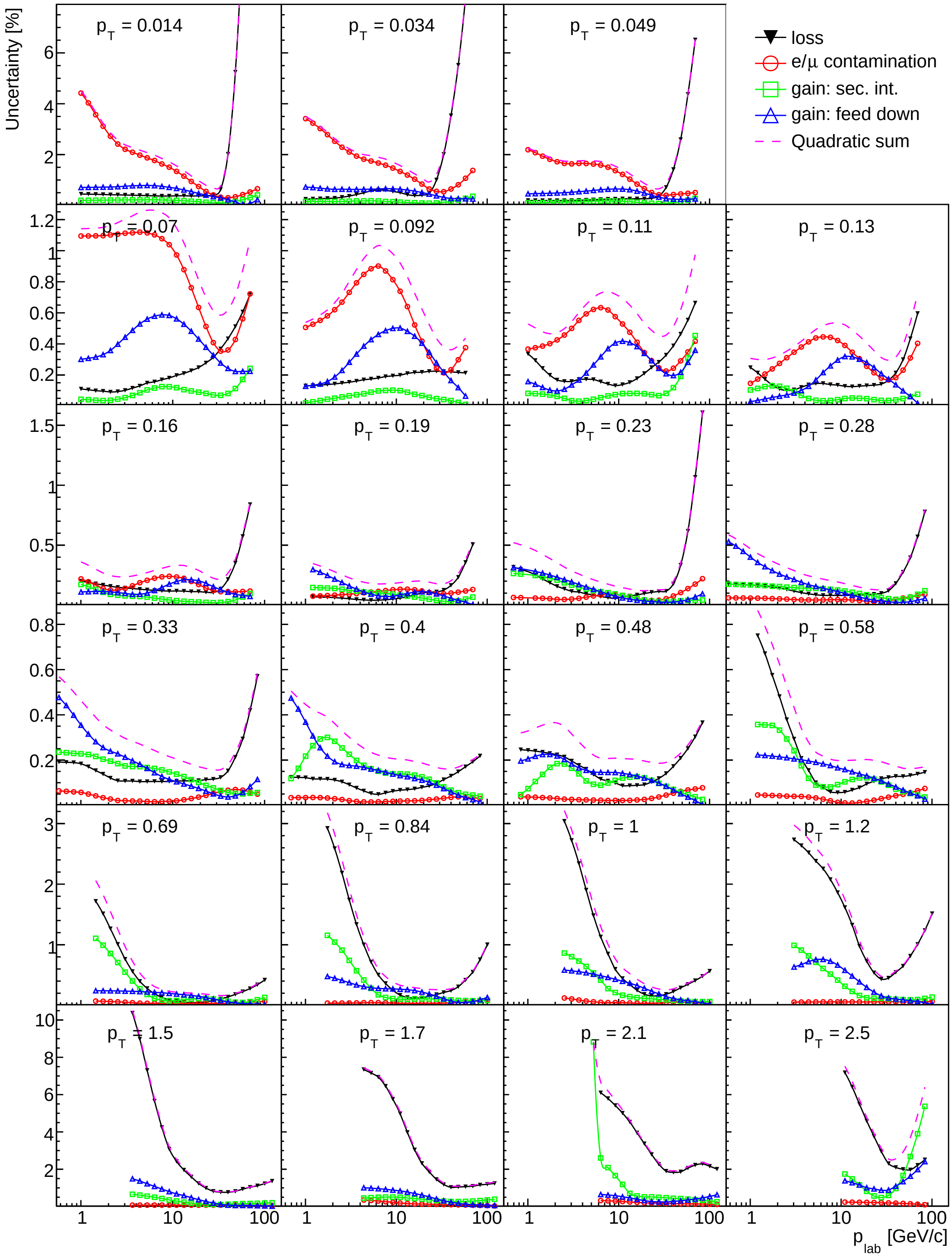

Figure G.8.: Calculation of the model uncertainty of MC correction for h^- at 158 GeV/c. The individual components are discussed in Section 4.7. Transverse momentum p_T is given in GeV/c.

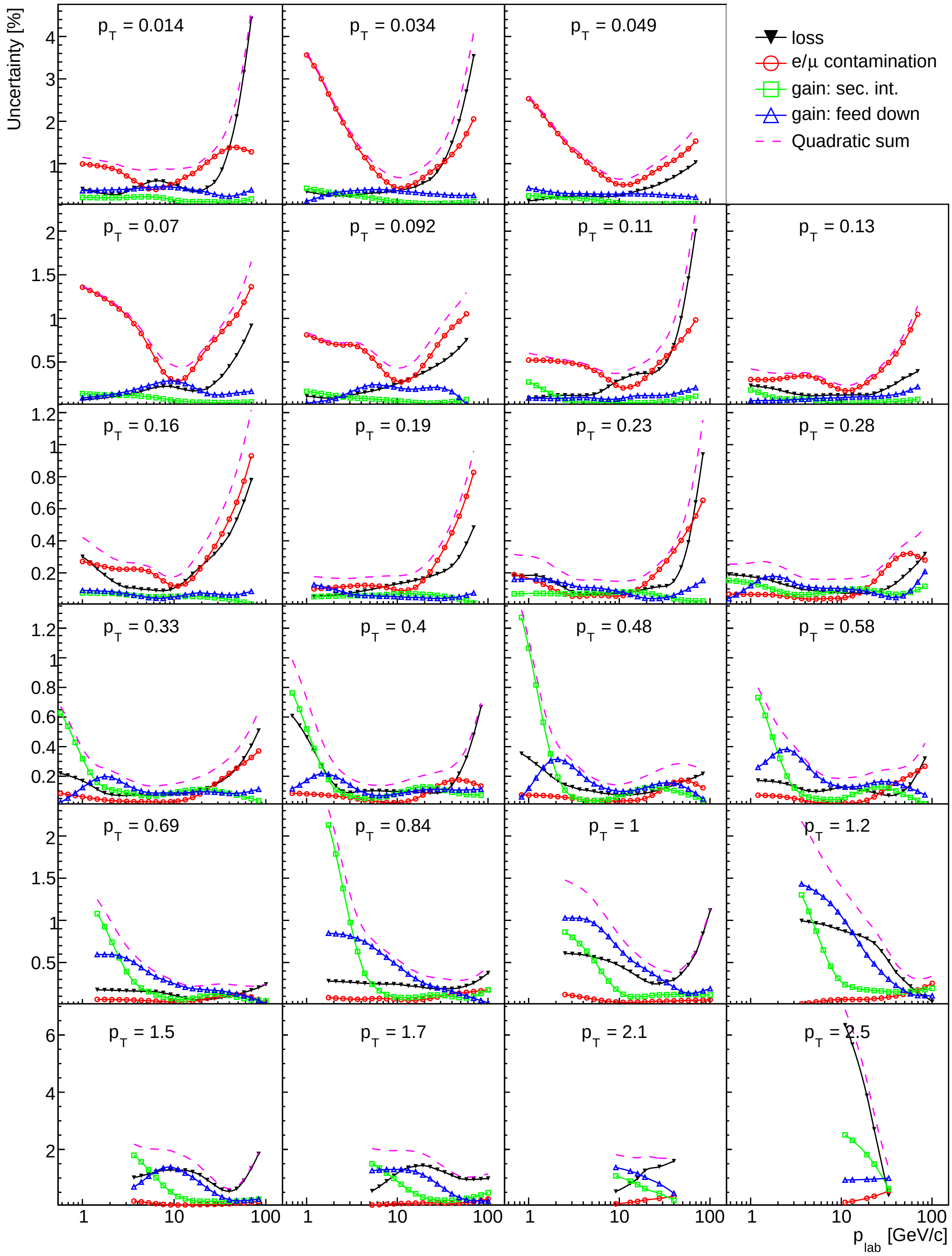

Figure G.9.: Calculation of the model uncertainty of MC correction for h^+ at 158 GeV/c. The individual components are discussed in Section 4.7. Transverse momentum p_T is given in GeV/c.

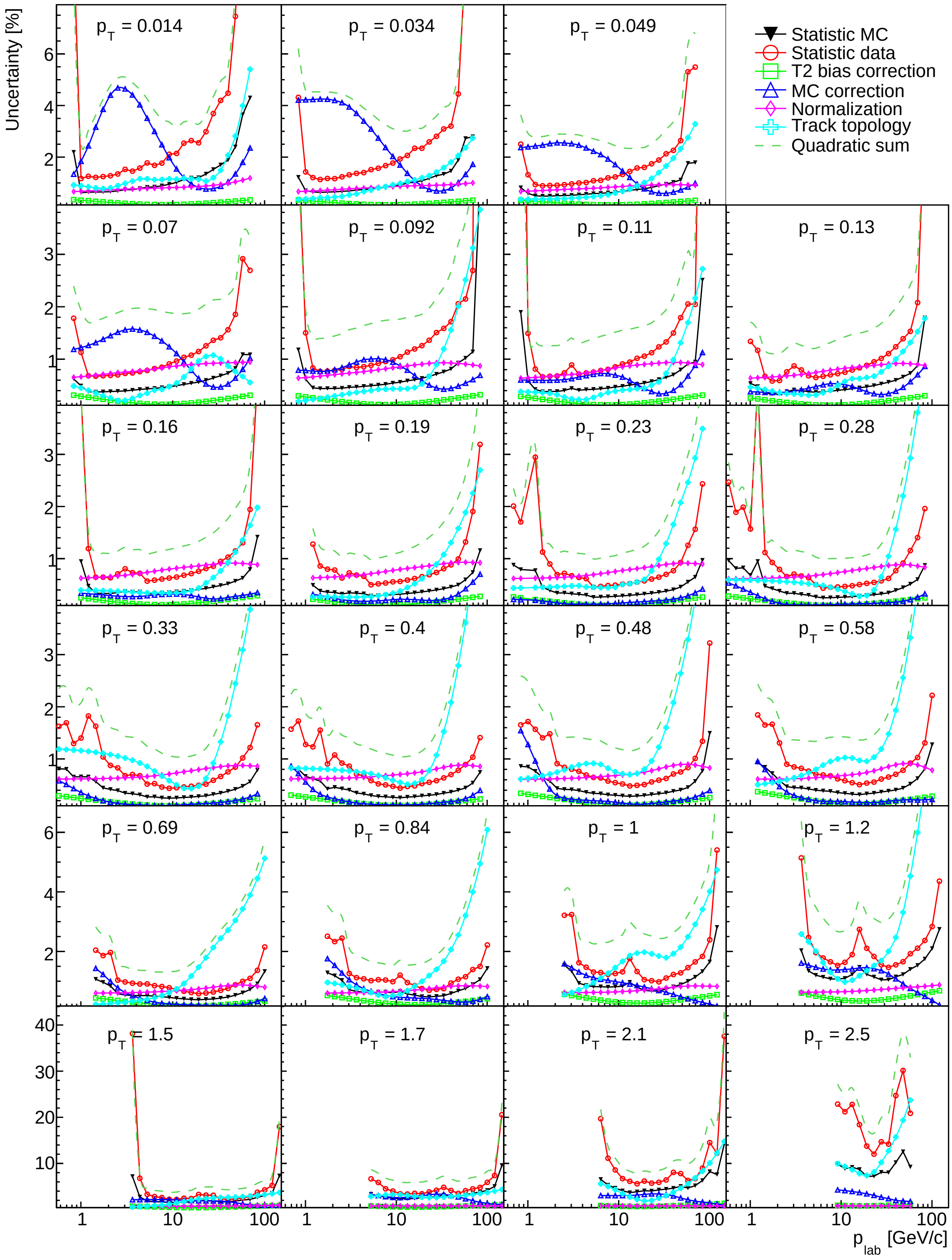

Figure G.10.: Calculation of the total uncertainty for h^+ at 350 GeV/c. The individual components are discussed in Section 4.7. Transverse momentum p_T is given in GeV/c.

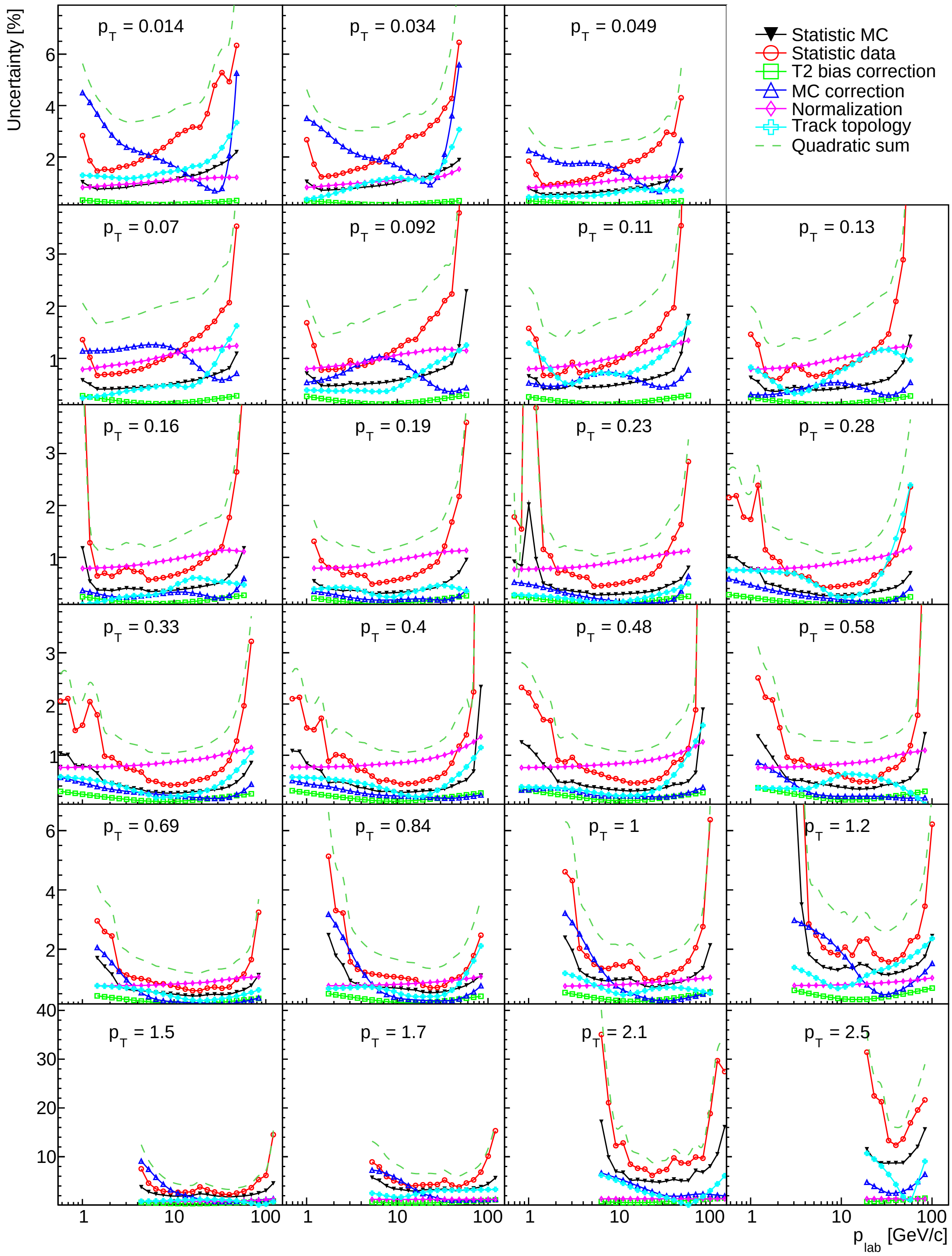

Figure G.11.: Calculation of the total uncertainty for h^- at 158 GeV/c. The individual components are discussed in Section 4.7. Transverse momentum p_T is given in GeV/c.

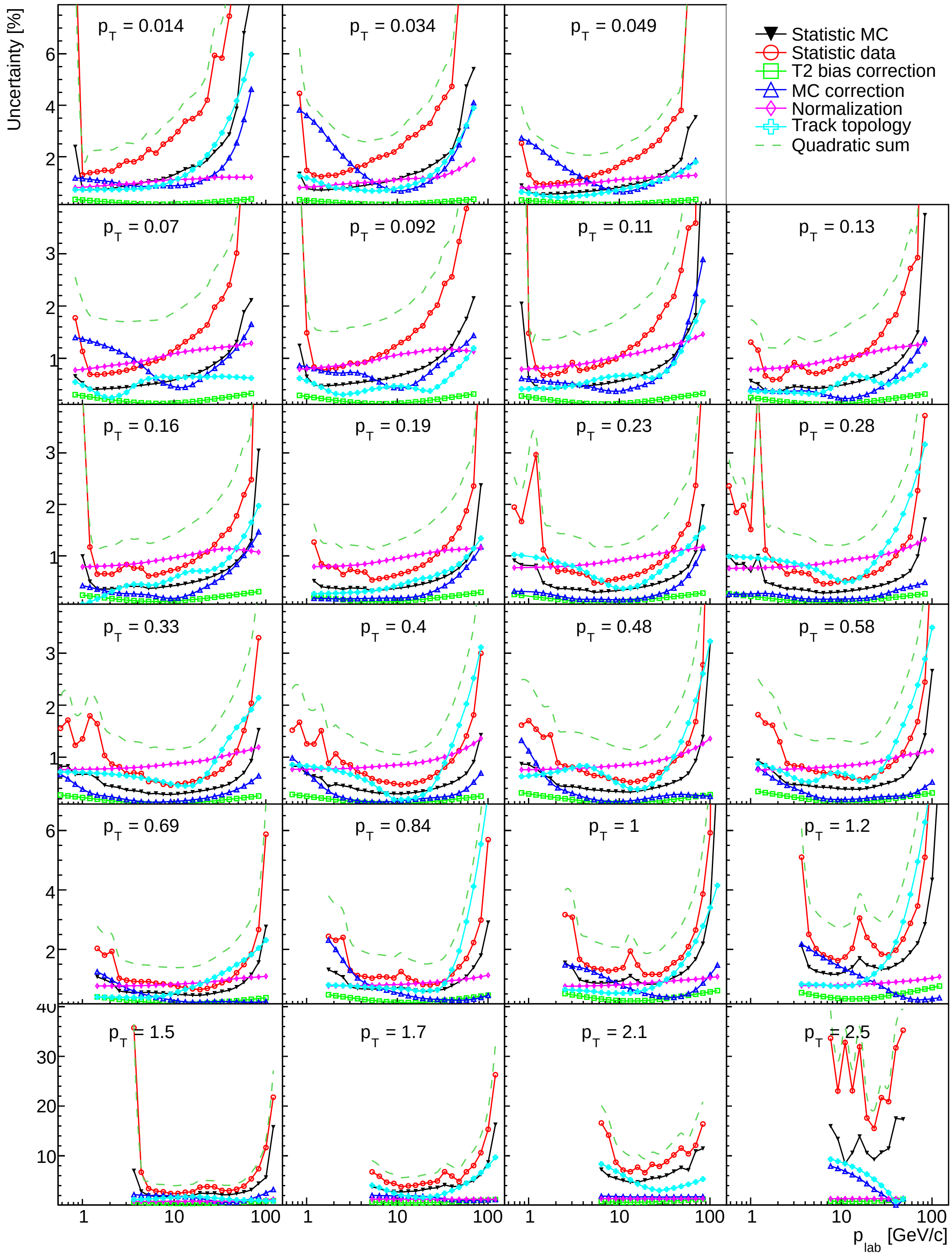

Figure G.12.: Calculation of the total uncertainty for h^+ at 158 GeV/c. The individual components are discussed in Section 4.7. Transverse momentum p_T is given in GeV/c.

H. Tabulated results

Table H.4.: Complete table of results of differential inclusive cross section $F = \frac{\Delta\sigma}{\Delta p_T \Delta p_{lab}}$ for negatively and positively charged hadrons in $\pi^- + \mathrm{C}$ interactions at 158 GeV/c and 350 GeV/c beam momentum. F is given in $\frac{\mathrm{mb}}{(\mathrm{GeV}/c)^2}$. σ_{stat} and σ_{sys} denote relative statistical and systematic uncertainty respectively.

Bin size				158 GeV/c, h^-			158 GeV/c, h^+			350 GeV/c, h^-			350 GeV/c, h^+		
$\log \frac{p_T}{\mathrm{GeV}/c}$		$\log \frac{p}{\mathrm{GeV}/c}$		F	σ_{stat}	σ_{sys}	F	σ_{stat}	σ_{sys}	F	σ_{stat}	σ_{sys}	F	σ_{stat}	σ_{sys}
low	high	low	high		%	%		%	%		%	%		%	%
-inf	-1.56	-0.12	-0.04				46.2	10.7	2.9				50.7	10.3	2.5
		-0.04	0.04	34.8	2.8	4.9	35.6	1.3	1.8	39.5	2.6	7	41.9	1.2	2.3
		0.04	0.12	30.7	1.9	4.5	29.5	1.4	1.8	34.8	1.7	6.7	35.1	1.3	2.8
		0.12	0.2	24.6	1.5	4.1	23.7	1.4	1.7	29.5	1.3	6.5	29.9	1.2	3.4
		0.2	0.28	21	1.5	3.7	18.6	1.5	1.7	24.5	1.3	6.2	24.1	1.2	4.1
		0.28	0.36	16.9	1.5	3.3	15.3	1.4	1.7	20.9	1.3	5.9	19.4	1.3	4.6
		0.36	0.44	14	1.6	3.1	11.6	1.7	1.7	17.1	1.4	5.6	16	1.3	4.9
		0.44	0.52	10.7	1.6	2.9	8.98	1.8	1.8	13.9	1.4	5.2	12.5	1.5	4.9
		0.52	0.6	8.67	1.7	2.9	7.1	1.8	1.8	10.8	1.5	4.9	9.83	1.5	4.7
		0.6	0.68	6.54	1.9	2.8	5.61	2	1.8	8.71	1.5	4.5	7.75	1.6	4.3
		0.68	0.76	4.86	2	2.8	4.08	2.3	1.9	6.67	1.6	4.2	5.69	1.8	3.9
		0.76	0.84	3.89	2.2	2.8	3.29	2.1	1.9	5.33	1.7	3.9	4.92	1.7	3.4
		0.84	0.92	2.86	2.4	2.8	2.45	2.5	2	4.36	1.7	3.6	3.9	1.8	3
		0.92	1	2.26	2.6	2.7	1.91	2.7	2.1	3.39	1.9	3.3	2.76	2.1	2.6
		1	1.08	1.68	2.9	2.7	1.41	3	2.3	2.55	2.2	3	2.24	2.1	2.3
		1.08	1.16	1.23	3	2.7	1.03	3.4	2.5	1.95	2.3	2.9	1.61	2.5	2.2
		1.16	1.24	0.921	3.2	2.6	0.791	3.5	2.7	1.45	2.4	2.7	1.26	2.6	2.1
		1.24	1.32	0.738	3.2	2.6	0.562	3.7	2.9	1.15	2.5	2.6	0.977	2.6	2.1
		1.32	1.4	0.507	3.7	2.7	0.374	4.2	3.3	0.83	2.9	2.5	0.711	3	2.1
		1.4	1.48	0.334	4.8	2.9	0.251	5.9	3.8	0.586	3.4	2.7	0.523	3.7	2.3
		1.48	1.56	0.226	5.3	3.3	0.17	5.8	4.3	0.457	3.5	2.9	0.389	4.2	2.6
		1.56	1.64	0.187	4.9	4.2	0.112	7.5	5.1	0.345	3.7	3.2	0.294	4.5	3.2
		1.64	1.72	0.119	6.3	6.7	0.0826	9.6	6.4	0.258	4.4	3.7	0.184	7.5	4.1
		1.72	1.8				0.048	20.2	9.2				0.135	13.7	5.8
		1.8	1.88				0.0235	27	11.3				0.0754	16.5	7.4
-1.56	-1.4	-0.12	-0.04				120	4.5	4.3				125	4.3	1.5
		-0.04	0.04	97.7	2.7	3.8	98.8	1.5	4	103	2.6	4.2	109	1.4	4.4
		0.04	0.12	81.5	1.7	3.6	79.6	1.3	3.7	89.7	1.7	4.2	91.4	1.2	4.4
		0.12	0.2	69.5	1.2	3.3	65.8	1.2	3.4	77.8	1.2	4.2	79.1	1.1	4.4
		0.2	0.28	58.5	1.3	3.1	52.7	1.3	3.1	64.8	1.2	4.2	64.2	1.2	4.4
		0.28	0.36	46.7	1.3	2.9	42.9	1.3	2.8	55	1.2	4.1	54.1	1.2	4.3
		0.36	0.44	37.6	1.4	2.8	33.8	1.4	2.5	47.9	1.2	4	43.4	1.2	4.3
		0.44	0.52	30.4	1.5	2.7	26.7	1.5	2.3	37.2	1.3	3.8	35.1	1.3	4.1
		0.52	0.6	23.4	1.5	2.6	20.1	1.6	2.1	30.9	1.3	3.7	26.7	1.4	3.9
		0.6	0.68	18.9	1.6	2.6	15.8	1.7	2	25.1	1.3	3.5	21.3	1.4	3.6
		0.68	0.76	14.2	1.8	2.6	11.5	1.9	1.9	18.5	1.5	3.3	16.4	1.5	3.4
		0.76	0.84	11.1	1.8	2.6	9.28	2	1.8	15.7	1.5	3.2	13	1.6	3.1
		0.84	0.92	8.29	2	2.6	7.16	2.1	1.8	12.3	1.5	3.1	10.5	1.7	2.8
		0.92	1	6.2	2.2	2.5	5.34	2.2	1.9	9.73	1.6	3	7.98	1.8	2.5
		1	1.08	4.71	2.4	2.5	3.95	2.4	1.9	7.37	1.8	2.9	5.96	1.9	2.3
		1.08	1.16	3.29	2.8	2.4	2.97	2.7	2.1	5.4	2	2.8	4.71	2.1	2.2
		1.16	1.24	2.6	2.8	2.3	2.14	2.9	2.2	3.97	2.1	2.7	3.31	2.3	2.1
		1.24	1.32	1.94	2.9	2.3	1.56	3.1	2.4	3.1	2.2	2.5	2.64	2.3	2.1
		1.32	1.4	1.39	3.2	2.3	1.16	3.3	2.6	2.3	2.4	2.4	1.92	2.6	2.1
		1.4	1.48	1.03	3.4	2.6	0.743	3.9	2.9	1.64	2.7	2.3	1.43	2.8	2.2
		1.48	1.56	0.653	3.9	3.4	0.52	4.3	3.4	1.21	3	2.2	1.02	3.1	2.4
		1.56	1.64	0.525	4.3	4.8	0.332	4.7	4	1.02	2.9	2.1	0.783	3.2	2.6
		1.64	1.72	0.286	6.5	6.8	0.182	8.3	5	0.735	3.3	2.3	0.603	4.4	3.1
		1.72	1.8				0.117	14.9	6.8				0.353	9.7	4
		1.8	1.88				0.0693	15.1	8.1				0.252	8.4	4.4
-1.4	-1.24	-0.12	-0.04				166	2.5	3.1				174	2.5	1.2
		-0.04	0.04	138	1.8	2.6	141	1.3	2.9	143	1.9	2.6	148	1.3	2.6
		0.04	0.12	115	1.3	2.4	112	1	2.7	125	1.3	2.6	127	0.9	2.6
		0.12	0.2	99.4	0.9	2.3	92.7	0.9	2.5	107	0.9	2.7	106	0.9	2.7
		0.2	0.28	82.2	0.9	2.2	76.4	0.9	2.3	92.6	0.9	2.8	88.7	0.9	2.7
		0.28	0.36	67.3	1	2.1	60.8	1	2.1	75.9	0.9	2.8	74.3	0.9	2.7
		0.36	0.44	55.3	1	2.1	49.9	1	2	65.5	0.9	2.8	60.9	0.9	2.7
		0.44	0.52	44.1	1	2.1	38.5	1.1	1.8	54.1	0.9	2.8	49.5	1	2.7
		0.52	0.6	34.5	1.1	2.1	29.4	1.1	1.8	42.8	1	2.8	39	1	2.7
		0.6	0.68	27	1.1	2.2	23.3	1.2	1.7	36.1	1	2.7	31.7	1	2.6
		0.68	0.76	21.3	1.2	2.2	17.1	1.3	1.6	28.5	1	2.6	24.8	1.1	2.5
		0.76	0.84	15.7	1.3	2.2	13.4	1.4	1.6	22.5	1.1	2.6	20.1	1.1	2.4
		0.84	0.92	11.9	1.4	2.2	10.2	1.4	1.6	17.9	1.1	2.5	15.3	1.2	2.3
		0.92	1	9.08	1.5	2.1	7.65	1.6	1.7	14.2	1.2	2.4	12	1.2	2.1
		1	1.08	6.75	1.7	2.1	5.53	1.8	1.7	10.9	1.3	2.4	9.11	1.3	2
		1.08	1.16	4.99	1.8	2	4.19	1.9	1.8	8.05	1.3	2.3	6.83	1.4	1.8
		1.16	1.24	3.75	1.9	1.9	3.09	2	1.9	5.98	1.5	2.3	5.04	1.6	1.8
		1.24	1.32	2.81	2.1	1.8	2.23	2.2	2	4.63	1.5	2.2	3.9	1.6	1.8
		1.32	1.4	2.02	2.3	1.8	1.58	2.4	2.2	3.39	1.7	2.2	2.97	1.7	1.8
		1.4	1.48	1.37	2.5	1.8	1.08	2.6	2.3	2.44	1.8	2.1	2.19	1.9	2
		1.48	1.56	0.937	3	2	0.685	3.1	2.5	1.77	2.1	2	1.53	2.1	2.2
		1.56	1.64	0.732	2.9	2.4	0.465	3.5	2.7	1.37	2.1	2.1	1.13	2.3	2.5
		1.64	1.72	0.503	4.3	3.4	0.302	3.8	3.1	1.04	2.2	2.2	0.741	2.6	2.8
		1.72	1.8				0.187	8.8	4.1				0.53	5.3	3.5
		1.8	1.88				0.107	8.9	4.6				0.33	5.5	4
-1.24	-1.08	-0.12	-0.04				221	1.8	1.8				237	1.8	1.1
		-0.04	0.04	185	1.4	1.5	193	1.1	1.8	194	1.4	1.4	206	1.1	1.6
		0.04	0.12	159	1	1.5	160	0.7	1.7	166	1	1.4	175	0.7	1.6
		0.12	0.2	137	0.7	1.5	131	0.7	1.6	146	0.7	1.5	147	0.7	1.6
		0.2	0.28	114	0.7	1.5	108	0.7	1.6	124	0.7	1.6	121	0.7	1.6
		0.28	0.36	95	0.7	1.6	86.3	0.7	1.6	104	0.7	1.6	102	0.7	1.7
		0.36	0.44	79	0.7	1.6	70.5	0.7	1.5	88.8	0.7	1.7	85.2	0.7	1.8
		0.44	0.52	64.2	0.7	1.6	55.5	0.8	1.5	73.6	0.7	1.8	67.5	0.7	1.8
		0.52	0.6	49.8	0.8	1.6	42.6	0.8	1.5	60.1	0.7	1.8	54.5	0.7	1.8

Continued on next page

Table H.4 – Continued from previous page

Bin size				158 GeV/c, h^-			158 GeV/c, h^+			350 GeV/c, h^-			350 GeV/c, h^+		
$\log \frac{p_T}{\mathrm{GeV}/c}$		$\log \frac{p}{\mathrm{GeV}/c}$		F	σ_{stat}	σ_{sys}	F	σ_{stat}	σ_{sys}	F	σ_{stat}	σ_{sys}	F	σ_{stat}	σ_{sys}
low	high	low	high		%	%		%	%		%	%		%	%
		0.6	0.68	39.8	0.8	1.7	34	0.9	1.5	50.5	0.7	1.8	44.8	0.8	1.8
		0.68	0.76	31.1	0.9	1.7	25.6	0.9	1.5	40.1	0.8	1.8	35.6	0.8	1.8
		0.76	0.84	23.5	0.9	1.7	20	1	1.4	33.1	0.8	1.9	28	0.8	1.8
		0.84	0.92	17.8	1	1.8	15.5	1	1.4	26.4	0.8	1.9	22.6	0.8	1.7
		0.92	1	13.4	1.1	1.8	11.3	1.1	1.5	20.3	0.8	1.9	17.3	0.9	1.7
		1	1.08	9.75	1.1	1.7	8.25	1.2	1.5	15.9	0.9	1.9	13.2	1	1.6
		1.08	1.16	7.17	1.3	1.7	6.03	1.3	1.5	11.8	1	1.9	9.87	1	1.6
		1.16	1.24	5.19	1.4	1.7	4.34	1.4	1.6	8.9	1	1.8	7.6	1.1	1.6
		1.24	1.32	3.98	1.4	1.7	3.21	1.5	1.6	6.67	1.1	1.8	5.66	1.1	1.6
		1.32	1.4	2.84	1.6	1.7	2.28	1.6	1.7	4.93	1.2	1.7	4.17	1.3	1.6
		1.4	1.48	2.01	1.7	1.8	1.46	2	1.8	3.48	1.3	1.7	3.1	1.4	1.6
		1.48	1.56	1.41	1.9	1.9	0.994	2.1	1.9	2.64	1.4	1.7	2.3	1.4	1.6
		1.56	1.64	1.01	2.1	2.1	0.65	2.4	2.1	1.93	1.5	1.9	1.63	1.6	1.6
		1.64	1.72	0.68	3.5	2.4	0.402	3	2.3	1.41	1.6	2.2	1.09	1.9	1.6
		1.72	1.8				0.234	5	2.8	1.01	30	4.2	0.738	2.9	1.8
		1.8	1.88				0.145	4.9	3.1				0.492	2.7	1.9
-1.08	-1	-0.12	-0.04				290	4.8	1.8				293	5	1.4
		-0.04	0.04	232	1.7	1.3	238	1.5	1.5	240	1.7	1.3	251	1.5	1.2
		0.04	0.12	195	1.2	1.2	200	0.8	1.4	208	1.3	1.2	216	0.8	1.2
		0.12	0.2	171	0.8	1.2	169	0.8	1.3	182	0.8	1.2	186	0.8	1.2
		0.2	0.28	142	0.8	1.2	133	0.8	1.3	152	0.8	1.2	153	0.8	1.2
		0.28	0.36	119	0.8	1.3	110	0.8	1.3	129	0.8	1.2	128	0.8	1.2
		0.36	0.44	98.5	0.8	1.3	88	0.9	1.3	110	0.8	1.2	103	0.8	1.2
		0.44	0.52	81.2	1	1.4	69.6	0.9	1.3	90.7	0.9	1.3	84	0.9	1.3
		0.52	0.6	63.9	0.9	1.4	54.7	0.9	1.3	75.5	0.8	1.3	68.4	0.8	1.4
		0.6	0.68	52.6	0.9	1.5	44.4	0.9	1.3	62.6	0.8	1.4	56.2	0.9	1.4
		0.68	0.76	40.6	0.9	1.5	33.8	1	1.3	51.3	0.8	1.4	45.8	0.9	1.4
		0.76	0.84	31.3	1	1.6	25.8	1.1	1.3	41.7	0.9	1.5	36.1	0.9	1.5
		0.84	0.92	23.9	1.1	1.6	19.9	1.1	1.4	33.7	0.9	1.5	28.6	1	1.5
		0.92	1	17.6	1.2	1.6	14.8	1.2	1.4	26.5	0.9	1.6	22.8	1	1.4
		1	1.08	12.9	1.2	1.6	10.9	1.3	1.4	21	1	1.6	17.1	1	1.4
		1.08	1.16	9.5	1.3	1.6	8.18	1.4	1.5	15.8	1.1	1.6	12.9	1.1	1.4
		1.16	1.24	7.19	1.4	1.6	5.82	1.5	1.5	12	1.1	1.6	9.79	1.2	1.4
		1.24	1.32	5.08	1.6	1.7	4.18	1.6	1.6	8.86	1.2	1.6	7.44	1.3	1.4
		1.32	1.4	3.6	1.8	1.7	2.85	1.9	1.7	6.64	1.2	1.6	5.57	1.4	1.4
		1.4	1.48	2.61	1.9	1.7	1.98	2	1.8	4.73	1.4	1.6	3.92	1.5	1.6
		1.48	1.56	1.81	2.1	1.8	1.26	2.4	2	3.43	1.5	1.7	2.94	1.6	1.8
		1.56	1.64	1.31	2.2	1.9	0.895	2.6	2.1	2.44	1.7	2	2.1	1.7	2
		1.64	1.72	0.92	3.8	2.1	0.522	3.2	2.4	1.85	1.8	2.4	1.48	2.1	2.5
		1.72	1.8	0.649	10.9	2.9	0.306	3.9	2.7	1.25	8	3.3	1.02	2.1	2.9
		1.8	1.88				0.189	4.2	3.1				0.609	2.7	3.5
		1.88	1.96										0.516	24.5	6
-1	-0.92	-0.12	-0.04				338	12.8	2.3				327	13.2	2.1
		-0.04	0.04	261	1.6	1.8	278	1.5	1.3	275	1.6	1.1	292	1.5	1.2
		0.04	0.12	225	1.4	1.6	229	0.8	1.2	233	1.4	1.1	249	0.8	1.1
		0.12	0.2	193	0.7	1.4	189	0.7	1.2	203	0.7	1	207	0.7	1.1
		0.2	0.28	164	0.7	1.3	157	0.7	1.2	174	0.7	1	174	0.7	1.1
		0.28	0.36	136	0.7	1.2	125	0.7	1.2	147	0.7	1	144	0.7	1.1
		0.36	0.44	115	0.8	1.2	105	0.8	1.2	125	0.7	1	120	0.7	1.1
		0.44	0.52	95	0.9	1.3	83.7	0.9	1.2	105	0.9	1.1	97.9	0.9	1.1
		0.52	0.6	75.5	0.7	1.3	64.3	0.8	1.2	85.4	0.7	1.1	80.1	0.7	1.1
		0.6	0.68	60.8	0.7	1.4	51.3	0.8	1.3	73.2	0.7	1.2	65.3	0.7	1.1
		0.68	0.76	48.8	0.8	1.4	40.4	0.8	1.3	60.2	0.7	1.2	53.4	0.8	1.2
		0.76	0.84	37.1	0.8	1.5	31.5	0.9	1.3	49.6	0.7	1.3	42.3	0.8	1.2
		0.84	0.92	29.1	0.9	1.5	23.9	0.9	1.4	39.5	0.8	1.3	33.8	0.8	1.2
		0.92	1	21.9	0.9	1.5	18.4	1	1.4	31.1	0.8	1.4	26.5	0.9	1.3
		1	1.08	15.7	1	1.5	13.1	1.1	1.4	24.6	0.8	1.4	20.2	0.9	1.3
		1.08	1.16	11.6	1.1	1.5	9.3	1.2	1.5	18.9	0.9	1.4	15.8	0.9	1.3
		1.16	1.24	8.42	1.2	1.6	6.94	1.3	1.5	14.3	0.9	1.4	11.8	1	1.2
		1.24	1.32	5.98	1.3	1.6	4.76	1.4	1.6	11.1	1	1.4	8.99	1.1	1.2
		1.32	1.4	4.35	1.4	1.7	3.37	1.5	1.6	7.8	1	1.4	6.6	1.1	1.3
		1.4	1.48	3.06	1.6	1.8	2.23	1.8	1.7	5.57	1.2	1.5	4.78	1.2	1.3
		1.48	1.56	2.06	1.8	1.9	1.48	2	1.9	4.02	1.3	1.5	3.47	1.3	1.4
		1.56	1.64	1.52	2	2	1	2.2	2.1	3.07	1.3	1.6	2.43	1.5	1.6
		1.64	1.72	1.07	3.5	2.3	0.629	2.7	2.5	2.2	1.5	1.7	1.68	1.8	1.9
		1.72	1.8	0.718	9	2.9	0.367	3.5	3	1.57	5.9	2.3	1.13	2.1	2.3
		1.8	1.88				0.229	3.6	3.6				0.752	2	2.7
		1.88	1.96				0.115	20.5	6.4				0.495	10.4	3.8
-0.92	-0.84	-0.04	0.04	299	1.5	1.4	316	1.3	1.1	309	1.5	1.2	329	1.3	1.1
		0.04	0.12	252	1.3	1.3	256	1.2	1.1	263	1.3	1.1	272	1.2	1
		0.12	0.2	213	0.7	1.2	216	0.7	1.1	228	0.7	1	230	0.7	1
		0.2	0.28	184	0.6	1.1	177	0.6	1	195	0.6	1	196	0.6	0.9
		0.28	0.36	155	0.6	1.1	145	0.6	1	166	0.6	1	162	0.6	0.9
		0.36	0.44	129	0.8	1.1	118	0.8	1.1	139	0.8	1	133	0.8	0.9
		0.44	0.52	109	0.9	1.1	93.7	0.9	1.1	116	0.9	1	112	0.9	1
		0.52	0.6	87.1	0.8	1.1	75.7	0.8	1.1	97	0.8	1	91.5	0.8	1
		0.6	0.68	70.4	0.7	1.1	60.2	0.7	1.1	80.4	0.7	1	74.7	0.7	1
		0.68	0.76	57	0.7	1.2	47.8	0.7	1.1	66.8	0.6	1	61.2	0.6	1
		0.76	0.84	44.4	0.7	1.3	36.8	0.7	1.1	55.2	0.6	1.1	49.1	0.7	1.1
		0.84	0.92	34.7	0.7	1.3	27.9	0.8	1.2	45.2	0.7	1.1	38.4	0.7	1.1
		0.92	1	26	0.8	1.4	21	0.9	1.2	37	0.7	1.1	30.8	0.7	1.2
		1	1.08	19.2	0.8	1.5	15.6	0.9	1.3	28.8	0.7	1.2	24.1	0.8	1.2
		1.08	1.16	14	0.9	1.5	11.4	1	1.4	22.6	0.7	1.2	18.6	0.8	1.2
		1.16	1.24	10.2	1	1.6	8.24	1.1	1.4	17.3	0.8	1.3	14.2	0.8	1.2
		1.24	1.32	7.31	1.1	1.7	5.9	1.2	1.4	13	0.8	1.4	10.6	0.9	1.3
		1.32	1.4	5.22	1.2	1.7	4.05	1.3	1.5	9.58	0.9	1.4	7.98	0.9	1.3
		1.4	1.48	3.64	1.3	1.8	2.72	1.5	1.5	6.94	1	1.5	5.78	1	1.3
		1.48	1.56	2.54	1.5	1.8	1.75	1.7	1.6	4.87	1.1	1.6	4.17	1.1	1.4
		1.56	1.64	1.77	2.1	1.8	1.19	1.8	1.7	3.6	1.1	1.7	2.89	1.2	1.6
		1.64	1.72	1.25	2.9	1.9	0.707	2.2	1.9	2.63	1.4	1.8	2.02	1.4	1.7
		1.72	1.8	0.925	5.9	2.2	0.414	2.7	2.1	1.95	3.9	2.2	1.37	1.5	1.9
		1.8	1.88				0.266	2.9	2.4				0.887	2.1	2.1
		1.88	1.96				0.178	10.2	4.3				0.623	5.8	2.7
-0.84	-0.76	-0.04	0.04	317	5.2	1.5	341	4.2	1.4	326	5.3	1.4	360	4.2	1.3
		0.04	0.12	267	1.3	1	285	1.2	1	284	1.3	1	302	1.2	1

Continued on next page

Table H.4 – Continued from previous page

Bin size				158 GeV/c, h^-			158 GeV/c, h^+			350 GeV/c, h^-			350 GeV/c, h^+		
$\log \frac{p_T}{\mathrm{GeV}/c}$		$\log \frac{p}{\mathrm{GeV}/c}$		F	σ_{stat}	σ_{sys}	F	σ_{stat}	σ_{sys}	F	σ_{stat}	σ_{sys}	F	σ_{stat}	σ_{sys}
low	high	low	high		%	%		%	%		%	%		%	%
		0.12	0.2	233	0.6	1	234	0.6	1	242	0.7	0.9	251	0.6	0.9
		0.2	0.28	192	0.7	1	193	0.7	1	207	0.7	0.9	211	0.6	0.9
		0.28	0.36	167	0.6	1	159	0.6	1	178	0.6	0.8	178	0.6	0.9
		0.36	0.44	140	0.7	1	129	0.7	1	151	0.7	0.8	148	0.7	0.9
		0.44	0.52	117	0.8	1	105	0.8	1.1	127	0.8	0.9	120	0.8	0.9
		0.52	0.6	98.1	0.7	1	84.9	0.8	1.1	106	0.7	0.9	99.8	0.7	0.9
		0.6	0.68	81	0.7	1	68.1	0.8	1.1	89	0.7	0.9	82.7	0.7	0.9
		0.68	0.76	64.4	0.6	1	53.7	0.6	1.1	74.3	0.5	0.9	67.3	0.6	0.9
		0.76	0.84	51	0.6	1.1	42.5	0.6	1.1	61.5	0.6	1	54.4	0.6	1
		0.84	0.92	40.4	0.6	1.1	32.3	0.7	1.1	50.5	0.6	1	43.4	0.6	1
		0.92	1	31.1	0.6	1.1	24.5	0.7	1.2	40.7	0.6	1	34.9	0.6	1
		1	1.08	23.4	0.7	1.2	18.5	0.7	1.3	32.4	0.6	1	27.4	0.6	1
		1.08	1.16	17.1	0.7	1.3	13.7	0.8	1.3	25.4	0.6	1	21	0.7	1
		1.16	1.24	12.4	0.8	1.3	9.71	0.9	1.4	20	0.6	1.1	16.3	0.7	1.1
		1.24	1.32	8.76	0.9	1.3	6.77	1	1.4	15.4	0.7	1.1	12.2	0.8	1.1
		1.32	1.4	6.14	1	1.4	4.74	1.1	1.5	11.5	0.7	1.1	9.14	0.8	1.2
		1.4	1.48	4.33	1.1	1.4	3.23	1.2	1.6	8.39	0.8	1.1	6.87	0.9	1.2
		1.48	1.56	3.02	1.2	1.4	2.12	1.4	1.7	5.99	0.9	1.2	4.88	0.9	1.3
		1.56	1.64	2.1	1.8	1.5	1.41	1.5	1.8	4.42	0.9	1.2	3.44	1	1.4
		1.64	1.72	1.47	2.6	1.5	0.859	1.8	2	3.09	1.4	1.3	2.4	1.1	1.6
		1.72	1.8	1.1	4.5	1.8	0.503	2.2	2.3	2.25	3.1	1.5	1.56	1.3	1.8
		1.8	1.88				0.309	2.5	2.7				1.03	1.9	2.1
		1.88	1.96				0.199	7.6	4.1				0.681	4.4	2.6
-0.76	-0.68	0.04	0.12	279	1.3	1.1	301	1.3	1	294	1.3	0.9	320	1.3	0.9
		0.12	0.2	238	0.9	1.1	247	0.8	1	250	1	0.8	263	0.9	0.9
		0.2	0.28	204	0.8	1	205	0.8	1	214	0.8	0.8	220	0.8	0.8
		0.28	0.36	172	0.8	1	169	0.8	1	183	0.8	0.8	185	0.8	0.8
		0.36	0.44	146	0.7	1	138	0.6	0.9	155	0.7	0.8	154	0.6	0.8
		0.44	0.52	123	0.7	1	114	0.7	1	131	0.7	0.9	127	0.7	0.8
		0.52	0.6	103	0.7	1	92.4	0.7	1	110	0.7	0.9	104	0.7	0.8
		0.6	0.68	87	0.7	1	73.1	0.7	1	93.9	0.7	0.9	86.5	0.7	0.8
		0.68	0.76	70.9	0.5	1	58.5	0.5	1	78.2	0.5	0.9	72	0.5	0.8
		0.76	0.84	56.4	0.5	1	46	0.6	1	64.9	0.5	0.9	58.2	0.5	0.9
		0.84	0.92	44.7	0.5	1	35.9	0.6	1.1	53.3	0.5	0.9	47.2	0.5	0.9
		0.92	1	34.8	0.6	1	27.7	0.6	1.1	43.2	0.5	1	37.2	0.6	0.9
		1	1.08	26.8	0.6	1.1	21	0.7	1.1	35.4	0.5	1	30.3	0.6	1
		1.08	1.16	20.3	0.6	1.1	15.5	0.7	1.2	28.4	0.5	1	23.4	0.6	1
		1.16	1.24	14.6	0.7	1.2	11.4	0.8	1.2	22.4	0.6	1	18.1	0.6	1.1
		1.24	1.32	10.4	0.7	1.2	8	0.8	1.3	17.7	0.6	1	13.8	0.7	1.1
		1.32	1.4	7.19	0.8	1.2	5.48	0.9	1.3	13.2	0.6	1	10.5	0.7	1.2
		1.4	1.48	5.11	0.9	1.3	3.74	1	1.4	9.99	0.7	1	7.74	0.7	1.3
		1.48	1.56	3.55	1.2	1.3	2.5	1.2	1.5	7.25	0.7	1.1	5.6	0.8	1.5
		1.56	1.64	2.46	1.7	1.4	1.59	1.3	1.6	5.29	0.8	1.1	4.01	0.9	1.7
		1.64	1.72	1.75	2.2	1.4	0.98	1.5	1.7	3.7	1.2	1.2	2.72	1	1.9
		1.72	1.8	1.2	3.6	1.6	0.576	1.9	1.9	2.59	2.4	1.4	1.81	1.3	2.2
		1.8	1.88				0.327	2.4	2.2				1.18	1.9	2.6
		1.88	1.96				0.232	5.4	3.2				0.78	3.2	3.1
-0.68	-0.6	-0.2	-0.12	421	1.8	1.4	529	1.9	1.6	429	1.8	1.3	522	2	1.2
		-0.12	-0.04	374	1.5	1.3	436	1.7	1.6	386	1.6	1.2	449	1.7	1.1
		-0.04	0.04	321	13.8	2.2				339	14	2.1			
		0.04	0.12	277	3.9	1.4	302	3	1.5	287	4	1.3	320	2.9	1.1
		0.12	0.2	234	1.2	1.1	253	1.1	1.4	244	1.2	1	267	1.1	0.9
		0.2	0.28	199	1	1	208	0.9	1.3	207	1	0.9	218	0.9	0.9
		0.28	0.36	170	0.7	1	170	0.7	1.3	180	0.7	0.9	184	0.7	0.9
		0.36	0.44	145	0.7	1	140	0.7	1.2	152	0.8	0.9	156	0.7	0.9
		0.44	0.52	122	0.7	1	113	0.7	1.2	129	0.7	0.8	127	0.7	0.9
		0.52	0.6	103	0.6	0.9	92.7	0.7	1.2	110	0.6	0.8	106	0.6	0.9
		0.6	0.68	85.5	0.6	0.9	75.2	0.6	1.1	92.1	0.6	0.8	86.9	0.6	0.9
		0.68	0.76	71.1	0.4	0.9	60.7	0.5	1.1	77.2	0.4	0.8	71.9	0.5	0.9
		0.76	0.84	58.5	0.5	0.9	48.5	0.5	1.1	64.1	0.4	0.8	58.8	0.5	0.9
		0.84	0.92	47.5	0.5	1	37.8	0.5	1.1	53.3	0.5	0.9	47.8	0.5	0.9
		0.92	1	37.7	0.5	1	29.2	0.5	1.1	43.4	0.5	0.9	38.7	0.5	0.9
		1	1.08	29.2	0.5	1	22.5	0.6	1.1	36.2	0.5	0.9	30.8	0.5	1
		1.08	1.16	22.2	0.5	1	17.1	0.6	1.1	29.4	0.5	0.9	24.5	0.5	1
		1.16	1.24	16.7	0.6	1.1	12.6	0.6	1.1	23.8	0.5	1	18.8	0.5	1
		1.24	1.32	12.2	0.6	1.1	9.03	0.7	1.2	18.4	0.5	1	14.7	0.6	1.1
		1.32	1.4	8.52	0.7	1.1	6.28	0.8	1.3	14.4	0.5	1	11.2	0.6	1.2
		1.4	1.48	5.89	0.8	1.2	4.32	0.9	1.4	11	0.6	1.1	8.46	0.6	1.4
		1.48	1.56	4.05	1.1	1.2	2.83	1	1.5	8.31	0.6	1.1	6.16	0.7	1.6
		1.56	1.64	2.78	1.4	1.3	1.79	1.2	1.6	6	0.8	1.2	4.38	0.8	2
		1.64	1.72	1.98	1.6	1.4	1.06	1.4	1.7	4.3	1.1	1.3	3.05	0.9	2.3
		1.72	1.8	1.38	2.8	1.6	0.646	1.6	1.9	3	1.9	1.4	2.06	1.3	2.7
		1.8	1.88				0.387	2.4	2.3				1.37	1.6	3.2
		1.88	1.96				0.232	4.6	3				0.901	2.4	3.8
-0.6	-0.52	-0.28	-0.2	438	2.2	1.6	627	2.4	1.6	426	2.3	1.3	604	2.5	1.4
		-0.2	-0.12	389	2.2	1.6	510	1.8	1.5	373	2.4	1.3	513	1.9	1.3
		-0.12	-0.04	339	1.8	1.5	409	2	1.5	348	1.8	1.2	429	2	1.3
		-0.04	0.04	292	1.7	1.4	352	1.5	1.5	301	1.8	1.1	350	1.6	1.2
		0.04	0.12	246	2.4	1.4	295	4.3	1.6	261	2.4	1.1	298	4.4	1.3
		0.12	0.2	212	1.1	1.3	238	1.1	1.4	224	1.2	1	254	1.1	1
		0.2	0.28	182	1	1.2	196	0.9	1.3	192	1	0.9	208	0.9	1
		0.28	0.36	155	0.9	1.2	160	0.8	1.3	162	0.9	0.9	173	0.8	1
		0.36	0.44	132	0.7	1.2	133	0.6	1.3	140	0.7	0.8	144	0.7	0.9
		0.44	0.52	114	0.7	1.2	110	0.7	1.2	118	0.7	0.8	120	0.7	0.9
		0.52	0.6	95.3	0.6	1.1	88.8	0.7	1.2	101	0.7	0.8	98.9	0.7	0.9
		0.6	0.68	80.5	0.6	1.1	71.9	0.7	1.2	85.3	0.6	0.8	82.2	0.6	0.9
		0.68	0.76	67.8	0.5	1	59	0.5	1.2	72.9	0.5	0.8	68.4	0.5	0.9
		0.76	0.84	56.3	0.4	1	47.4	0.5	1.1	60	0.4	0.8	56.9	0.4	0.9
		0.84	0.92	45.9	0.4	1	37.5	0.5	1.1	49.6	0.4	0.8	45.2	0.5	0.9
		0.92	1	37.5	0.4	1	29.4	0.5	1.1	41.1	0.4	0.8	37.2	0.5	0.9
		1	1.08	29.9	0.5	1	22.9	0.5	1.1	34.5	0.4	0.9	30.2	0.5	0.9
		1.08	1.16	23.4	0.5	1	17.4	0.5	1.1	28.3	0.4	0.9	24.2	0.5	0.9
		1.16	1.24	17.8	0.5	1.1	13	0.6	1.2	23.2	0.4	0.9	18.9	0.5	0.9
		1.24	1.32	13.3	0.5	1.1	9.6	0.6	1.3	18.3	0.5	0.9	14.7	0.5	0.9
		1.32	1.4	9.58	0.7	1.2	6.9	0.7	1.4	14.6	0.5	1	11.4	0.5	1

Continued on next page

Table H.4 – Continued from previous page

Bin size				158 GeV/c, h^-			158 GeV/c, h^+			350 GeV/c, h^-			350 GeV/c, h^+		
$\log \frac{p_T}{\mathrm{GeV}/c}$		$\log \frac{p}{\mathrm{GeV}/c}$		F	σ_{stat}	σ_{sys}	F	σ_{stat}	σ_{sys}	F	σ_{stat}	σ_{sys}	F	σ_{stat}	σ_{sys}
low	high	low	high		%	%		%	%		%	%		%	%
		1.4	1.48	6.81	0.7	1.3	4.78	0.7	1.6	11.5	0.5	1	8.79	0.6	1.1
		1.48	1.56	4.62	0.9	1.5	3.13	0.9	1.7	8.63	0.7	1	6.53	0.6	1.4
		1.56	1.64	3.11	1.1	1.8	1.99	1	2	6.43	0.7	1	4.69	0.8	1.9
		1.64	1.72	2.11	1.5	2.2	1.19	1.2	2.3	4.79	1	1.1	3.35	0.9	2.4
		1.72	1.8	1.47	2.4	2.8	0.73	1.4	2.6	3.49	1.5	1.2	2.27	1.2	3.1
		1.8	1.88				0.403	2.3	3.1				1.52	1.4	4
		1.88	1.96				0.239	3.7	3.9				1.04	2	5
-0.52	-0.44	-0.28	-0.2	360	2.1	1.5	571	1.6	1.5	357	2.2	1.5	565	1.6	1.7
		-0.2	-0.12	324	2.1	1.5	467	1.7	1.5	323	2.2	1.4	485	1.7	1.7
		-0.12	-0.04	284	1.5	1.4	387	1.2	1.3	295	1.5	1.3	379	1.3	1.6
		-0.04	0.04	249	1.6	1.3	317	1.4	1.3	251	1.6	1.2	318	1.4	1.5
		0.04	0.12	213	2	1.3	263	1.8	1.3	215	2.1	1.2	271	1.8	1.5
		0.12	0.2	182	1.8	1.2	211	1.6	1.2	190	1.8	1.1	226	1.6	1.4
		0.2	0.28	158	1	1.1	174	1	1.2	163	1	1	187	1	1.4
		0.28	0.36	135	1	1.1	143	0.9	1.2	143	1	1	152	0.9	1.3
		0.36	0.44	116	0.8	1	120	0.8	1.1	121	0.9	1	126	0.8	1.3
		0.44	0.52	96.2	0.7	1	97.6	0.7	1.1	101	0.8	0.9	107	0.7	1.3
		0.52	0.6	82.6	0.7	1	80.7	0.7	1.1	89.3	0.7	0.9	88.2	0.7	1.2
		0.6	0.68	70.4	0.7	1	65.2	0.7	1.1	74.5	0.7	0.9	73.1	0.7	1.2
		0.68	0.76	59.3	0.5	0.9	53.1	0.5	1.1	62.7	0.5	0.9	60.6	0.5	1.1
		0.76	0.84	49.8	0.5	0.9	43.3	0.5	1.1	52.4	0.5	0.8	50.6	0.5	1.1
		0.84	0.92	41.3	0.4	0.9	34.8	0.5	1.1	43.7	0.4	0.8	41.1	0.5	1
		0.92	1	34.1	0.4	1	27.4	0.5	1	36.8	0.4	0.8	33.5	0.4	1
		1	1.08	27.6	0.4	1	21.4	0.5	1.1	30.3	0.4	0.8	27	0.4	0.9
		1.08	1.16	22.2	0.4	1	16.7	0.5	1.1	25.3	0.4	0.9	21.9	0.5	0.9
		1.16	1.24	17.4	0.5	1	12.7	0.5	1.1	20.6	0.4	0.9	17.3	0.5	0.9
		1.24	1.32	13.1	0.5	1	9.32	0.6	1.2	17	0.4	0.9	13.6	0.5	1
		1.32	1.4	9.92	0.6	1.1	6.84	0.6	1.3	13.9	0.5	1	10.7	0.5	1.1
		1.4	1.48	7.15	0.6	1.1	4.85	0.7	1.4	11	0.5	1	8.3	0.6	1.3
		1.48	1.56	5.08	0.7	1.2	3.34	0.8	1.6	8.52	0.6	1.1	6.18	0.7	1.6
		1.56	1.64	3.45	0.9	1.3	2.13	0.9	1.8	6.49	0.7	1.2	4.54	0.8	2.1
		1.64	1.72	2.28	1.3	1.4	1.33	1.1	2	4.91	0.9	1.4	3.36	0.8	2.6
		1.72	1.8	1.54	2	1.6	0.762	1.5	2.2	3.6	1.3	1.6	2.39	1	3.3
		1.8	1.88	1.06	3.2	1.9	0.439	2	2.5	2.54	2.2	2	1.6	1.2	4
		1.88	1.96				0.241	3.3	3	1.84	8.6	2.6	1.08	1.7	5
-0.44	-0.36	-0.2	-0.12	233	2.1	1.6	407	1.5	1.7	244	2.2	1.5	394	1.6	1.6
		-0.12	-0.04	223	2.1	1.5	328	1.7	1.7	220	2.2	1.5	321	1.7	1.5
		-0.04	0.04	189	1.5	1.4	263	1.3	1.5	191	1.6	1.3	274	1.3	1.4
		0.04	0.12	165	1.5	1.3	219	1.3	1.4	168	1.5	1.3	235	1.2	1.3
		0.12	0.2	147	1.7	1.3	182	1.5	1.4	150	1.8	1.2	186	1.6	1.2
		0.2	0.28	125	0.9	1.1	149	0.9	1.2	130	0.9	1.1	158	0.9	1.2
		0.28	0.36	108	1	1.1	121	1.1	1.2	111	1	1	128	1.1	1.2
		0.36	0.44	92.6	1	1.1	100	0.9	1.2	95.6	1	1	105	0.9	1.1
		0.44	0.52	77.8	0.9	1.1	81.6	0.9	1.1	81.6	0.9	0.9	87.3	0.9	1.1
		0.52	0.6	66.9	0.7	1	66.4	0.7	1.1	69.4	0.7	0.9	71.9	0.7	1.1
		0.6	0.68	57	0.7	1	54.9	0.7	1.1	59.9	0.7	0.9	60.4	0.7	1.1
		0.68	0.76	48.6	0.6	1	45.5	0.6	1	50.8	0.6	0.8	50.3	0.6	1
		0.76	0.84	40.5	0.5	1	36.2	0.5	1	43.1	0.5	0.8	41.9	0.5	1
		0.84	0.92	33.9	0.5	1	29.3	0.5	1	35.9	0.5	0.8	34.4	0.5	1
		0.92	1	28.4	0.5	1	23.7	0.5	0.9	30.1	0.5	0.8	28.1	0.5	1
		1	1.08	23.2	0.4	1	18.5	0.5	0.9	24.6	0.4	0.8	22.8	0.4	0.9
		1.08	1.16	19.1	0.4	1	14.5	0.5	1	20.7	0.4	0.9	18.5	0.5	0.9
		1.16	1.24	15.4	0.5	1	11.1	0.5	1	17.2	0.4	0.9	15	0.5	1
		1.24	1.32	12.1	0.5	1	8.48	0.5	1	14.1	0.5	0.9	11.9	0.5	1
		1.32	1.4	9.29	0.5	1	6.27	0.6	1.1	11.7	0.5	0.9	9.27	0.6	1.2
		1.4	1.48	6.99	0.6	1.1	4.52	0.7	1.2	9.58	0.5	1	7.23	0.6	1.4
		1.48	1.56	5.02	0.7	1.2	3.14	0.8	1.4	7.64	0.5	1	5.53	0.6	1.8
		1.56	1.64	3.49	0.8	1.3	2.12	0.9	1.7	5.99	0.7	1.1	4.09	0.7	2.3
		1.64	1.72	2.31	1.2	1.4	1.34	1.1	2.1	4.48	0.9	1.1	3.03	0.8	3
		1.72	1.8	1.51	1.4	1.5	0.807	1.4	2.5	3.39	1	1.2	2.21	0.9	3.8
		1.8	1.88	0.981	2.2	1.7	0.452	1.8	3	2.52	1.4	1.4	1.57	1	4.7
		1.88	1.96	0.646	19.7	3	0.221	3	3.8	1.71	7.8	2	1.08	1.4	5.9
-0.36	-0.28	-0.12	-0.04	141	2.3	1.6	259	1.6	1.9	149	2.4	1.7	257	1.7	2
		-0.04	0.04	137	2.2	1.5	216	1.7	1.8	133	2.4	1.6	222	1.7	1.8
		0.04	0.12	116	2	1.4	175	1.5	1.6	127	1.9	1.5	180	1.6	1.5
		0.12	0.2	104	1.7	1.3	143	1.4	1.4	107	1.7	1.3	146	1.4	1.3
		0.2	0.28	88.6	1.7	1.2	116	1.4	1.3	94.8	1.7	1.2	118	1.5	1.2
		0.28	0.36	77.5	0.9	1.1	94.3	0.9	1.2	80.6	0.9	1	97.3	0.9	1.1
		0.36	0.44	67.2	0.9	1.1	76.4	0.8	1.2	69.8	0.9	1	81.5	0.8	1.1
		0.44	0.52	58.1	1	1	62.4	0.8	1.2	60.3	1	1	67.6	0.8	1.2
		0.52	0.6	49.2	0.8	1	51.6	0.8	1.3	51.8	0.8	0.9	55.8	0.8	1.2
		0.6	0.68	41.5	0.7	1	41.7	0.7	1.2	44.5	0.7	0.9	45.8	0.7	1.2
		0.68	0.76	35.9	0.7	1	35	0.6	1.2	37.8	0.7	0.9	38.7	0.6	1.2
		0.76	0.84	30.8	0.6	1	28.3	0.6	1.1	32.5	0.6	0.8	32.2	0.6	1.2
		0.84	0.92	25.4	0.6	0.9	23	0.6	1.1	27.3	0.6	0.8	26.7	0.6	1.1
		0.92	1	21.2	0.5	1	18.5	0.6	1.1	22.9	0.5	0.8	22.2	0.5	1.1
		1	1.08	17.9	0.5	1	14.7	0.5	1	19	0.5	0.8	17.9	0.5	1.1
		1.08	1.16	14.7	0.5	1	11.5	0.5	1	15.8	0.5	0.8	14.4	0.5	1
		1.16	1.24	12.2	0.5	1	8.97	0.5	1	13.1	0.5	0.8	11.6	0.5	1.1
		1.24	1.32	9.85	0.5	1	6.86	0.6	1.1	10.8	0.5	0.8	9.34	0.5	1.2
		1.32	1.4	7.83	0.5	1	5.15	0.6	1.1	8.96	0.5	0.9	7.4	0.6	1.3
		1.4	1.48	6.01	0.5	1.1	3.8	0.7	1.2	7.49	0.5	0.9	5.8	0.6	1.5
		1.48	1.56	4.45	0.7	1.2	2.71	0.8	1.4	6.11	0.6	1	4.48	0.6	1.9
		1.56	1.64	3.18	0.9	1.3	1.84	0.9	1.6	4.85	0.7	1.1	3.33	0.7	2.3
		1.64	1.72	2.17	0.9	1.4	1.2	1	1.8	3.86	0.7	1.1	2.51	0.8	2.8
		1.72	1.8	1.45	1.1	1.6	0.763	1.3	2.1	2.95	0.8	1.3	1.89	0.8	3.5
		1.8	1.88	0.921	1.9	1.9	0.431	1.7	2.6	2.27	1.2	1.5	1.37	1	4.2
		1.88	1.96	0.561	12.7	2.8	0.209	2.8	3.2	1.68	7	2.2	0.979	1.3	5.2
		1.96	2.04				0.113	7.4	4.7				0.716	3.2	6.4
-0.28	-0.2	0.04	0.12	75.8	2.5	1.9	130	1.8	1.7	73.3	2.6	2	133	1.8	1.6
		0.12	0.2	66.1	2.1	1.7	102	1.7	1.6	67.5	2.2	1.8	110	1.7	1.5
		0.2	0.28	56.5	2.1	1.5	85	1.6	1.5	60	2.1	1.6	87.2	1.7	1.3
		0.28	0.36	51.7	1.5	1.3	68.1	1.3	1.4	51.9	1.6	1.4	73	1.3	1.2
		0.36	0.44	44.7	1	1.2	55.4	0.9	1.2	46.3	1	1.2	57.9	0.9	1.1
		0.44	0.52	38	0.9	1.1	44.8	0.8	1.2	39.8	0.9	1.1	47.6	0.8	1.1

Continued on next page

Table H.4 – Continued from previous page

Bin size				158 GeV/c, h^-			158 GeV/c, h^+			350 GeV/c, h^-			350 GeV/c, h^+		
log $\frac{p_T}{\mathrm{GeV}/c}$		log $\frac{p}{\mathrm{GeV}/c}$		F	σ_{stat}	σ_{sys}	F	σ_{stat}	σ_{sys}	F	σ_{stat}	σ_{sys}	F	σ_{stat}	σ_{sys}
low	high	low	high		%	%		%	%		%	%		%	%
		0.52	0.6	33.3	0.9	1.1	36	0.8	1.1	35.7	0.9	1	39.8	0.8	1.1
		0.6	0.68	28.8	0.8	1	29.9	0.8	1.1	30.2	0.8	1	32.5	0.8	1.1
		0.68	0.76	24.3	0.8	1	24.4	0.7	1.1	26.4	0.8	1.1	27.6	0.7	1.1
		0.76	0.84	20.9	0.7	1.1	20.3	0.7	1.1	22.4	0.7	1.1	22.8	0.7	1.2
		0.84	0.92	17.7	0.7	1.1	16.7	0.7	1.2	18.6	0.7	1.2	19	0.7	1.2
		0.92	1	14.6	0.6	1.1	13.3	0.6	1.2	15.8	0.6	1.2	15.8	0.6	1.3
		1	1.08	12.3	0.6	1.1	10.7	0.6	1.2	13.3	0.6	1.2	12.8	0.6	1.3
		1.08	1.16	10.3	0.5	1.1	8.46	0.6	1.1	11.1	0.5	1.1	10.3	0.5	1.3
		1.16	1.24	8.43	0.5	1.1	6.53	0.6	1.1	9.1	0.5	1.1	8.26	0.5	1.3
		1.24	1.32	7.01	0.5	1.2	5.08	0.6	1.1	7.5	0.5	1.1	6.77	0.5	1.3
		1.32	1.4	5.72	0.5	1.2	3.88	0.6	1.2	6.38	0.5	1	5.38	0.6	1.4
		1.4	1.48	4.62	0.6	1.2	2.86	0.7	1.3	5.26	0.6	1	4.22	0.6	1.5
		1.48	1.56	3.52	0.7	1.2	2.02	0.8	1.5	4.34	0.7	1	3.25	0.7	1.8
		1.56	1.64	2.63	0.8	1.2	1.41	0.9	1.8	3.57	0.7	1.1	2.47	0.7	2.2
		1.64	1.72	1.84	0.9	1.2	0.951	1.1	2	2.83	0.7	1.1	1.86	0.8	2.8
		1.72	1.8	1.25	1.2	1.3	0.605	1.4	2.4	2.26	0.9	1.2	1.43	0.9	3.5
		1.8	1.88	0.795	1.8	1.3	0.364	1.7	2.8	1.75	1.2	1.3	1.08	1	4.4
		1.88	1.96	0.509	5.9	1.8	0.183	2.4	3.4	1.39	3.5	1.8	0.77	1.3	5.5
		1.96	2.04				0.0951	5.1	4.6				0.558	2.2	6.9
-0.2	-0.12	0.12	0.2	36.9	3	2.9	70.8	2	1.9	37	3.1	2.4	74.4	2	1.9
		0.2	0.28	32.9	2.6	2.6	57.4	1.8	1.8	34.7	2.6	2.2	58.8	1.9	1.7
		0.28	0.36	29.5	2.4	2.2	45.5	1.9	1.6	30.8	2.5	1.9	47.1	2	1.5
		0.36	0.44	26.1	1.3	1.8	36.3	1	1.4	26.9	1.3	1.6	39.1	1	1.2
		0.44	0.52	23.1	1.1	1.6	29.3	1	1.3	23.8	1.2	1.4	30.7	1	1.1
		0.52	0.6	20	1	1.4	23.9	0.9	1.2	21.1	1.1	1.3	25.5	0.9	1.1
		0.6	0.68	17.8	1	1.3	19.5	0.9	1.2	18.6	1	1.2	21.4	0.9	1
		0.68	0.76	15.4	1	1.2	16.1	0.9	1.1	16.2	1	1.1	18.1	0.9	1
		0.76	0.84	13.3	0.8	1.2	13.4	0.9	1.1	14.1	0.9	1.1	15.2	0.9	1
		0.84	0.92	11.2	0.8	1.1	11	0.8	1.1	12.3	0.8	1.1	12.6	0.8	1
		0.92	1	9.57	0.8	1.1	8.83	0.8	1.1	10.2	0.8	1	10.3	0.8	1.1
		1	1.08	7.95	0.7	1.1	7.08	0.8	1.2	8.58	0.7	1	8.37	0.7	1.1
		1.08	1.16	6.67	0.7	1	5.59	0.7	1.2	7.34	0.7	1	6.91	0.7	1.3
		1.16	1.24	5.5	0.6	1	4.4	0.7	1.2	6.07	0.6	1	5.57	0.6	1.5
		1.24	1.32	4.54	0.6	1	3.36	0.6	1.3	5.02	0.6	1	4.46	0.6	1.7
		1.32	1.4	3.72	0.7	1.1	2.53	0.7	1.4	4.14	0.7	1	3.51	0.6	2
		1.4	1.48	3.06	0.7	1.1	1.89	0.8	1.5	3.44	0.7	1	2.72	0.6	2.3
		1.48	1.56	2.47	0.7	1.1	1.37	0.9	1.7	2.81	0.7	1	2.12	0.7	2.6
		1.56	1.64	1.88	0.7	1.2	0.974	1	1.8	2.29	0.7	1.1	1.66	0.8	2.9
		1.64	1.72	1.38	1	1.3	0.645	1.2	2	1.87	0.9	1.1	1.28	0.9	3.2
		1.72	1.8	0.973	1.2	1.4	0.414	1.5	2.2	1.51	1	1.1	0.973	1	3.6
		1.8	1.88	0.645	1.7	1.5	0.255	1.8	2.4	1.23	1.2	1.2	0.756	1.1	4.1
		1.88	1.96	0.394	3.2	1.8	0.135	2.7	2.8	0.965	2.1	1.4	0.558	1.4	4.6
		1.96	2.04				0.0596	5.9	3.8				0.395	2.2	5.4
-0.12	-0.04	0.2	0.28	14.9	5.1	4.2	34	2.4	2.9	15.8	5.1	4	34	2.5	2.5
		0.28	0.36	14.1	3.3	3.5	26.7	2.3	2.6	14.5	3.4	3.3	28.4	2.3	2.3
		0.36	0.44	12.6	3.2	3	20.8	2.4	2.3	13.4	3.3	2.9	22.1	2.4	2
		0.44	0.52	11.5	1.6	2.4	16.3	1.3	1.9	12.4	1.6	2.3	18.3	1.3	1.7
		0.52	0.6	10.5	1.3	2	13.7	1.1	1.7	11.5	1.3	1.9	14.9	1.1	1.5
		0.6	0.68	9.39	1.2	1.8	11.2	1.1	1.6	10.2	1.2	1.6	12.3	1.1	1.4
		0.68	0.76	8.23	1.2	1.6	9.34	1	1.5	8.82	1.2	1.4	10.1	1	1.3
		0.76	0.84	7.29	1.1	1.4	7.67	1.1	1.5	7.93	1.1	1.3	8.85	1.1	1.2
		0.84	0.92	6.33	1.1	1.4	6.42	1.1	1.4	7.04	1.1	1.2	7.47	1	1.2
		0.92	1	5.38	1.1	1.3	5.3	1	1.4	5.96	1.1	1.2	6.19	1	1.2
		1	1.08	4.6	1	1.2	4.27	1.3	1.4	5.22	1	1.2	5.13	1.2	1.2
		1.08	1.16	3.81	1	1.2	3.32	1	1.3	4.27	1	1.1	4.18	1	1.2
		1.16	1.24	3.2	1	1.2	2.62	0.9	1.3	3.59	1	1.1	3.41	0.9	1.3
		1.24	1.32	2.66	0.8	1.2	2.05	0.8	1.3	3.01	0.8	1.1	2.67	0.8	1.4
		1.32	1.4	2.15	0.7	1.2	1.54	0.8	1.3	2.49	0.7	1.1	2.17	0.7	1.6
		1.4	1.48	1.77	0.7	1.2	1.14	0.9	1.3	2.08	0.7	1.1	1.71	0.7	1.7
		1.48	1.56	1.43	0.8	1.2	0.848	0.9	1.5	1.67	0.8	1.2	1.34	0.7	2
		1.56	1.64	1.13	1	1.4	0.594	1.2	1.8	1.36	0.9	1.2	1.03	0.9	2.3
		1.64	1.72	0.882	1.1	1.5	0.399	1.4	2.4	1.13	1	1.3	0.778	1.1	2.8
		1.72	1.8	0.642	1.3	1.8	0.263	1.7	3.3	0.865	1.2	1.4	0.593	1.2	3.4
		1.8	1.88	0.439	1.8	2.2	0.157	2.2	4.5	0.733	1.4	1.5	0.434	1.4	4.2
		1.88	1.96	0.284	2.5	2.8	0.0829	3	6	0.592	1.8	1.7	0.358	1.5	5.2
		1.96	2.04				0.0354	5.7	7.9				0.231	2.2	6.3
-0.04	0.04	0.36	0.44	5.35	4.6	4.3	10.5	3.2	2.4	5.35	4.9	3.7	11.8	3.2	2.4
		0.44	0.52	4.89	4.3	3.8	8.56	3.1	2.3	5.34	4.3	3.2	8.74	3.2	2.2
		0.52	0.6	4.87	2	3.1	6.75	1.7	2	4.97	2.1	2.7	7.66	1.6	1.9
		0.6	0.68	4.3	1.8	2.7	5.78	1.5	1.9	4.74	1.8	2.5	6.25	1.5	1.9
		0.68	0.76	3.99	1.5	2.3	4.67	1.4	1.8	4.33	1.5	2.2	5.5	1.3	1.8
		0.76	0.84	3.66	1.4	2	3.98	1.3	1.7	3.76	1.4	2	4.57	1.3	1.9
		0.84	0.92	3.1	1.4	1.7	3.37	1.3	1.7	3.46	1.3	1.8	3.91	1.2	2
		0.92	1	2.69	1.5	1.6	2.73	1.3	1.6	3.06	1.4	1.7	3.25	1.3	2.1
		1	1.08	2.31	1.4	1.5	2.28	1.4	1.6	2.59	1.4	1.7	2.71	1.3	2.2
		1.08	1.16	1.98	1.6	1.5	1.78	1.9	1.6	2.23	1.5	1.6	2.28	1.8	2.4
		1.16	1.24	1.6	1.4	1.4	1.39	1.5	1.5	1.92	1.3	1.5	1.85	1.3	2.4
		1.24	1.32	1.38	1	1.4	1.11	1.1	1.5	1.61	1	1.4	1.46	1.1	2.4
		1.32	1.4	1.13	0.9	1.4	0.84	1.2	1.5	1.33	0.9	1.3	1.17	1	2.3
		1.4	1.48	0.901	1	1.4	0.618	1.2	1.6	1.08	1	1.3	0.922	1	2.2
		1.48	1.56	0.724	1.1	1.5	0.456	1.3	1.7	0.889	1	1.3	0.727	1.1	2.2
		1.56	1.64	0.577	1.2	1.5	0.317	1.5	1.9	0.728	1.1	1.3	0.555	1.2	2.3
		1.64	1.72	0.453	1.3	1.6	0.217	1.7	2.2	0.592	1.2	1.4	0.438	1.3	2.5
		1.72	1.8	0.345	1.6	1.6	0.138	2.1	2.6	0.479	1.4	1.5	0.328	1.5	2.9
		1.8	1.88	0.243	2.1	1.8	0.0828	2.7	3.1	0.377	1.7	1.7	0.242	1.6	3.3
		1.88	1.96	0.168	2.8	1.9	0.0405	3.9	3.8	0.312	2	1.9	0.192	1.8	3.8
		1.96	2.04	0.103	6.4	2.6	0.02	5.9	5.1	0.258	4.1	2.6	0.131	2.4	4.5
		2.04	2.12				0.00551	25.4	9.2				0.0892	5.4	5.6
0.04	0.12	0.44	0.52	2.3	29.1	8.7				2.08	32.3	8.6			
		0.52	0.6	1.93	8.5	4.8	3.12	5.1	3.3	1.74	9.2	5.2	3.34	5.1	3.8
		0.6	0.68	1.68	2.9	3.6	2.43	2.5	2.8	1.83	2.8	4.2	2.84	2.5	3.2
		0.68	0.76	1.57	2.5	3.3	2.1	2	2.6	1.67	2.5	3.9	2.46	2	2.9
		0.76	0.84	1.45	2.1	3.1	1.8	1.8	2.4	1.58	2	3.6	2.07	1.8	2.6
		0.84	0.92	1.34	1.9	2.9	1.45	1.7	2.3	1.49	1.9	3.3	1.7	1.7	2.3
		0.92	1	1.17	1.8	2.6	1.24	1.6	2.2	1.3	1.8	2.9	1.53	1.5	2.2

Continued on next page

Table H.4 – Continued from previous page

Bin size				158 GeV/c, h^-			158 GeV/c, h^+			350 GeV/c, h^-			350 GeV/c, h^+		
$\log \frac{p_T}{\mathrm{GeV}/c}$		$\log \frac{p}{\mathrm{GeV}/c}$		F	σ_{stat}	σ_{sys}	F	σ_{stat}	σ_{sys}	F	σ_{stat}	σ_{sys}	F	σ_{stat}	σ_{sys}
low	high	low	high		%	%		%	%		%	%		%	%
		1	1.08	1.01	2.1	2.5	1.05	1.7	2.2	1.14	2	2.7	1.26	1.6	2.2
		1.08	1.16	0.909	1.8	2.3	0.854	2	2.2	1.04	1.8	2.5	1.07	1.9	2.3
		1.16	1.24	0.773	2.3	2.2	0.673	3.1	2.4	0.884	2.2	2.4	0.888	2.7	2.5
		1.24	1.32	0.612	2.3	2.2	0.521	2.4	2.2	0.746	2.2	2.2	0.726	2.1	2.5
		1.32	1.4	0.506	1.9	2.1	0.403	2.1	2.2	0.623	1.8	2.1	0.589	1.8	2.5
		1.4	1.48	0.401	1.7	2	0.298	1.8	2.3	0.519	1.5	1.9	0.46	1.6	2.5
		1.48	1.56	0.324	1.6	2.1	0.217	1.8	2.5	0.444	1.4	1.9	0.358	1.5	2.7
		1.56	1.64	0.261	1.6	2.2	0.157	2	2.9	0.354	1.4	1.8	0.284	1.6	3.1
		1.64	1.72	0.207	1.8	2.4	0.0988	2.3	3.5	0.283	1.6	1.9	0.208	1.7	3.8
		1.72	1.8	0.149	2.3	2.6	0.0666	2.9	4.4	0.225	1.9	2	0.159	1.9	4.9
		1.8	1.88	0.116	2.4	2.9	0.0398	3.5	5.5	0.185	1.9	2.1	0.116	2.1	6.3
		1.88	1.96	0.0769	3.5	3.2	0.0196	5.1	7	0.145	2.5	2.3	0.0883	2.4	8
		1.96	2.04	0.0471	6.2	3.9	0.00851	8.5	9.1	0.12	3.9	2.8	0.0694	2.8	10.1
		2.04	2.12				0.00186	25.6	12.9				0.0406	4.4	12.8
0.12	0.2	0.52	0.6				0.976	35.7	7.5				1.18	38.2	7.6
		0.6	0.68	0.475	7.5	9.9	0.886	6.7	3.9	0.503	7.4	7.5	1.02	6.8	3.7
		0.68	0.76	0.489	4.6	8	0.764	3.4	3.3	0.552	4.5	6.7	0.875	3.3	3.1
		0.76	0.84	0.526	3.4	6.4	0.672	2.9	3.2	0.547	3.4	6.2	0.767	2.8	3
		0.84	0.92	0.494	2.9	5	0.549	2.8	3.2	0.527	2.9	5.7	0.695	2.6	3
		0.92	1	0.403	2.8	4	0.474	2.4	3.2	0.487	2.7	5.1	0.59	2.2	3
		1	1.08	0.361	2.7	3.5	0.396	2.4	3.2	0.436	2.5	4.5	0.52	2.2	3.1
		1.08	1.16	0.336	2.7	3.2	0.34	2.7	3.3	0.402	2.6	4.1	0.434	2.5	3.2
		1.16	1.24	0.298	2.8	3	0.272	2.7	3.3	0.343	2.7	3.8	0.381	2.4	3.4
		1.24	1.32	0.246	3.8	3.2	0.232	3.7	3.5	0.291	3.8	3.8	0.31	3.3	3.7
		1.32	1.4	0.221	3.2	2.9	0.166	3.8	3.3	0.265	3.1	3.5	0.248	3.1	3.7
		1.4	1.48	0.166	2.8	2.7	0.118	3.7	3.2	0.227	2.5	3.3	0.197	3.1	3.8
		1.48	1.56	0.139	2.4	2.5	0.0924	3	2.8	0.184	2.1	2.9	0.156	2.4	3.7
		1.56	1.64	0.106	2.2	2.4	0.0606	3	2.8	0.151	2	2.8	0.123	2.2	3.7
		1.64	1.72	0.0832	2.5	2.5	0.0449	3.3	2.9	0.123	2.2	2.8	0.0969	2.3	3.7
		1.72	1.8	0.0621	2.9	2.6	0.0281	3.9	3.3	0.0985	2.4	3.1	0.0707	2.5	3.8
		1.8	1.88	0.0439	3.6	2.7	0.0152	5.4	3.8	0.0799	2.7	3.5	0.052	2.8	3.9
		1.88	1.96	0.0283	5.3	3.1	0.00854	7.4	5.1	0.0568	3.8	4.1	0.0377	3.8	4.3
		1.96	2.04	0.0196	6.2	3.6	0.00322	11.6	6.4	0.0454	4.1	4.7	0.0294	4.3	4.7
		2.04	2.12	0.0103	14.5	5.1	0.00137	21.8	16.2	0.0332	7.8	6	0.0191	5.2	5.2
		2.12	2.2										0.0118	18	8.3
0.2	0.28	0.68	0.76	0.147	8.9	9.7	0.241	6.8	6	0.134	10.4	8.5	0.259	6.7	5.6
		0.76	0.84	0.151	7.9	9.1	0.213	5.9	5.5	0.176	7.5	11.2	0.221	5.9	5.3
		0.84	0.92	0.134	5.9	8	0.173	4.7	4.9	0.145	6.1	9.6	0.21	4.5	5.1
		0.92	1	0.122	5.1	7.1	0.147	4.4	4.4	0.134	4.9	8.3	0.182	4	5
		1	1.08	0.118	4.6	6.4	0.139	3.8	4.2	0.143	4.5	7.3	0.175	3.4	4.9
		1.08	1.16	0.113	3.9	5.6	0.115	3.9	4.1	0.127	3.9	6.3	0.158	3.4	4.8
		1.16	1.24	0.0923	4.1	5.1	0.0892	4.1	4.1	0.12	3.7	5.6	0.13	3.5	4.8
		1.24	1.32	0.0839	4.2	5	0.0728	4.4	4.2	0.111	3.8	5.3	0.118	3.4	4.9
		1.32	1.4	0.0746	4.3	5	0.0597	4.6	4.4	0.096	3.9	5.1	0.0972	3.8	5
		1.4	1.48	0.0575	4.3	4.9	0.0482	4.9	4.6	0.0779	4.3	4.8	0.0734	4.2	5.2
		1.48	1.56	0.0474	5.2	5	0.0332	6.8	5.2	0.0658	4.5	4.7	0.0623	4.8	5.4
		1.56	1.64	0.0375	4.2	4.7	0.0232	5.9	5.2	0.0589	3.5	4.2	0.0465	4.1	5.2
		1.64	1.72	0.0292	3.8	4.7	0.0167	4.8	5.7	0.0506	3.1	4.1	0.0361	3.5	5.1
		1.72	1.8	0.0214	4.6	4.9	0.0101	6.8	6.6	0.0363	3.7	4.3	0.0281	4.1	5.1
		1.8	1.88	0.0156	5.2	5.1	0.00506	8	7.6	0.0299	4.1	4.7	0.0213	4.5	5.3
		1.88	1.96	0.0103	6.8	5.4	0.00282	10.6	9.3	0.0225	4.9	5.2	0.014	4.8	5.5
		1.96	2.04	0.00614	10.1	5.9	0.00117	15.3	12	0.0192	5.1	6.1	0.00975	5.9	5.9
		2.04	2.12	0.00349	15.3	6.9	0.00035	26.3	19	0.0138	7	6.9	0.00725	7.4	6.7
		2.12	2.2										0.00385	20.6	10.7
0.28	0.36	0.76	0.84	0.0347	35.1	19.5	0.0508	16.6	11.3	0.0283	32.5	19.3	0.0453	19.7	8.7
		0.84	0.92	0.0226	21.1	13.1	0.0361	14.2	10	0.0263	18.7	15.8	0.0518	11.1	8
		0.92	1	0.026	12.3	10.5	0.0398	8.7	9.1	0.0336	12.3	14	0.0459	8.6	7.1
		1	1.08	0.0254	12.8	9.8	0.0369	7.1	8.3	0.0343	11.6	12.7	0.045	6.7	6.2
		1.08	1.16	0.0247	8.5	8	0.0328	6.8	7.3	0.0359	7	11.2	0.0381	6.1	5.6
		1.16	1.24	0.0237	7.6	7.5	0.0219	7.7	6.8	0.0337	6.8	9.9	0.0386	5.6	5.6
		1.24	1.32	0.0218	7.5	6.8	0.023	6.6	6.7	0.037	6.3	9.5	0.0364	6.2	5.7
		1.32	1.4	0.0226	6.2	6.3	0.017	8.3	6.8	0.0274	6	6.1	0.0304	5.7	5.7
		1.4	1.48	0.0164	7	5.9	0.0124	7.9	6.8	0.0257	5.9	8	0.0239	5.9	6.1
		1.48	1.56	0.0131	7.4	5.8	0.0096	8.8	7.3	0.0247	5.9	7.6	0.0203	6.4	6.4
		1.56	1.64	0.0102	9.7	6	0.00748	10.2	8.1	0.019	6.4	6.9	0.0149	8.1	6.8
		1.64	1.72	0.00762	8.7	5.7	0.00504	11.5	8.9	0.0141	6.3	6.3	0.0128	7.8	7.4
		1.72	1.8	0.00539	8.7	5.8	0.00322	10.4	8.7	0.0109	5.6	6	0.00908	6.3	7.7
		1.8	1.88	0.00414	9.9	7.8	0.00186	12.1	12.1	0.00999	6	6.1	0.00691	6.7	8.9
		1.88	1.96	0.003	9.7	7.7	0.00108	16.4	12.9	0.00758	6.7	6.2	0.00519	9	10.5
		1.96	2.04	0.0014	18.8	9.1				0.00649	8.6	7.1	0.00321	14.5	13.2
		2.04	2.12	0.000876	29.7	11.8				0.0034	11.8	6.4	0.00198	12.2	14.5
		2.12	2.2	0.000483	27.5	17.3				0.00355	10.8	8.1	0.00133	37.6	20.6
0.36	0.44	0.84	0.92				0.0106	33.7	20.2						
		0.92	1				0.00754	23	17.8				0.0091	22.9	14.1
		1	1.08				0.00334	32.8	13.9				0.00933	21.2	13.6
		1.08	1.16				0.0065	23.1	14.7				0.00859	22.8	13.3
		1.16	1.24				0.0049	31.9	16.6				0.00895	18.4	11.7
		1.24	1.32	0.00376	31.4	16.5	0.00447	17.6	13.2	0.00702	21.4	12.5	0.00768	13.8	10.4
		1.32	1.4	0.00314	22.5	14	0.00418	15.5	11.2	0.00735	16.1	10.9	0.00776	12	11
		1.4	1.48	0.00252	21.3	12.4	0.00262	21.7	11.8	0.00473	16.9	9	0.00673	14.7	13.4
		1.48	1.56	0.00351	13.3	11.2	0.00221	20.9	11.9	0.00538	11.5	9.3	0.005	14.2	15.3
		1.56	1.64	0.00283	12.4	10.2	0.00205	31.7	17.6	0.00564	9.4	8	0.0039	24.7	18.9
		1.64	1.72	0.00219	13.6	9.6	0.00162	35.3	17.6	0.0041	11.3	7.7	0.00364	30.1	23.2
		1.72	1.8	0.00161	16.9	11.2				0.00308	11.3	8.2	0.00226	20.9	25.6
		1.8	1.88	0.00103	19.6	14				0.00259	11.3	8.5			
		1.88	1.96	0.000635	21.6	19.3				0.00196	12.7	9.3			
		1.96	2.04							0.00171	12.4	10.9			
		2.04	2.12							0.00147	19.4	15.8			

Hiermit versichere ich, dass ich die vorliegende Diplomarbeit selbstständig verfasst und keine anderen als die angegebenen Hilfsmittel verwendet habe.

Martin Ruprecht
Karlsruhe, den 31. Mai 2012